

**Springer Theses**

Recognizing Outstanding Ph.D. Research

Johanna Ricarda Bruckner

# A First Example of a Lyotropic Smectic C\* Analog Phase

Design, Properties and Chirality  
Effects

 Springer

# **Springer Theses**

Recognizing Outstanding Ph.D. Research

## **Aims and Scope**

The series “Springer Theses” brings together a selection of the very best Ph.D. theses from around the world and across the physical sciences. Nominated and endorsed by two recognized specialists, each published volume has been selected for its scientific excellence and the high impact of its contents for the pertinent field of research. For greater accessibility to non-specialists, the published versions include an extended introduction, as well as a foreword by the student’s supervisor explaining the special relevance of the work for the field. As a whole, the series will provide a valuable resource both for newcomers to the research fields described, and for other scientists seeking detailed background information on special questions. Finally, it provides an accredited documentation of the valuable contributions made by today’s younger generation of scientists.

### **Theses are accepted into the series by invited nomination only and must fulfill all of the following criteria**

- They must be written in good English.
- The topic should fall within the confines of Chemistry, Physics, Earth Sciences, Engineering and related interdisciplinary fields such as Materials, Nanoscience, Chemical Engineering, Complex Systems and Biophysics.
- The work reported in the thesis must represent a significant scientific advance.
- If the thesis includes previously published material, permission to reproduce this must be gained from the respective copyright holder.
- They must have been examined and passed during the 12 months prior to nomination.
- Each thesis should include a foreword by the supervisor outlining the significance of its content.
- The theses should have a clearly defined structure including an introduction accessible to scientists not expert in that particular field.

More information about this series at <http://www.springer.com/series/8790>

Johanna Ricarda Bruckner

# A First Example of a Lyotropic Smectic C\* Analog Phase

Design, Properties and Chirality Effects

Doctoral Thesis accepted by  
the University of Stuttgart, Stuttgart, Germany

 Springer

*Author*

Dr. Johanna Ricarda Bruckner  
Institute of Physical Chemistry  
University of Stuttgart  
Stuttgart  
Germany

*Supervisor*

Prof. Frank Gießelmann  
Institute of Physical Chemistry  
University of Stuttgart  
Stuttgart  
Germany

ISSN 2190-5053

Springer Theses

ISBN 978-3-319-27202-3

DOI 10.1007/978-3-319-27203-0

ISSN 2190-5061 (electronic)

ISBN 978-3-319-27203-0 (eBook)

Library of Congress Control Number: 2015956136

© Springer International Publishing Switzerland 2016

This work is subject to copyright. All rights are reserved by the Publisher, whether the whole or part of the material is concerned, specifically the rights of translation, reprinting, reuse of illustrations, recitation, broadcasting, reproduction on microfilms or in any other physical way, and transmission or information storage and retrieval, electronic adaptation, computer software, or by similar or dissimilar methodology now known or hereafter developed.

The use of general descriptive names, registered names, trademarks, service marks, etc. in this publication does not imply, even in the absence of a specific statement, that such names are exempt from the relevant protective laws and regulations and therefore free for general use.

The publisher, the authors and the editors are safe to assume that the advice and information in this book are believed to be true and accurate at the date of publication. Neither the publisher nor the authors or the editors give a warranty, express or implied, with respect to the material contained herein or for any errors or omissions that may have been made.

Printed on acid-free paper

This Springer imprint is published by SpringerNature

The registered company is Springer International Publishing AG Switzerland

**Parts of this thesis have been published in the following journal articles:**

J.R. Bruckner, D. Krueerke, J.H. Porada, S. Jagiella, D. Blunk and F. Giesselmann, The 2D-correlated structures of a lyotropic liquid crystalline diol with a phenylpyrimidine core. *J Mater Chem* **22**, 18198–18203 (2012)

J.R. Bruckner, J.H. Porada, C.F. Dietrich, I. Dierking and F. Giesselmann, A lyotropic chiral smectic C liquid crystal with polar electrooptic switching. *Angewandte Chemie International Edition* **52**, 8934–8937 (2013)

J.R. Bruckner, F. Knecht, F. Giesselmann, Origin of the director tilt in the lyotropic smectic C\* analog phase: hydration interactions and solvent variations. *ChemPhysChem*, doi:[10.1002/cphc.201500673](https://doi.org/10.1002/cphc.201500673)

# Supervisor's Foreword

Liquid crystals constitute a distinct thermodynamic state of condensed matter, which combines the fluidity of ordinary liquids with the macroscopic anisotropy of solid crystals. They are quintessential soft matter materials, which are today best known to the broad public for their ubiquitous application as electro-optical material in flat panel liquid crystal displays (LCDs). Systems exhibiting liquid crystalline order range from small rod- or disc-shaped organic molecules (e.g., the 'classic' liquid crystals used in LCD devices), over polymers, biological membranes, dispersions of micelles and nanoparticles to certain quantum electronic materials.

The *plethora* of liquid crystal structures and phases is categorized into two main classes: thermotropic and lyotropic liquid crystals. While thermotropic liquid crystals are formed by, e.g., rod- or disc-shaped molecules in a certain temperature range, lyotropic liquid crystals are 'liquid crystalline solutions,' built up by, e.g., aggregates of amphiphilic molecules in a certain concentration range. Many liquid crystal phases are found in thermotropic as well as in lyotropic systems. In some cases, however, the lyotropic analog of a thermotropic phase has never been observed. The probably most interesting of these 'missing link' cases is the thermotropic chiral smectic C\* (SmC\*) phase, which has become famous as the only spontaneously polarized, ferroelectric fluid in nature.

In this thesis Johanna Bruckner reports the discovery of the lyotropic counterpart of the thermotropic SmC\* phase. By means of polarizing optical microscopy, X-ray diffraction and electro-optic experiments she firmly establishes aspects of its structure and elucidates its fascinating properties, among them a pronounced polar electro-optic effect, analogous to the ferroelectric switching of its thermotropic counterpart. The helical ground state of this new lyotropic phase raises the fundamental question of how chiral interactions are 'communicated' across layers of disordered and achiral solvent molecules which are located between adjacent

bilayers of the chiral amphiphile molecules. This thesis bridges an important gap between thermotropic and lyotropic liquid crystals and pioneers a new field of liquid crystal research.

Stuttgart  
October 2015

Frank Gießelmann



# Acknowledgments

Many people supported me during my doctorate and thus contributed to the successful realization of this thesis. I want to express my gratitude to every single one of them. My special thanks go to:

- Prof. Dr. Frank Gießelmann for the opportunity to investigate a fascinating issue in liquid crystal research, his excellent advice and last but not least his steady and invaluable support
- Prof. Dr. Peer Fischer for preparing the second assessment for this thesis
- Prof. Dr. Sabine Laschat for taking over the post of chairperson in the examination
- The state of Baden-Württemberg for financial support in the form of a scholarship
- Dr. Jan Porada for providing the surfactants which form the basis of this thesis
- Everyone who took part in the scientific discussion concerning the results of this thesis
- Dr. Nadia Kapernaum, Dr. Jan Porada, Judith Bruckner, Florian Schörg, and Prof. Dr. Joseph MacLennan for proofreading
- All members of the workshops for mechanics and electronics as well as the technical assistants for their fast and uncomplicated support
- My bachelor student Clarissa Dietrich as well as my research interns Marc Harjung, Friederike Knecht, and Iris Wurzbach for their participation in the research projects
- All present and former members of the work group for the excellent atmosphere and their willingness to help in every respect: Dr. Alberto Sánchez Castillo, Andreas Bogner, Boris Tschertsche, Carsten Müller, Clarissa Dietrich, Dr. Daniel Krüerke, Dr. Dorothee Nonnenmacher, Florian Schörg, Frank Jenz, Friederike Knecht, Gabriele Bräuning, Inge Blankenship, Iris Wurzbach, Marc Harjung, Michael Christian Schlick, Dr. Nadia Kapernaum, Dr. Peter Staffeld, Dr. Stefan Jagiella

- My friends, my family, and everyone else who accompanied and supported me throughout my studies and doctorate
- My parents without whom none of this would have been possible.

# Contents

<b>1</b>	<b>Introduction</b>	1
1.1	The Liquid Crystalline State of Matter	1
1.2	The SmC* Phase: A Ferroelectric Fluid	3
1.3	The Lyotropic SmC Analog Phase	6
	References	9
<b>2</b>	<b>Aims and Scope of This Thesis</b>	11
<b>3</b>	<b>Thermotropic and Lyotropic Liquid Crystals</b>	13
3.1	The Building Blocks	13
3.2	Survey of Important Mesophases	16
3.2.1	The Nematic Phases	17
3.2.2	The Smectic Phases	20
3.2.3	The Columnar Phases	24
3.2.4	Phase Sequences of Thermotropic and Lyotropic Liquid Crystals	26
	References	27
<b>4</b>	<b>Materials and Experimental Techniques</b>	29
4.1	Materials and Preparation of Samples	29
4.2	Differential Scanning Calorimetry	31
4.3	Polarizing Optical Microscopy	31
4.4	Measurement of the Director Tilt Angle	34
4.5	Measurement of the Helical Pitch	35
4.5.1	The ‘Direct’ Method	35
4.5.2	The Cano Method	37
4.6	Electric and Electro-Optical Measurements	39
4.6.1	Measurement of the Spontaneous Electric Polarization	39
4.6.2	Measurement of the Switching Time	40

4.7	X-Ray Diffraction . . . . .	41
4.7.1	Basic Concepts of X-Ray Diffraction . . . . .	41
4.7.2	X-Ray Diffraction Experiments . . . . .	46
	References . . . . .	47
<b>5</b>	<b>Results and Discussion . . . . .</b>	<b>49</b>
5.1	Preliminary Investigations . . . . .	49
5.1.1	Design Strategy . . . . .	49
5.1.2	Screening of the Diverse Surfactant/Solvent Systems . . . . .	51
5.2	Phase Diagrams of Selected Solvent/Surfactant Mixtures . . . . .	66
5.2.1	Phase Diagrams of C5O/Solvent Systems Exhibiting the Lyotropic SmC* Analog Phase . . . . .	66
5.2.2	The C5O/ <i>N</i> -Methylformamide System: A Counterexample but not less Interesting . . . . .	73
5.3	Structural and Physical Properties of the Lyotropic SmC* Analog Phase . . . . .	78
5.3.1	X-Ray Diffraction Measurements . . . . .	79
5.3.2	Measurement of the Director Tilt . . . . .	83
5.3.3	Calorimetric Investigations . . . . .	85
5.4	Chirality Effects in the Lyotropic SmC* Analog Phase . . . . .	88
5.4.1	Investigation of the Helical Pitch . . . . .	88
5.4.2	Electro-optical Investigations . . . . .	92
5.5	Model of the Lyotropic SmC* Analog Phase . . . . .	99
	References . . . . .	103
<b>6</b>	<b>Summary . . . . .</b>	<b>105</b>
	<b>Appendix . . . . .</b>	<b>109</b>

# Symbols and Acronyms

## Latin Symbols

$a_{cs}$	Cross-sectional area of the polar head group of an amphiphile
$a, b$	Lattice parameters
$A_1, A_2$	Areas underneath a measurement curve
$A_{El}$	Electrode area
$\mathbf{c}$	$\mathbf{c}$ -director, projection of the $\mathbf{n}$ -director into the $\mathbf{x,y}$ -plane
$C$	Capacity
$C_2$	Schoenflies notation of a point group with a twofold axis of rotation
$C_{2h}$	Schoenflies notation of a point group with a twofold axis of rotation and a mirror plane perpendicular to the axis of rotation
$d$	Smectic or lamellar layer spacing, periodicity distance
$d_{bl}$	Thickness of the bilayer
$d_{calc.}$	Calculated periodicity distance
$d_{hk}$	Periodicity distance associated with certain Miller indices
$d_{obs.}$	Observed periodicity distance
$d_s$	Thickness of the solvent layer
$d(\text{SmA})$	Layer spacing in the SmA phase
$d(\text{SmC})$	Layer spacing in the SmC phase
$\mathbf{E}$	Electric field
$E_{T30}$	Polarity determined by solvatochromy
$f$	Molecular form factor
$F(hk)$	Scattering amplitude
$g(\mathbf{q})$	Pair correlation function
$h, k, l$	Miller indices
$\mathbf{H}$	Magnetic field
$\Delta_{tr}H$	Transition enthalpy
$i$	Consecutive number
$I$	Intensity

$I(hk)$	Intensity of a diffraction peak
$i_{\text{el.}}$	Current
$I_{\text{el.}}$	Total current
$I_{\text{rel.}}$	Relative intensity
$\mathbf{k}$	Layer normal
$\mathbf{k}_i$	Wave vector of the incident beam
$\mathbf{k}_s$	Wave vector of the scattered beam
$l$	Length of the hydrophobic chain of an amphiphile
$L$	Molecular length
$L_{\text{calc.}}$	Calculated molecular length
$m$	Slope
$M$	Molecular weight
$N$	Integer
$\mathbf{n}$	Director
$n$	Refractive index
$n_{\parallel}, n_{\perp}$	Refractive indices parallel and perpendicular to the optical main axis
$N_A$	Avogadro constant
$\mathbf{n}_{\text{local}}$	Local director
$n_p$	Number density
$p$	Helical pitch length
$p^{-1}$	Helical twist
$p1, p2, p2gg,$ $p2mg, c2mm,$ $p6mm$	Plane crystallographic groups of columnar phases
$\mathbf{P}_S$	Spontaneous electric polarization
$\mathbf{q}$	Scattering vector
$\mathbf{r}$	Distance
$R$	Residual organic group
$R_c$	Radius of curvature
$R_{\text{el.}}$	Resistance
$R_{\text{ITO}}$	Resistance of the ITO layer
$R_L$	Load resistance
$s$	Point singularity/'strength' of the disclination
$S_2$	Orientalational order parameter
$S(\mathbf{q})$	Structure factor
$t$	Time
$T$	Temperature
$T_{\text{bp}}$	Transition temperature at the boiling point
$T_C$	Temperature at the lamellar $L_{\alpha}$ to lyotropic $\text{SmC}^*$ analog phase transition
$T_{\text{cp}}$	Transition temperature at the clearing point
$T_{\text{mp}}$	Transition temperature at the melting point
$U$	Voltage
$\Delta U$	Compensated voltage

$V$	Effective volume of an amphiphile
$V_s$	Scattering volume
$w(\text{solvent})$	Mass fraction of the solvent
$X$	Linking organic group
$x(\text{solvent})$	Mole fraction of the solvent
$\mathbf{x}, \mathbf{y}, \mathbf{z}$	Basis of the Cartesian coordinate system
$x_N$	Distance from the center of a lense to the $N^{\text{th}}$ disclination line
$z_i$	Position of a mesogen $i$ with respect to $\mathbf{z}$

## Greek Symbols

$\alpha_i$	Angle between the director $\mathbf{n}$ and the main axis of a molecule $i$
$\alpha, \beta, \gamma$	Lattice angles
$\chi$	Azimuth angle
$\phi(hk)$	Phase angle of the scattering amplitude
$\gamma$	Viscosity
$\gamma_\varphi$	Rotational viscosity
$\lambda$	Wavelength
$\mu$	Dipole moment
$\Pi$	Packing parameter
$\theta$	Tilt angel
$\theta_{\text{diff.}}$	Diffraction angle
$\theta_{\text{opt}}$	Tilt angle measured by optical method
$\theta_{\text{steric}}$	Tilt angle calculated from the layer shrinkage determined by X-ray diffraction
$\rho$	Density
$\rho(x, y)$	Electron density
$\Sigma$	Smectic order parameter
$\sigma$	Mirror plane
$\tau$	Switching time
$\tau_{10-90}$	Switching time, measured in the range between 10 % and 90 % of the maximum signal
$\zeta$	Correlation length

## Acronyms

BH8	Benzene-hexa- <i>n</i> -octanoate
C3	( <i>R</i> )-3-(4-(5-heptylpyrimidin-2-yl)phenoxy)propane-1,2-diol
C5	( <i>S</i> )-5-(4-(5-heptylpyrimidin-2-yl)phenoxy)pentane-1,2-diol
C5O	( <i>R</i> )-3-(2-(4-(5-heptylpyrimidin-2-yl)phenoxy)ethoxy)propane-1,2-diol
C6	( <i>S</i> )-6-(4-(5-heptylpyrimidin-2-yl)phenoxy)hexane-1,2-diol

C6O	( <i>R</i> )-3-(3-(4-(5-heptylpyrimidin-2-yl)phenoxy)propoxy)propane-1,2-diol
Col, Col <sub>1</sub> , Col <sub>2</sub>	Columnar phases
Col <sub>h</sub>	Thermotropic hexagonal phase
Col <sub>ob</sub>	Thermotropic oblique phase
Col <sub>r</sub>	Thermotropic rectangular phase
Cr, Cr <sub>1</sub> , Cr <sub>2</sub>	Crystalline phases
D	Dystetic phase
DFG	Deutsche Forschungsgemeinschaft
DMF	Dimethylformamide
DSC	Differential scanning calorimetry
EG	Ethylene glycol
FT	Fourier transform
H <sub>α</sub>	Lyotropic hexagonal phase
HCONH <sub>2</sub>	Formamide
Iso	Isotropic
ITO	Indium tin oxide
LC	Liquid crystal
L <sub>α</sub>	Lamellar phase with molten alkyl chains (fluid)
L <sub>α'</sub> *	Tilted lamellar phase with molten alkyl chains (fluid)
L <sub>β'</sub> *	Tilted lamellar phase with frozen alkyl chains (gel-like)
M <sub>α</sub>	Lyotropic monoclinic phase
N	Nematic phase
N*	Chiral nematic phase/cholesteric phase
N <sub>C</sub>	Nematic phase composed of rod-like micelles
N <sub>C</sub> *	Cholesteric phase composed of rod-like micelles
N <sub>D</sub>	Nematic phase composed of disc-like micelles
N <sub>D</sub> *	Cholesteric phase composed of disc-like micelles
NMF	<i>N</i> -methylformamide
N <sub>RE</sub>	Re-entrant nematic phase
N <sub>RE</sub> *	Re-entrant cholesteric phase
PEG	Polyethylene glycol
POM	Polarizing optical microscopy
R	Lyotropic rectangular phase
rac-C5O	( <i>rac</i> )-3-(2-(4-(5-heptylpyrimidin-2-yl)phenoxy)ethoxy)propane-1,2-diol
SAXS	Small-angle X-ray scattering
SDS	Sodium dodecyl sulfate
SmA	Smectic A phase
SmA*	Chiral smectic A phase
Sm $\tilde{A}$	Modulated smectic $\tilde{A}$ antiphase
SmB	Smectic B phase
SmC	Smectic C phase
SmC*	Chiral smectic C phase



Sm $\tilde{C}$	Modulated smectic $\tilde{C}$ antiphase
SmF	Smectic F phase
SmF*	Chiral smectic F phase
SmI	Smectic I phase
SmI*	Chiral smectic I phase
TBBA	Terephthal-bis-( <i>p</i> -butylaniline)
TGB	Twist grain boundary phase
TGBA*	Twist grain boundary A* phase
TGBC*	Twist grain boundary C* phase
TGBL $^*_\alpha$	Lyotropic twist grain boundary L $^*_\alpha$ phase
UV	Ultraviolet
WAXS	Wide-angle X-ray scattering
wt%	Weight percent

# Chapter 1

## Introduction

In this thesis a lyotropic analog of the thermotropic chiral smectic C ( $\text{SmC}^*$ ) phase is presented for the first time. So far, only very scarce examples of the achiral variant of this phase have been known in lyotropic liquid crystals and no comprehensive studies have been performed on them. Thus, the focus of the present thesis is on the proof of existence and characterization of this novel phase. Furthermore, a tentative model of the lyotropic  $\text{SmC}^*$  analog phase is introduced. Thereby, this thesis contributes to the unification of the often separately treated fields of lyotropic and thermotropic liquid crystals.

To start with, the present chapter will address some fundamental concepts of liquid crystals to enable a thorough comprehension of the aims and scope of this thesis. The properties of and the discovery of the thermotropic  $\text{SmC}^*$  phase will be dealt with in more detail, as they are essential for understanding the significance of the thesis presented. Finally, examples of lyotropic analogs of the achiral smectic C ( $\text{SmC}$ ) phase, which were known up to now, will be discussed in this introductory chapter.

### 1.1 The Liquid Crystalline State of Matter

The liquid crystalline state ranges between the solid and the fluid states of matter. Moreover, it combines characteristic features known from crystals and liquids. Hence, it is also called mesomorphic state to emphasize its intermediate position. In Fig. 1.1 the four states crystalline, liquid crystalline, liquid and gaseous are displayed schematically. While there is positional as well as orientational long-range order of the molecules in the crystalline state, there is no such thing in the liquid state. In liquids only short-range order exists. Both concepts apply for liquid crystals. Depending on the degree of order in the liquid crystalline structure, different phases are distinguished. They are termed mesophases and their building blocks are called mesogens. In the simplest case of a nematic (N) mesophase, as shown in Fig. 1.1, only long-range orientational order of the mesogenic main axes is present. The lack of any long-range positional order causes a fluid-like short range order of the mesogenic centers in three dimensions. The mesophase thus

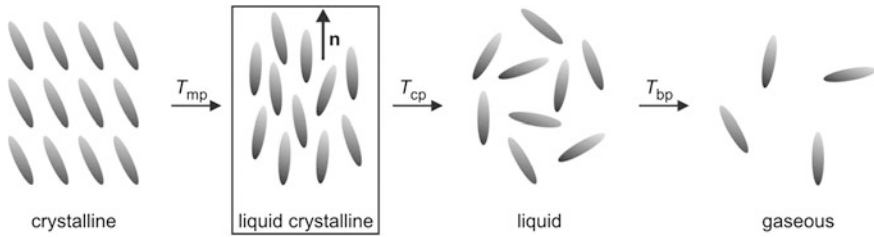


**Fig. 1.1** Sketch of the molecular arrangement in the three commonly known states of matter, crystalline, liquid and gaseous, as well as the intermediary liquid crystalline state. The molecules or mesogens are depicted as rods. Transitions from a higher ordered state to the next lower ordered state take place by increasing the temperature above the melting point ( $T_{mp}$ ), the clearing point ( $T_{cp}$ ) or the boiling point ( $T_{bp}$ ), respectively. In the case of the liquid crystalline state the director  $\mathbf{n}$ , which is fundamental for the description of liquid crystalline phases, is indicated

combines the fluidity of a liquid with anisotropic properties known from crystals, e.g. an anisotropic dielectric permittivity. In more complex liquid crystalline phases a one- or two-dimensional long-range positional order of the mesogenic centers may occur. But at least in one direction, a fluid-like order has to persist.

One of the most important physical quantities for describing liquid crystalline phases is the director  $\mathbf{n}$ . It indicates the average direction of the mesogenic principle axis with the highest symmetry, as shown in Fig. 1.1. The directions  $+\mathbf{n}$  and  $-\mathbf{n}$  are physically indistinguishable, independent of the nature of the mesogen. The quality of the orientational order of the mesogenic main axes along the director  $\mathbf{n}$  is described by the orientational order parameter  $S_2$ . It considers the angle  $\alpha_i$  between the director  $\mathbf{n}$  and the principle axis with the highest symmetry of every mesogen  $i$ . The orientational order parameter  $S_2$  can be written as:

$$S_2 = \frac{1}{2} \langle 3 \cos^2 \alpha_i - 1 \rangle. \quad (1.1)$$

In isotropic liquids the orientational order parameter  $S_2$  is 0, as the mesogens are oriented randomly. In liquid crystals the orientational order parameter  $S_2$  rises to values of at least 0.4 [1] and may reach values close to 1.0 [2].

In general, two types of liquid crystals can be distinguished. On the one hand, there are the so-called thermotropic liquid crystals. The mesogens in this type of liquid crystals are organic molecules with an anisotropic shape. The appearance of specific thermotropic phases depends solely on the temperature at a constant pressure. On the other hand, there are the lyotropic liquid crystals. The mesophases of lyotropic liquid crystals are composed of surfactant molecules, which are organic molecules with competing polarities in different parts of the molecule and a solvent, which is typically water. By solving the surfactant molecules in the solvent, the molecules assemble themselves into aggregates, which hide their hydrophobic parts from the polar solvent. These aggregates are called micelles. Thus, in lyotropic liquid crystals the mesogens are no single molecules, but micelles with anisometric

shape. The most important parameter for the formation of a specific mesophase, therefore, is the solvent concentration. The temperature plays a secondary role.

From a historical point of view as well as due to their applications, thermotropic and lyotropic liquid crystals have always been treated separately. While thermotropics and the concept of liquid crystallinity in general were discovered as late as in 1888 [3], lyotropic phases were “known” to mankind since the Bronze Age [4], as they occur during the soap-making process. Due to this, lyotropic liquid crystals find their main applications in the detergent industry and in cosmetics. As various biological systems, e.g. cell membranes, take a lyotropic liquid crystalline form, they also possess some medical and pharmaceutical importance [5]. In contrast, thermotropic liquid crystals are used for completely different applications, e.g. for displays, thermography, tunable filters or lasers [6]. Thus, it is not astonishing, that two distinct fields of research evolved for the two types of liquid crystals. However, thermotropic and lyotropic liquid crystals share a common state of matter with many similarities. For example, many mesophases which occur in thermotropics can also be found in lyotropics. Still, there are some thermotropic phases which do not seem to have a lyotropic counterpart.

One of the most outstanding examples of this is the thermotropic SmC phase and especially its chiral variant SmC\*. Due to its unique properties, the SmC\* phase attracted considerable scientific interest over the last four decades. Therefore, the investigation of a lyotropic analog of the SmC\* phase would be especially interesting in regard to the formation and properties of this so far unknown lyotropic mesophase. To explain the significance of the thermotropic SmC\* phase, a brief synopsis of its discovery and properties will be given in the following chapter.

## 1.2 The SmC\* Phase: A Ferroelectric Fluid

The SmC phase as such was first discovered in 1933 by means of X-ray diffraction [7]. In the SmC phase the molecules are arranged in two dimensional layers, which are stacked upon each other in the third dimension of space. An illustration of this is shown in Fig. 1.2a. Within those smectic layers a fluid-like order can be found, while a long range positional order exists in the stacking direction along the layer normal  $\mathbf{k}$ . As the molecules in the layers are tilted with respect to the layer normal  $\mathbf{k}$ , the director  $\mathbf{n}$  and the layer normal  $\mathbf{k}$  include the so-called tilt angle  $\theta$ .

In the case of the SmC\* phase, which is a SmC phase composed of chiral molecules, the structure is significantly modified by the molecular chirality. As shown in Fig. 1.2b, the tilt direction, which is indicated by the director  $\mathbf{c}$ , precesses from layer to layer, thus leading to the formation of a helical superstructure. The helical pitch  $p$  usually takes values between 0.5 and 50  $\mu\text{m}$ , which relates to approximately  $10^3$  smectic layers [8, 9]. The helical structure manifests itself macroscopically in the ability to selectively reflect circular polarized light with a

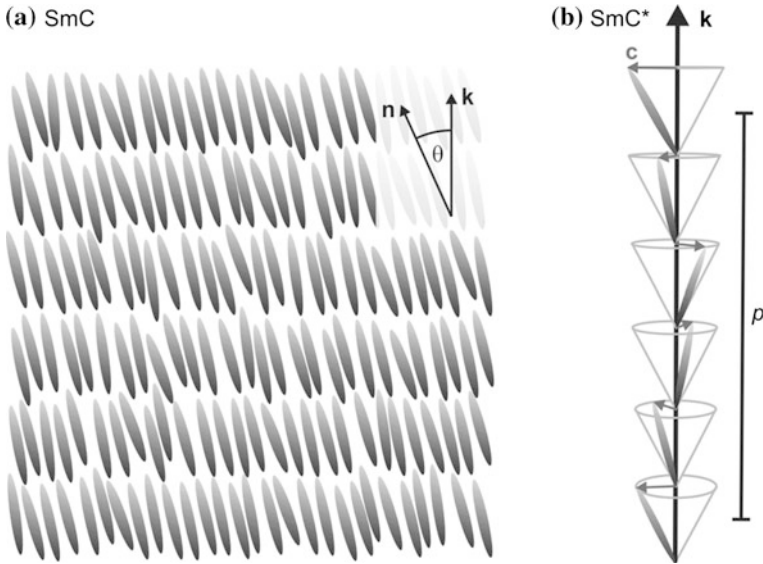


**Fig. 1.2** **a** Cut through the structure of the SmC phase with indicated directions of the director  $\mathbf{n}$  and the layer normal  $\mathbf{k}$ . The smectic layers are extended two-dimensionally parallel and perpendicular to the drawing plane. **b** Illustration of the helical structure of the SmC\* phase. For the sake of clarity, only one mesogen per layer is shown. From one layer to the next, the direction of the c-director, and thus the orientation of the molecules, changes gradually. The distance which is necessary for the c-director to rotate by  $2\pi$  is called the helical pitch  $p$

wave length corresponding to the helical pitch and between crossed polarizers in a striped texture<sup>1</sup> due to a changing effective birefringence.

Even though the first SmC\* materials were synthesized at the beginning of the 20th century [10], it took decades until the macroscopic chirality of the SmC\* phase was discovered. The existence of a hypothetical twisted smectic phase was first discussed by Saupe in 1969 [11]. Two years later, in 1971, Helfrich and Oh [12] detected the SmC\* phase as such for the first time due to its ability to selectively reflect light. The ferroelectricity of the SmC\* phase was then theoretically predicted, explained and experimentally proved by Meyer et al. [13] in 1975 for the first time. Five years later, Clark and Lagerwall published their groundbreaking work [14], which demonstrated the ferroelectric switching of the SmC\* phase if surface-stabilized.

To understand why the SmC\* phase is ferroelectric, the symmetries of the SmC as well as of the SmC\* phase have to be considered. The symmetry of the SmC phase is described by the point group  $C_{2h}$ , as it possesses a mirror plane within the tilt plane and a two-folded rotation axis perpendicular to it, if considering that  $+\mathbf{n} = -\mathbf{n}$ . An illustration of this is shown in Fig. 1.3a. If the phase is instead

<sup>1</sup>The term ‘texture’ is described in detail in Sect. 4.3.

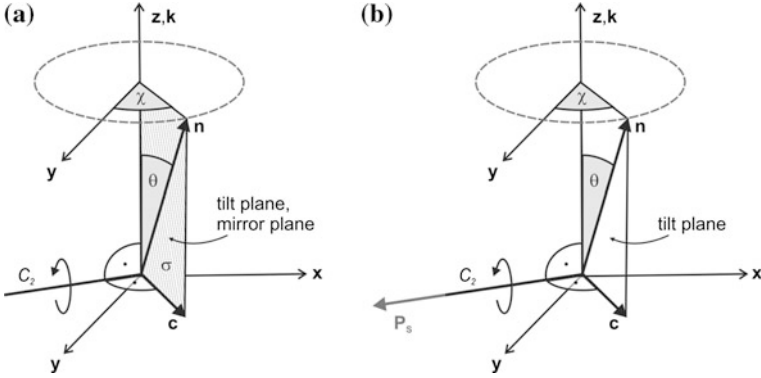


**Fig. 1.3** Symmetry elements in **a** the SmC phase, which belongs to the point group  $C_{2h}$  and **b** the SmC\* phase in which the symmetry is reduced to the point group  $C_2$ . The smectic layers are supposed to be within the  $x,y$ -plane. The angle between the layer normal  $\mathbf{k}$  and the director  $\mathbf{n}$  is the tilt angle  $\theta$ . The projection of  $\mathbf{n}$  on the  $x,y$ -plane, results in the director  $\mathbf{c}$ . The  $y$ -axis and the director  $\mathbf{c}$  include the azimuth angle  $\chi$  (redrawn after [9])

composed of chiral molecules, as it is the case in the SmC\* phase, the mirror plane is removed, resulting in the point group  $C_2$ . This situation is depicted in Fig. 1.3b.

The point group  $C_2$  is a polar point group with the  $C_2$ -axis being a polar axis allowing a nonzero spontaneous electric polarization  $\mathbf{P}_S$ . In a molecular picture, this means that the transverse dipole moments are not canceled due to the lack of the mirror plane. In consequence, a spontaneous electric polarization  $\mathbf{P}_S$  occurs along the polar  $C_2$ -axis and thus perpendicular to the plane spanned by  $\mathbf{n}$  and  $\mathbf{k}$ :

$$\mathbf{P}_S \propto \mathbf{k} \times \mathbf{n}. \quad (1.2)$$

Furthermore, the magnitude of this spontaneous electric polarization  $\mathbf{P}_S$  is related to the tilt angle  $\theta$  according to:

$$|\mathbf{P}_S| \propto \sin \theta. \quad (1.3)$$

However, due to the helical super structure of the SmC\* phase, the spontaneous polarization  $\mathbf{P}_S$  of the individual smectic layers is averaged out. Therefore, the formation of the helix has to be suppressed in order to achieve a macroscopic ferroelectricity of the SmC\* phase. This can be done effectively by surface stabilization in very thin samples, as demonstrated by Clark and Lagerwall in 1980 [14]. They showed that under these conditions only two states may occur and that it is possible to switch between the two states within the range of microseconds by reversing the direction of the applied electric field. A sketch of this is given in Fig. 1.4.

The SmC\* phase attracted considerable interest in the liquid crystal research community, especially after its ferroelectricity was shown. Ferroelectricity was discovered as late as 1921 [16] and was solely known for solid materials up to the

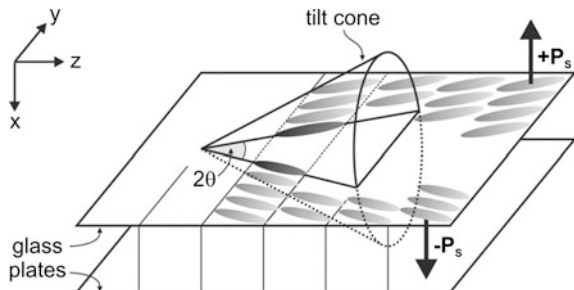


**Fig. 1.4** Sketch of the surface-stabilized ferroelectric liquid crystal (SSFLC) cell structure. Due to the surface-stabilization, the helical structure of the  $\text{SmC}^*$  phase is unwound as only two director orientations on the tilt cone can be realized. These two director states correspond to either UP or DOWN polarization (redrawn after [15])

pioneering work of Meyer et al. [13]. The fluid state of the  $\text{SmC}^*$  phase opened up a completely new and fascinating field of research. Furthermore, the fluidity of the new ferroelectric material allowed the development of unique applications, i.e. fast switching electro-optic devices [17]. Up to the present date, the  $\text{SmC}^*$  phase is the only known ferroelectric material which is fluid,<sup>2</sup> and thus it is still one of the thermotropic liquid crystalline phases attracting the most attention. However, in lyotropic liquid crystals an analog phase was not found so far.

### 1.3 The Lyotropic $\text{SmC}$ Analog Phase

Lyotropic liquid crystals tend to form layered structures, which are called lamellar phases. Yet, the mesogens are usually parallel to the layer normal  $\mathbf{k}$  (*cf.* lamellar  $L_\alpha$  phase, Sect. 3.2.2) and not tilted with respect to it, as is the case in the thermotropic  $\text{SmC}$  phase. A very plausible explanation is commonly accepted for this behavior. In lyotropic liquid crystals the lamellas are composed of alternating bilayers of surfactant and solvent molecules as shown in Fig. 1.5a. The individual layers of surfactant molecules are therefore separated from each other by layers of solvent molecules, which only possess short range order as in common liquids. Thus, the disordered layers of solvent molecules prevent any correlation of the director tilt between adjacent surfactant layers. In consequence, a long-range correlation of the director tilt, as depicted in Fig. 1.5b, or moreover of chirality, which would be necessary for the formation of a lyotropic analog of the  $\text{SmC}^*$  phase, does not seem to be possible in lyotropic liquid crystals. Still, there are very rare examples in

<sup>2</sup>Actually, there are two higher ordered smectic phases, namely  $\text{SmF}^*$  and  $\text{SmI}^*$ , which are also ferroelectric. These phases, however, are significantly more viscous and thus do not attract the same amount of scientific attention.

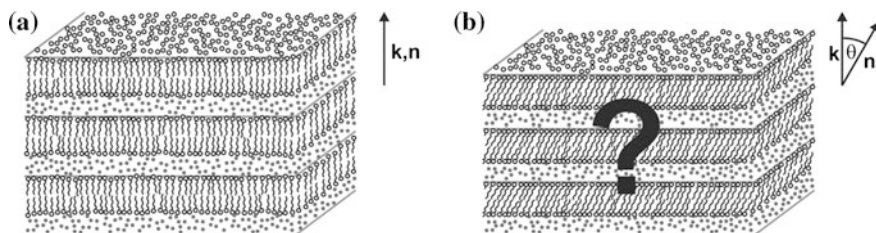


**Fig. 1.5** **a** The well-known lamellar  $L_{\alpha}$  phase is composed of bilayers of surfactant molecules, which are separated from each other by layers of solvent molecules. The surfactant molecules are on the average oriented parallel to the layer normal. **b** The structure of the rarely found lyotropic SmC analog phase is assumed to be similar to the structure of the lamellar  $L_{\alpha}$  phase, though the surfactant molecules should be tilted with respect to the layer normal. However, in literature there are no suggestions for the structure of this phase

literature of lyotropic analogs of the thermotropic SmC phase, which will be presented in this chapter.

Most often, lyotropic SmC analog phases mentioned in literature appear at very low solvent concentrations in direct connection to a thermotropic SmC phase [18–21]. Such phases should be considered as solvent swollen thermotropics rather than as lyotropics, because they get destabilized by the addition of the solvent and thus are no real lyotropic mesophase. Furthermore, the amount of solvent molecules is so low, that the solvent layers do not possess a substantial thickness. Hence, only mesophases which appear solely upon the addition of a solvent are considered to be real lyotropic analogs of the SmC phase in the following.

The phase diagram of an often cited example of a lyotropic SmC analog phase reported by Pietschmann et al. [22] is shown in Fig. 1.6. Here an unconventional diolic surfactant with an aromatic phenylpyrimidine core was claimed to form a very broad lyotropic SmC analog phase in mixtures with water. Unfortunately, the authors did not provide any evidence for the correct phase assignment of the lyotropic SmC analog phase, and later investigations of the system showed, that the phase was indeed a rather complex two dimensional correlated columnar phase [23, 24]. Actually, there are only two examples of lyotropic SmC analog phases in literature, in which the authors included clear proof of the existence of those phases.

The first example is a homologous series of rod-like amphiphiles synthesized by Schafheutle et al. [25]. The molecules possess several ethylene glycol units and form lyotropic SmC analog phases in mixtures with water. An exemplary phase diagram of one of the homologous series of surfactant molecules and water is displayed in Fig. 1.7. The considered mesophase forms between 20 and 45 wt% of water and can therefore be regarded as a true lyotropic phase, the existence of which was proven by X-ray diffraction. A picture of a two-dimensional diffraction pattern of an aligned sample is shown in the inset in Fig. 1.7. As the directions of the small-angle and the wide-angle maxima deviate slightly from a perpendicular orientation, the presence of a tilted structure with a quite small tilt angle is verified (*cf.* Sect. 4.7).



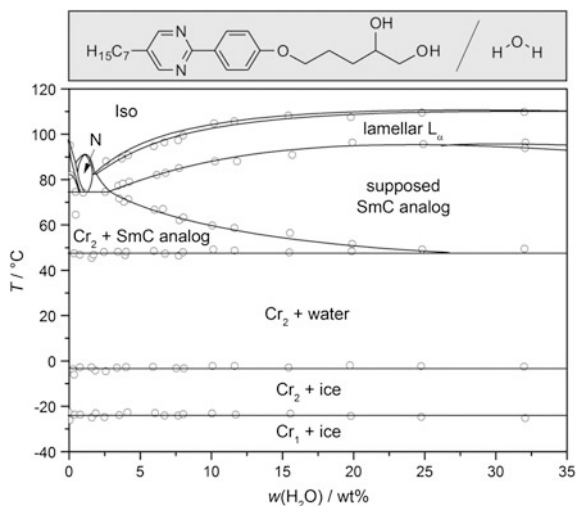


**Fig. 1.6** Phase diagram of 5-[4-(5-*n*-heptylpyrimidine-2-yl)phenoxy]pentane-1,2-diol and water (phase diagram redrawn after [22]). It was shown in later work, that the lyotropic SmC analog phase is indeed a columnar phase [23, 24]. The isotropic phase is denoted with the abbreviation ‘Iso’ and the two crystalline phases with ‘Cr<sub>1</sub>’ or ‘Cr<sub>2</sub>’, respectively. For an explanation of the occurring mesophases and their abbreviations see Chap. 3

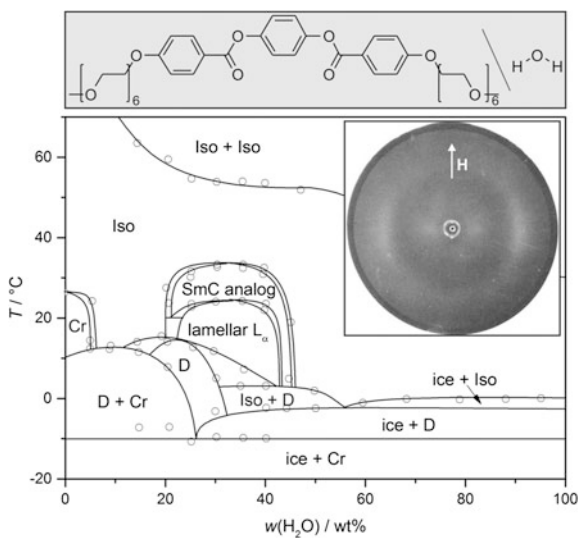


**Fig. 1.7** Phase diagram of 1,4-phenylene bis(4-((2,5,8,11,14,17-hexaoxonadecan-19-yl)oxy)benzoate) and water (redrawn after [25]). The abbreviation ‘D’ stands for dystetic, ‘Iso’ for isotropic and ‘Cr’ for crystalline. The *inset* shows a two-dimensional X-ray diffraction image of an aligned sample of the lyotropic SmC analog phase. The direction of an applied magnetic field **H** is indicated (adapted from [25], Copyright 1988 Taylor & Francis, [www.tandfonline.com](http://www.tandfonline.com))

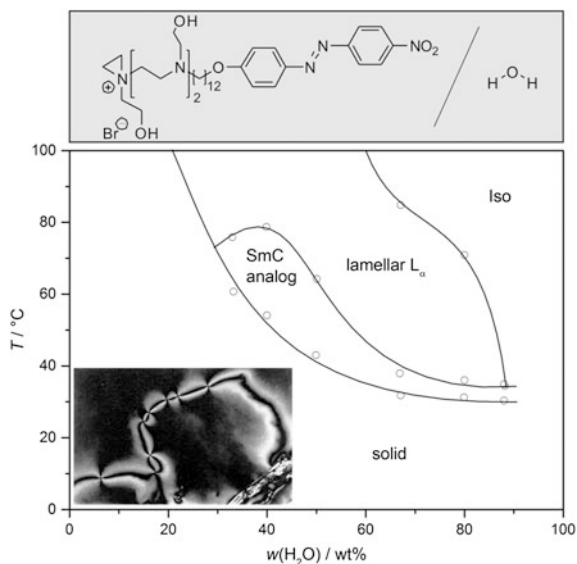


**Fig. 1.8** Phase diagram of 1-(2-hydroxyethyl)-1-(2-((2-hydroxyethyl)(2-((2-hydroxyethyl)(12-(4-((4-nitro-phenyl)diazenyl)phenoxy)dodecyl)amino)ethyl)amino)ethyl)aziridin-1-ium bromide and water (redrawn after [26]). The *inset* shows the texture between crossed polarizers of the lyotropic SmC analog phase (adapted from [26] with permission of the Royal Society of Chemistry)

The second example is a system composed of water and an ionic amphiphile which incorporates several ethylene imine units and hydroxyl groups [26]. The phase diagram is shown in Fig. 1.8. The lyotropic SmC analog phase is stabilized over a quite broad concentration range. To prove the correct phase assignment of the lyotropic SmC analog phase, the authors provided X-ray diffraction data as well as texture images, which exhibit the characteristic schlieren texture known from thermotropic SmC phases (*cf.* inset of Fig. 1.8).

Summing up, there are so far only two examples of lyotropic SmC analog phases to be found in literature. None of them has been investigated in detail. Thus, little is known about the necessary conditions for the formation of a lyotropic SmC analog phase, its structure or the influence of the solvent on its properties.

## References

1. P.G. de Gennes, J. Prost, *The Physics of Liquid Crystals*, 2nd edn. (Oxford University Press, New York, 1993)
2. A. Sánchez Castillo, *Polarized micro-Raman spectroscopy: A modern technique to study the molecular orientational order of nematic and smectic liquid crystals*. Doctoral thesis, Verlag Dr. Hut, München, 2013

3. F. Reinitzer, *Monatsh. Chem.* **9**, 421–441 (1888)
4. H.-D. Dörfler, *Grenzflächen und kolloid-disperse Systeme* (Springer, Berlin, 2002)
5. A. Blume, K. Hiltrop, K. Kratzat, T. Engels, W. von Rybinski, C.C. Möller-Goymann, in *Lyotrope Flüssigkristalle: Grundlagen, Entwicklungen, Anwendungen*, ed. by H. Stegemeyer (Steinkopferverlag, Darmstadt, 1999)
6. I.C. Sage, W.A. Crossland, T.D. Wilkinson, H.F. Gleeson, W.J. Leigh, M.S. Workentin, in *Applications in Handbook of Liquid Crystals, Vol. 1 : Fundamentals*, eds. by E. Demus, J. Goodby, G.W. Gray, H.-W. Spiess, V. Vill (Wiley-VCH Verlag GmbH, Weinheim, 1998)
7. K. Herrmann, *Trans. Faraday Soc.* **29**, 972–976 (1933)
8. G. Heppke, C. Bahr, *Flüssigkristalle*, in *Bergmann, Schaefer, Lehrbuch der Experimentalphysik, Vol 5: Vielteilchen – Systeme*, ed. by W. Raith (Walter de Gruyter, Berlin, 1992)
9. M. Krüger, *Kollektive Dynamik ferro- und antiferroelektrischer Flüssigkristalle in elektrischen Feldern*. Doctoral thesis, Mensch & Buch Verlag, Berlin, 2007
10. D. Vorländer, M.E. Huth, *Z. Physik, Chem.* **75**, 641–650 (1911)
11. A. Saupe, *Mol. Cryst. Liq. Cryst.* **7**, 59–74 (1969)
12. W. Helfrich, C.S. Oh, *Mol. Cryst. Liq. Cryst.* **14**, 289–292 (1971)
13. R.B. Meyer, L. Liébert, L. Strzelecki, P. Keller, *J. Phys. Lett.* **36**, L-69–L-71 (1975)
14. N.A. Clark, S.T. Lagerwall, *Appl. Phys. Lett.* **36**(11), 899–901 (1980)
15. S.T. Lagerwall, I. Dahl, *Mol. Cryst. Liq. Cryst.* **114**, 151–187 (1984)
16. J. Valasek, *Phys. Rev.* **17**, 475 (1921)
17. N.A. Clark, S.T. Lagerwall, United States Patent #4840463 (1988)
18. D. Joachimi, C. Tschierske, A. Öhlmann, W. Rettig, *J. Mater. Chem.* **4**(7), 1021–1027 (1994)
19. G. Platz, J. Pölike, C. Thunig, *Langmuir* **11**, 4250–4255 (1995)
20. N. Linder, M. Kölbl, C. Sauer, S. Diele, J. Jokiranta, C. Tschierske, *J. Phys. Chem. B* **102**, 5261–5273 (1998)
21. K. Kanie, J. Sekiguchi, X. Zeng, G. Ungar, A. Muramatsu, *Chem. Commun.* **47**, 6885–6887 (2011)
22. N. Pietschmann, A. Lunow, G. Brezesinski, C. Tschierske, F. Kuschel, H. Zschke, *Colloid Polym. Sci.* **269**, 636–639 (1991)
23. J.R. Bruckner, *Struktur und Chiralitätseffekte in lyotrop-flüssigkristallinen Phasen eines chiralen 1,2-Diols*. Diploma thesis, University of Stuttgart, 2010
24. J.R. Bruckner, D. Krueerke, J.H. Porada, S. Jagiella, D. Blunk, F. Giesselmann, *J. Mater. Chem.* **22**, 18198–18203 (2012)
25. M.A. Schafheutle, H. Finkelmann, *Liq. Cryst.* **3**(10), 1369–1386 (1988)
26. S. Ujiie, Y. Yano, *Chem. Commun.* 79–80 (2000)

## Chapter 2

# Aims and Scope of this Thesis

Thermotropic and lyotropic liquid crystals share a common state of matter with many analogies in their structural and physical properties. However, these two fields of liquid crystal research are usually treated completely separately. This is partially due to historical reasons, but also to striking differences in some aspects of these two classes of liquid crystals. One of these differences is the occurrence of thermotropic phases which do not have a lyotropic counterpart. A compelling example of this is the thermotropic ferroelectric SmC\* phase. Due to its unique chirality effects, i.e. ferroelectricity and a helical configuration of the tilt-direction, this phase attracted considerable scientific interest over the last decades. However, there are no reports found in literature about a SmC\* analog phase in lyotropic liquid crystals.

To bridge this gap between thermotropic and lyotropic liquid crystals, efforts were made in our research group for quite some time in the scope of the DFG project Gi243/4 to find a lyotropic analog of the SmC\* phase. Now, preliminary investigations in the framework of this thesis led to a promising series of diol molecules, which might exhibit this so far unknown phase. Based on this, the present thesis deals with the first discovery and description of a lyotropic analog of the SmC\* phase. Furthermore, the physical properties of this novel phase shall be investigated, especially with focus on its chirality effects. In detail, the following points will be addressed:

- Screening of promising surfactant/solvent systems for the formation of a lyotropic SmC\* analog phase and selection of proper systems for further investigations. In this process, necessary structural features of the surfactants and the solvents shall be elucidated.
- Measurement of the phase diagrams of the selected surfactant/solvent systems using polarized optical microscopy and characterization of all phases observed.
- Proof of the existence of the potential lyotropic smectic C\* analog phase using several independent methods.

- Detailed investigation of structural and physical properties of the lyotropic SmC\* analog phase by means of X-ray diffraction, tilt angle measurements and differential scanning calorimetry. The impact of changes in temperature and solvent concentration on the structure of the lyotropic SmC\* analog phase shall be analyzed.
- Study of potential chirality effects like the helical twist of the tilt-direction and ferroelectricity in the lyotropic analog of the SmC\* phase.
- Design of a first structural model of the lyotropic SmC\* analog phase.

# Chapter 3

## Thermotropic and Lyotropic Liquid Crystals

### Crystals

In this chapter, the structural properties of thermotropic and lyotropic liquid crystals will be compared. In a first step, the driving forces for the formation of the mesophases, as well as the building blocks of the two types of liquid crystals will be analyzed. Afterwards, the structures and properties of the most important liquid crystalline phases will be described, as far as they are important in the context of this thesis.

### 3.1 The Building Blocks

Even though lyotropic and thermotropic liquid crystals share the same state of matter, the driving forces for the formation of the mesophases differ substantially. To understand this, the molecules which form the respective liquid crystalline phases have to be examined in more detail. Figure 3.1 shows typical examples of such molecules.

Thermotropic liquid crystals are most often composed of elongated rod-like or plane disc-like organic molecules (*cf.* Fig. 3.1, top part). However, the molecules may also take other geometries as long as they are anisotropic, e.g. a banana-like shape as found for bent-core molecules [1]. This anisotropic shape is essential, as orientational order cannot be defined for building blocks with an isotropic shape.

Rod-shaped molecules forming liquid crystalline phases are called ‘calamitic’. A prominent example of such a calamitic molecule is terephthal-bis-(*p*-butylaniline) (TBBA) [2]. Its chemical structure is shown in the upper left corner of Fig. 3.1. The molecule possesses a rigid aromatic core as well as flexible alkyl chains. The aromatic core favors a parallel packing of the molecules, while the flexible chains keep them from crystallizing. These intermolecular interactions, as well as entropic effects and steric interactions between the mesogens, promote the formation of mesophases, as discussed by Onsager [3]. The mesophases formed by calamitic mesogens frequently possess a layered structure, but different phase types are also possible.

Disc-shaped molecules forming mesophases are called ‘discotic’. An example for such a discotic mesogen is benzene-hexa-*n*-octanoate (BH8) [4] which is depicted in the upper right corner of Fig. 3.1. Again, aromatic cores lead to a

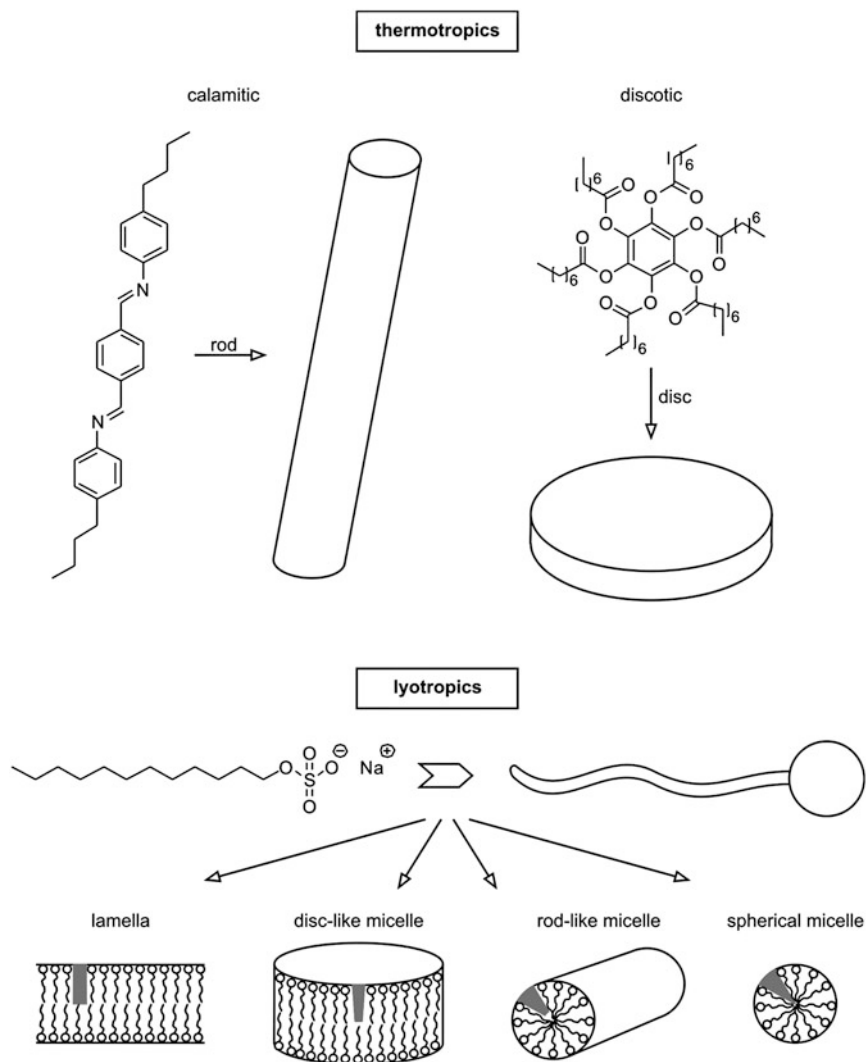


**Fig. 3.1** Building blocks of thermotropic and lyotropic liquid crystalline phases. The *upper part* of the figure shows two examples of typical thermotropic mesogens. Calamitic mesogens, such as terephthal-bis-(*p*-butylaniline) (TBBA) [2], can be represented by prolate ellipsoids or rigid rods, while discotic mesogens, such as benzene-hexa-*n*-octanoate (BH8) [4], are usually described by oblate ellipsoids or discs. The lower part of the figure shows the typical surfactant molecule sodium dodecyl sulfate (SDS), which forms lyotropic phases with water [5]. Such a surfactant molecule is basically composed of a polar head group and a flexible hydrophobic tail. These amphiphilic molecules aggregate into different types of micelles, which are the actual mesogens of lyotropic liquid crystals. The shape of the micelles depends mainly on the solvent concentration

stacking of the molecules due to core-core interactions and the alkyl chains hinder the crystallization. Consequently, the most favorable mesophases of discotic liquid crystals are columnar phases.

Summing up, the molecular interactions which cause the formation of mesophases are quite similar for both subtypes of thermotropic liquid crystals, i.e. intermolecular and steric interactions as well as entropic effects. Furthermore, for both types the mesogens which built up the mesophases are the molecules themselves.

Lytotropic liquid crystals are usually formed by amphiphilic molecules, i.e. surfactants, in mixtures with polar solvents. A common example of a surfactant forming lyotropic phases with water is sodium dodecyl sulfate (SDS) [5]. It is shown at the bottom of Fig. 3.1. The molecule holds a polar head group as well as an apolar alkyl tail. By dissolving surfactant molecules in water, the molecules cluster together into aggregates, the so-called micelles, which shield their apolar tails from the surrounding water. To understand this behavior, it is relevant to recall that the hydrogen bonds formed between water molecules are much stronger than the van der Waals forces between water molecules and the alkyl chains of the surfactant molecules. Due to this, if the surfactant is molecularly dissolved, the water molecules have to form cavities within the hydrogen bond network in which the alkyl chains are located. The formation of cavities only allows certain orientations of the water molecules, which causes a dramatic loss of entropy. Due to the connected thermodynamically unfavorable increase of the Gibbs free energy, the solvation of single molecules is impeded and thus the formation of micelles is promoted. This effect is called the ‘hydrophobic effect’ or, in more general terms, it is also denoted as ‘solvophobic effect’.

In lyotropic liquid crystals these micelles are the mesogens which built up the liquid crystalline phases. Depending on the solvent concentration, different types of micelles are possible. The most common micelles, i.e. rod-like micelles, disc-like micelles and spherical micelles, are depicted in the lower part of Fig. 3.1. Furthermore, the surfactant molecules may also aggregate into lamellas which represent full or partially interdigitated bilayers of the molecules. Those lamellas are, strictly speaking, no micelles as they extend infinitely into two dimensions, but yet the driving force for their formation is the same.

The reason for the formation of different types of micelles is the effective shape of the surfactant molecules. This effective shape is indicated in gray in the respective micelles in Fig. 3.1 and is also shown in more detail in Fig. 3.2. Due to the increasing solvation of the amphiphiles’ polar headgroups, the head groups become effectively bulkier and bulkier by raising the solvent concentration. Thus, at high solvent concentrations spherical micelles are preferred, which require a conic effective shape of the amphiphiles, while lamellas are formed at low solvent concentrations at which the amphiphiles possess a cylindrical effective shape. A mathematical description of this is given by the packing parameter  $\Pi$  [6], which relates the effective volume  $V$  of the amphiphile to the length  $l$  of the hydrophobic chain and the cross-section area  $a_{cs}$  of the polar head group:



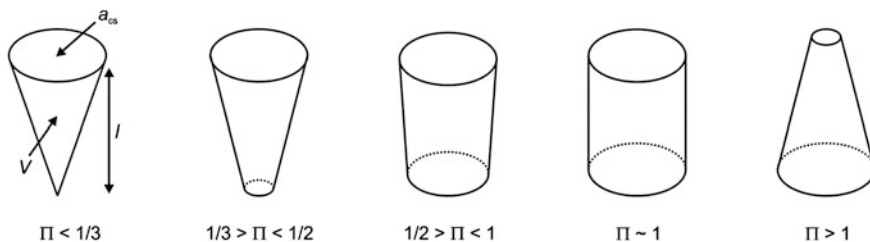


**Fig. 3.2** Effective amphiphile shapes and corresponding packing parameters  $\Pi$

$$\Pi = \frac{V}{l \cdot a_{cs}}. \quad (3.1)$$

For values of the packing parameter  $\Pi$  smaller than  $1/3$ , spherical micelles can be expected. For values up to  $1/2$ , rod-like micelles are most likely, followed by disc-like micelles at increasing values of  $\Pi$ . For values of approximately 1 the formation of lamellas dominates. At very low solvent concentrations or if using apolar solvents the packing parameter may take values larger than 1. Under these conditions inverse micelles are formed. They look similar to the micelles shown in Fig. 3.1, but instead of the alkyl chains, the hydrophilic head groups are located in the centers of the micelles.

In conclusion, thermotropic and lyotropic liquid crystalline phases are built up by mesogens with rather similar shapes, e.g. rods or discs. However, in the case of thermotropics, the mesogens are single molecules, while in lyotropics they are micelles which form due to the hydrophobic effect. Even though the driving forces for the formation of the two types of mesophases are rather different, it is not astonishing that analog phases emerge quite often, in view of the similar symmetry and shapes of the mesogens. To point out the analogies, a comparative synopsis of the most important mesophases of thermotropic and lyotropic liquid crystals will be given in the following section.

### 3.2 Survey of Important Mesophases

In general, there are three main types of liquid crystalline phases. All of them appear in thermotropic as well as in lyotropic liquid crystals in one or another variation. Unfortunately, due to historical reasons, the nomenclature of thermotropics [7, 8] and lyotropics [9, 10] is not uniform, making it sometimes complicated to identify analog phases. For the sake of clarity, the notation of thermotropics is sometimes adopted for lyotropics within this thesis.

The first mesophase type is represented by the nematic phase or its chiral variant, the so-called cholesteric phase, which is fluid in all three dimensions of space. The second type is defined by layered phases, which are two-dimensionally fluid. They

are denoted as smectic in thermotropics and as lamellar in lyotropics. The last type of liquid crystalline phases, which possess a fluid-like order in one dimension of space only, is frequently called columnar in thermotropics as well as in lyotropics. However, in lyotropic liquid crystals such two-dimensionally correlated mesophases are also referred to as ribbon phases.

In Table 3.1 analogies between some thermotropic and lyotropic mesophases are pointed out. Only mesophases commonly accepted in literature are included in this synopsis. It is classified into the three major mesophase types discussed previously. From this comparison it is obvious, that there is a considerable amount of thermotropic mesophases, mainly smectics, for which no lyotropic analog is known.

A more detailed description of the structure and properties of the mesophases in Table 3.1 is provided in the following subchapters. In principal, the properties and textures of analog phases are also similar due to the equivalent structure of the mesophases and thus are discussed simultaneously. However, the textures of lyotropic liquid crystals often appear less colorful. This is due to the lack of aromatic units in most of the typically used surfactant molecules, as the aromatic cores of thermotropic liquid crystal largely contribute to their birefringence. Exemplary texture images of the discussed thermotropic mesophase are shown in Refs. [11, 12], while texture images of lyotropic mesophases are found in Refs. [13, 14, 15].

### 3.2.1 *The Nematic Phases*

Of all liquid crystalline phases, the nematic phase is the phase with the highest symmetry, i.e.  $D_{\infty h}$ , and the least order. As shown in Fig. 3.3a, b, the mesogens solely possess orientational order. Positional order of the mass centers does not occur in this phase. Nematic phases are usually built up by either rod-like or disc-like mesogens. For thermotropic liquid crystals these mesogens are therefore calamitic or discotic molecules, respectively. In both cases the phase is simply denoted with the abbreviation N. For lyotropics, the notation typically distinguishes between nematic phases  $N_C$ , which are formed by rod-like micelles, and nematic phases  $N_D$ , which are composed of disc-like micelles.

Nematic phases typically show a schlieren texture between crossed polarizers if the director is oriented perpendicular to the viewing direction. One feature of the schlieren texture is the occurrence of topological point defects. At these point defects either two or four dark brushes meet. The corresponding defects are denoted as  $\pm 1/2$  or  $\pm 1$ , respectively. Further characteristic textures of the nematic phase are the thread-like texture, which exhibits  $\pi$  disclinations parallel to the substrate, and the marble texture, in which areas of differing uniform director orientations occur.

If the nematic phase is composed of chiral molecules, a chiral nematic phase ( $N^*$ ) forms, which is synonymous with a cholesteric phase. The chiral version of the N phase still only possesses orientational order, but additionally it exhibits a helical superstructure. A sketch of this helical precession of the director orientation is depicted in Fig. 3.3c, d. The precession of the local director  $\mathbf{n}_{\text{local}}$  may either be

**Table 3.1** Analogies between some thermotropic and lyotropic mesophases

degree of fluidity generic term	thermotropic		lyotropic	
	achiral	chiral	achiral	chiral
3D nematic	nematic (N)	chiral nematic / cholesteric (N*)	nematic (N) (composed of rod- like (N <sub>C</sub> ) or disk- like micelles (N <sub>D</sub> ))	chiral nematic / cholesteric (N*) (composed of rod- like (N <sub>C</sub> <sup>*</sup> ) or disk- like micelles (N <sub>D</sub> <sup>*</sup> ))
2D smectic	smectic A (SmA)	chiral smectic A (SmA*)  twist grain boundary A* (TGBA*)	lamellar L <sub>α</sub> (L <sub>α</sub> )	
	smectic C (SmC*)	chiral smectic C (SmC*)  twist grain boundary C* (TGBC*)		
	hexatic smectics (SmB, SmF, SmI)	chiral hexatic smectics (SmF*, SmI*)		
	Modulated antiphases (Sm $\tilde{A}$ , Sm $\tilde{C}$ )			
1D columnar	columnar hexagonal (Col <sub>h</sub> )		hexagonal (H <sub>α</sub> )	
	columnar rectangular (Col <sub>r</sub> )		rectangular (R)	
	columnar oblique (Col <sub>ob</sub> )		monoclinic (M <sub>α</sub> )	

Blank fields represent mesophases, for which usually no distinction is made in literature between the chiral and the achiral version. Hatched fields indicate that the respective mesophase does not exist or is not commonly accepted in literature

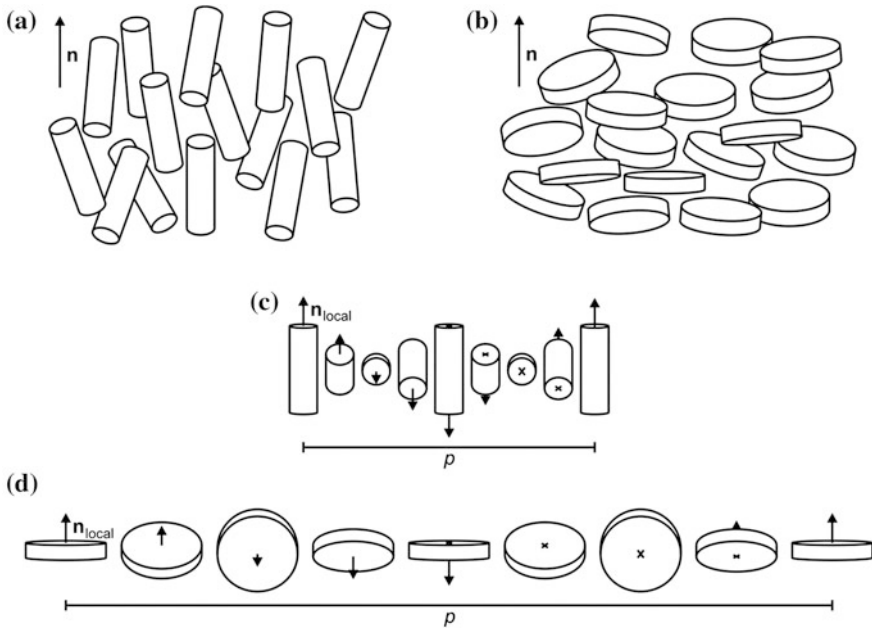


**Fig. 3.3** Structural sketches of nematic phases composed of **a** calamitic and **b** discotic mesogens with indicated direction of the director  $\mathbf{n}$ . In the sketches of the corresponding cholesteric phases of **c** calamitic and **d** discotic mesogens, only the local director  $\mathbf{n}_{\text{local}}$  is drawn in

right- or left-handed. The distance necessary for its rotation of  $2\pi$  corresponds to the helical pitch  $p$ . The pitch  $p$  usually takes values in the order of  $10^{-1} - 10^{+1} \mu\text{m}$  [12].

The helical superstructure of the  $N^*$  phase strongly influences the properties and textures of the mesophase compared to its achiral version. One example for this is the selective reflection of light leading to an iridescent appearance of the sample if the value of  $p$  is in the range of visible light. A second consequence is the occurrence of the so-called fingerprint texture, which can be seen between crossed polarizers if the sample is aligned in a manner that the helix axis is perpendicular to the viewing direction. Along with the helical modulation of the local director  $\mathbf{n}_{\text{local}}$ , the effective birefringence changes gradually. This leads to the occurrence of a striped pattern of dark and light lines. As  $\mathbf{n}$  is equivalent to  $-\mathbf{n}$ , the distance between two lines of equal brightness corresponds to  $p/2$ . If the value of  $p$  is very small, a fan-like texture may appear instead of the fingerprint texture. This texture looks similar to a texture typically observed for SmA phases and reflects the layer-like arrangement of the twisted mesogens. If the helix axis is aligned parallel to the viewing direction, a so-called oily streak texture occurs, in which the oily streaks correspond to small areas with a deviating alignment. If the upper and lower boundaries of such a sample are not parallel to each other but tilted, as it is the case in a wedge cell, Grandjean steps form, which originate from sudden changes in the number of helical turns within the cholesteric sample. The value of  $p$  can therefore

be deduced from the distance between the Grandjean steps, if the angle of the wedge cell is known.

### 3.2.2 The Smectic Phases

Smectic phases are characterized by a layered structure, in which a two-dimensional fluid order prevails. In Fig. 3.4a, a schematic picture of the skeleton structure of a smectic phase is shown. The two-dimensional fluid layers are stacked upon each other with the periodicity distance  $d$ , causing a one-dimensional positional order along the direction of the layer normal  $\mathbf{k}$ . In the case of the lyotropic lamellar  $L_\alpha$  phase one smectic layer is usually referred to as a lamella. The lamella can be separated into two parts, as shown in Fig. 3.4b. The first part is a surfactant bilayer, in which the molecules are on the average oriented perpendicular to the layer plane. For conventional lyotropic mixtures polar solvents are used, which cause the hydrophobic chains to point towards the middle of the bilayers. This arrangement can be inverted by using apolar solvents, i.e. alkyls. If the surfactant molecules are interdigitated to some degree, the term ‘partial bilayer’ is used. The second part of the lamella is a layer of solvent molecules, in which the molecules are believed to solely possess a fluid-like order. The solvent layers separate the surfactant bilayers from each other and should thus inhibit the transfer of information from one surfactant layer to the next. Consequently, the lamellar  $L_\alpha$  phase is the only fluid,

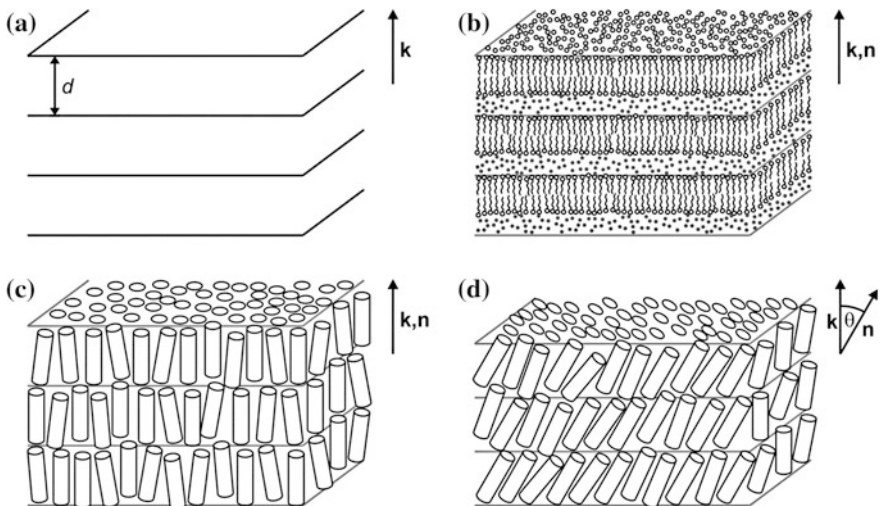


**Fig. 3.4** Sketch of **a** the skeletal structure of all smectic phases with indicated periodicity distance  $d$  and direction of the layer normal  $\mathbf{k}$ , **b** the lamellar  $L_\alpha$  phase with indicated directions of the layer normal  $\mathbf{k}$  and the director  $\mathbf{n}$ , **c** the SmA phase and **d** the SmC phase in which the layer normal  $\mathbf{k}$  and the director  $\mathbf{n}$  include the tilt angle  $\theta$

layered mesophase in lyotropics, which is commonly observed and accepted. Furthermore, a distinction in the denotation between lamellar  $L_\alpha$  phases with and without chiral molecules is not made, as no significant differences in their properties have been observed so far.

The SmA phase, which is depicted in Fig. 3.4c, is the thermotropic analog of the lamellar  $L_\alpha$  phase. The mesogens within the smectic layers are again oriented perpendicular to the layer planes, causing  $\mathbf{n}$  and  $\mathbf{k}$  to be parallel. Usually, the smectic layer thickness  $d$  corresponds directly to the molecular length  $L$  [16], if the smectic phase is composed of single layers (SmA<sub>1</sub>). It is also possible to find values for  $d$  up to  $2L$ , if bilayers (SmA<sub>2</sub>) or partial bilayers (SmA<sub>d</sub>) are formed. This normally happens for strongly polar or amphiphilic molecules [17]. The quality of the translational order of the mesogens within the smectic layers can be described with the smectic order parameter  $\Sigma$  which is defined as [18]:

$$\Sigma = \left\langle \cos\left(\frac{2\pi}{d} z_i\right) \right\rangle. \quad (3.2)$$

In this equation  $z_i$  describes the position of a mesogen  $i$  with respect to the  $z$ -axis of Cartesian coordinate system in which  $\mathbf{z}$  is parallel to the layer normal  $\mathbf{k}$  and  $d$  is the smectic layer thickness. For a hypothetical mesophase with a perfect smectic order,  $\Sigma$  would take a value of  $\Sigma \approx 1$ . For real SmA phases, typical values are  $\Sigma \approx 0.7$  [19, 20].

The structure of the SmA phase does not change if the mesogens are chiral, but some of its properties do, e.g. the response to an applied electric field [21]. Therefore, the chiral SmA phase is denoted as SmA\*. Between crossed polarizers, the SmA, the SmA\* as well as the lamellar  $L_\alpha$  phase initially form so-called bâtonnets under planar anchoring conditions if emerging directly from the isotropic phase. These bâtonnets then condense into a focal conic fan-shaped texture. If the director is oriented parallel to the viewing direction, the texture appears black between crossed polarizers, which is referred to as ‘homeotropic’. It is also possible to find oily streaks within the homeotropic texture, if the alignment of the sample is imperfect.

The SmC phase basically possesses the same structure as the SmA phase with the difference that the mesogen are on the average tilted by the tilt angle  $\theta$  with respect to the layer normal  $\mathbf{k}$ . Hence, the director  $\mathbf{n}$  is also tilted by  $\theta$ . The tilt angle increases with decreasing temperature until reaching a saturated value. Typical values for the saturated tilt angle lie between  $25^\circ$  and  $35^\circ$  [12]. If the high temperature phase is a N phase, the phase transition to the SmC phase is usually of 1st order. In consequence, the tilt angle as well as the order parameters escalate directly after the phase transition. Whereas, if the high temperature phase is a SmA phase, the phase transition is most often of 2nd order. In this case, the tilt angle as well as the order parameters increase continuously.

In the course of the tilting of the mesogens, the smectic layer thickness  $d$  shrinks with respect to the SmA phase. This can already be seen by simply comparing

Fig. 3.4c, d. The layer thickness  $d(\text{SmC})$  in the SmC phase is connected to the thickness  $d(\text{SmA})$  in the SmA phase via the equation

$$d(\text{SmC}) = d(\text{SmA}) \cdot \cos(\theta). \quad (3.3)$$

A further consequence of the director tilt is that the fan-shaped texture of the SmA phase turns into a broken fan-shaped texture in the SmC phase. In very thin, planarly oriented samples only the two tilt directions are favored, which allow the director  $\mathbf{n}$  to be parallel to the sample boundaries, leading to the formation of clearly separated tilt domains [22]. Furthermore, characteristic defects appear, which are called zigzag defects and are related to the shrinkage of the smectic layer thickness [23]. If the layer normal  $\mathbf{k}$  is oriented along the viewing direction, the SmC phase exhibits a schlieren texture, due to its biaxiality. In contrast to the schlieren texture of the N phase, all point singularities of the SmC schlieren texture are of the  $s = \pm 1$  type. Lyotropic analogs of the SmC phase are only known in exceptional cases (*cf.* Sect. 1.3).

Compared to its achiral variant, the chiral SmC\* phases exhibits a considerably modified structure and properties (*cf.* Sect. 1.2). The introduction of chiral mesogens causes a breaking of the symmetry from  $C_{2h}$  to  $C_2$  as well as the formation of a helical superstructure with the helix axis parallel to the layer normal  $\mathbf{k}$  (*cf.* Fig. 1.2b). Therefore, the SmC\* phase may exhibit selective reflection of circularly polarized light in analogy to the N\* phase, if the value of the pitch  $p$  is in the same order as the wavelength of the irradiated light. Furthermore, in addition to the textures observed for SmC phases, the SmC\* phase may show a striped texture, which is caused by the spatial modulation of the effective birefringence along the direction of the helix axis and is often referred to as ‘pitch lines’.

Besides the SmA and the SmC phases in which the molecules are two-dimensionally fluid within the layers, there are also smectic phases which exhibit some degree of intra-layer order. Those phases are called hexatic smectics. Within the smectic layers of the hexatic smectic phases a local hexagonal arrangement of the mesogens is found, which possess a long-range orientational order. However, in contrast to a hexagonal crystalline phase, which is depicted in Fig. 3.5a, the hexagonal arrangement in hexatic smectic phases does not show a long-range positional order [24, 25]. This situation is denoted with the term ‘bond-orientational order’ and is illustrated in Fig. 3.5b. The mesogens within the layers may in average either be parallel (SmB) or tilted (SmI, SmF) with respect to the layer normal. For the tilted hexatic smectic phases a distinction between achiral and chiral phases (SmI\*, SmF\*) is made.

In lyotropics, phases with a structure comparable to the ones of the thermotropic hexatic smectic phases exist, as pointed out by Smith et al. [26]. Again, the surfactant molecules show a bond-orientational order within the layers and can either be parallel (lamellar  $L_\beta$ ) [27] or tilted (lamellar  $L_\beta'$ ) [28] with respect to the layer normal  $\mathbf{k}$ . These phases are called gel-like rather than liquid crystalline, due to their dramatically increased viscosity compared to the lamellar  $L_\alpha$  phase. This increased



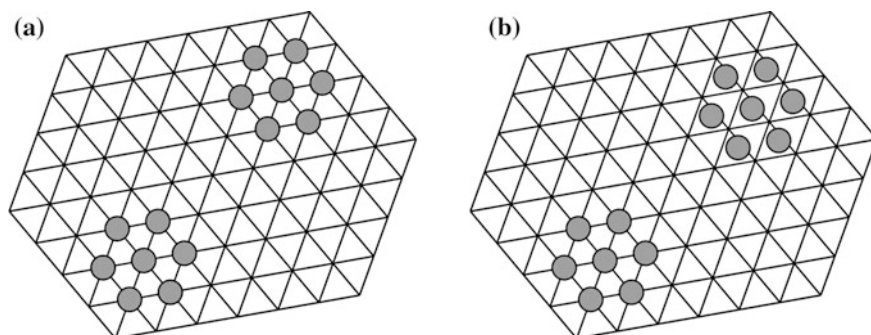


**Fig. 3.5** **a** Long-range orientational and positional order as found for a crystal. **b** Hexatic smectic phase with long-range orientational but only short-range positional order (redrawn after [24])

viscosity can be explained by the all-trans confirmation of the surfactants' alkyl chains, which is also referred to as 'frozen'.

In some cases, chiral liquid crystals which possess a very strong tendency to segregate into smectic layers and at the same time exhibit a very high twisting power form so-called twist grain boundary phases (TGB) [29]. This kind of mesophase represents a connecting link between smectic and nematic phases. In Fig. 3.6 a sketch of the TGBA\* phase is shown. The TGBA\* phase is composed of smectic blocks, which possess locally the same structure as the SmA\* phase. However, the individual blocks are twisted with respect to each other causing the formation of a helical superstructure with the helix axis being perpendicular to the layer normal  $\mathbf{k}$ . A full rotation of the smectic blocks of  $2\pi$  corresponds to the pitch length  $p$ . The smectic blocks are separated from each other by grain boundaries, which are formed by regular arrays of screw dislocations. Several types of TGB phases are known, e.g. the TGBC\* phase, which has a local SmC\* structure or the undulated twist grain boundary phase (UTGBC\*). TGB phases usually appear

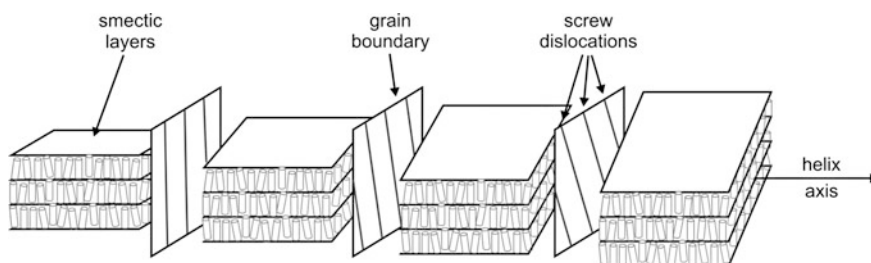


**Fig. 3.6** Structure of the TGBA\* phase. The phase is built up by blocks of smectic layers, which are slightly rotated with respect to the adjacent blocks. The blocks are separated from each other by grain boundaries, which are composed of regular sets of screw dislocations. The distance necessary for a rotation of the smectic blocks of  $2\pi$  is equivalent to the pitch  $p$ . The helix axis always lies within the layer planes, independently of the orientation of the individual smectic block



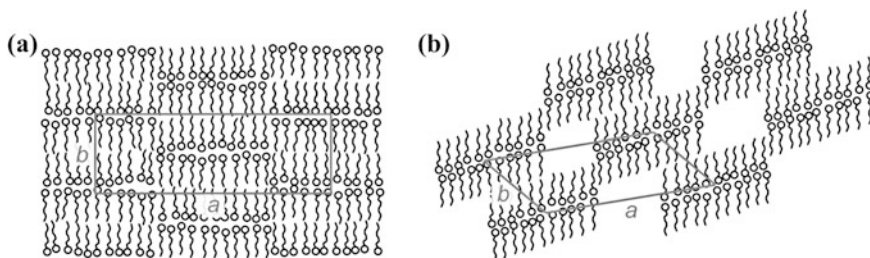


**Fig. 3.7** Sketch of the modulated smectic phases. For the sake of clarity, the sinusoidal modulations are drawn in an exaggerated way. **a** Shows the  $Sm\tilde{A}$  phase, which is described with a centered rectangular lattice and **b** shows the  $Sm\tilde{C}$  phase in which the mesogens are found on an oblique lattice

between  $N^*$  phases and smectic phases and are typically stable only within the range of a few Kelvin. If the helix axis is aligned perpendicular to the viewing direction, the  $TGBA^*$  phase exhibits a filament texture similar to the fingerprint texture of the  $N^*$  phases but much more pronounced due to the existence of the grain boundaries. If the helix axis is oriented parallel to the viewing direction, a Grandjean texture is often observed. Up to now only thermotropic TGB phases are known, even though the existence of a lyotropic TGB phase was already predicted in 1997 by Kamien and Lubensky [30]. In this lyotropic TGB phase the smectic blocks should possess the same local structure as known from the lamellar  $L_\alpha$  phase.

A link between the one-dimensionally correlated smectic phases and the two-dimensionally correlated columnar phases is given by the modulated smectic phases, which are also sometimes referred to as antiphases. Modulated phases are formed by amphiphilic [31, 32] or strongly polar mesogens, e.g. mesogens with cyano or nitro groups [33–35]. Due to their polarity, the mesogens arrange into bilayers similar to lyotropic lamellar phases. Modulated phases however only occur in thermotropics. In contrast to the already discussed smectic phases, the bilayers are not straight but undulated. A distinction between the  $Sm\tilde{A}$  and the  $Sm\tilde{C}$  is made, in analogy to the orthogonal  $SmA$  and the tilted  $SmC$  phase.  $Sm\tilde{A}$  phases most often possess a centered rectangular structure, while  $Sm\tilde{C}$  phases exhibit an oblique lattice as shown in Fig. 3.7.

### 3.2.3 The Columnar Phases

Columnar phases are typically formed by either thermotropic liquid crystals made up of discotic mesogens stacking upon each other to form columns or by lyotropic liquid crystals composed of rod-like micelles. These columns or rods arrange into two-dimensionally correlated structures. Alongside the long axis of the columns

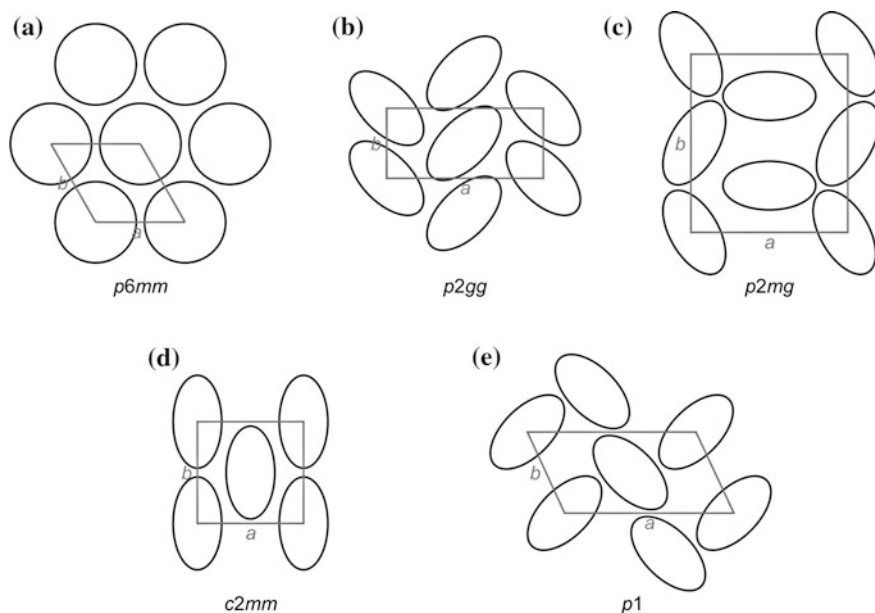


**Fig. 3.8** Sketch of the cross sections of the most common columnar phases, showing **a** the structure of the hexagonal columnar phase, **b–d** columnar phases with rectangular lattices and **e** of an oblique columnar phase. For every structure the unit cells as well as the corresponding plane crystallographic groups are given

there is no long-range positional correlation between the molecules, making the columnar phases one-dimensionally fluid. Depending on the symmetry of the two-dimensional lattice, different types of columnar phases are distinguished. In Fig. 3.8 the structure and symmetry of the most common columnar phases are depicted. They can either possess a hexagonal, a rectangular or an oblique symmetry and are categorized corresponding to their plane group symmetry [36]. In thermotropics the abbreviation for a columnar phase is simply Col. The symmetry of the explicit columnar phase can be indicated by the subscript crystallographic group. In lyotropics the symbols for the individual columnar phases differ for every lattice type. The abbreviation for the hexagonal phase is  $H_{\alpha}$ , for rectangular phases R is used and the oblique columnar phase is denoted with  $M_{\alpha}$ .

The most fundamental columnar phase is the hexagonal phase. In this phase the columns pack into a highly symmetrical hexagonal arrangement. If the cross section of the columns deviates from a perfect circular shape, e.g. because the discs are tilted within the columns, a hexagonal arrangement is not possible. Thus, such columns typically form rectangular or oblique lattices to avoid this unfavorable situation.

Between crossed polarizers, the phase transition into a columnar phase is often accompanied by a dendritic growth of the texture. If the director is oriented perpendicular to the viewing direction, pseudo-focal conic fan-shaped textures can be observed. If the viewing direction is parallel to the director, a platelet texture is formed.

### 3.2.4 Phase Sequences of Thermotropic and Lyotropic Liquid Crystals

The appearance of specific liquid crystalline phases and especially the sequence in which they occur is not random but follows certain rules. As the driving forces behind the formation of thermotropic and lyotropic liquid crystalline phases differ from each other, these rules are also different for the two types of liquid crystals.

In thermotropic liquid crystals, the formation of particular mesophases depends mainly on the temperature. On cooling, the structure of the mesophases becomes more and more ordered and thus less symmetric. For thermotropic mesophases formed by calamitic mesogens a fixed sequence was found [37, 38]:

isotropic  $\rightarrow$  N  $\rightarrow$  TGB  $\rightarrow$  SmA  $\rightarrow$  SmC  $\rightarrow$  SmB  $\rightarrow$  SmI  $\rightarrow$  SmF  $\rightarrow$  soft crystalline  $\rightarrow$  crystalline

Of course not all of these mesophase have to appear in a single liquid crystalline system. For very few liquid crystals, exceptions from this sequence rule are known to exist. In these liquid crystals a mesophase with a higher symmetry reappears on cooling, even though a less symmetric mesophase has already formed at higher temperatures. Such phases are called re-entrant and are indicated with a subscript 'RE'. Re-entrant behavior was first observed for a N–SmA–N<sub>RE</sub>–Cr phase sequence [39], but it was also found for other types of mesophases [40, 41]. It is not completely clarified when and why re-entrant phases appear. Different approaches to explain the re-entrant behavior were made, e.g. on the basis of frustration, geometric complexity or competing fluctuations [42, 43].

For lyotropic liquid crystals, the temperature plays a secondary role in the formation of the individual mesophases. The primary influence on the phase sequence is exerted by the solvent concentration. The solvent concentration is directly connected to the packing parameter and thus to the micellar shape (*cf.* Sect. 3.1), which largely determines the mesophase type. At low solvent concentrations lamellar phases are usually formed. By increasing the solvent concentration, columnar and nematic phases appear. At very high solvent concentrations an isotropic micellar solution dominates. An illustration of this phase behavior is shown in the theoretical phase diagram depicted in Fig. 3.9 (*cf.* [14]). The individual phases in Fig. 3.9 are separated by biphasic regions.

In some cases it is also possible to observe the formation of inverse micelles at very low solvent concentrations. This leads to a mirror imaged phase diagram of the one shown in Fig. 3.9. Even though the solvent concentration is the most important parameter for the occurrence of particular mesophases, the effect of temperature is not completely negligible. Hence, it is also possible to find high and low temperature mesophases at the same solvent concentration.

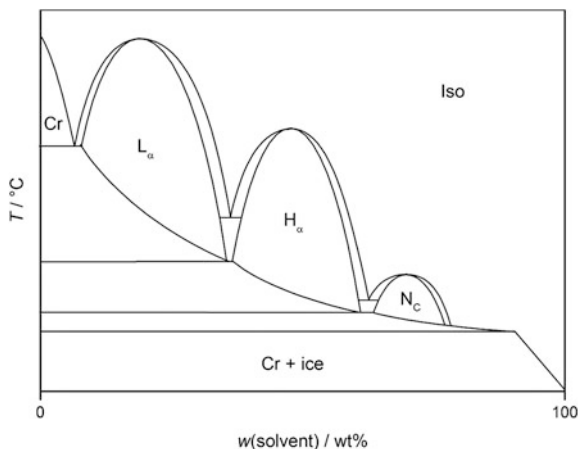


**Fig. 3.9** Theoretical phase diagram of a lyotropic liquid crystal. The phase transition from one lyotropic liquid crystalline phase into another mainly depends on the solvent concentration

## References

1. Y. Matsunaga, S. Miyamoto, *Mol. Cryst. Liq. Cryst.* **237**, 311–317 (1993)
2. D. Demus, H. Demus, H. Zschke, *Flüssige Kristalle in Tabellen*, 1st edn. (VEB Deutscher Verlag für Grundstoffindustrie, Leipzig, 1974)
3. L. Onsager, *Ann. N. Y. Acad. Sci.* **51**, 627–659 (1949)
4. S. Chandrasekhar, B.K. Sadashiva, K.A. Suresh, *Pramana* **9**(5), 471–480 (1977)
5. P. Kékicheff, C. Gabrielle-Madelmont, M. Ollivon, *J. Colloid Interface Sci.* **131**, 112–132 (1987)
6. J.N. Israelachvili, D.J. Mitchell, B.W. Ninham, *J. Chem. Soc., Faraday Trans.* **2**(72), 1525–1568 (1976)
7. G. Friedel, *Ann. Phys.* **18**, 273–474 (1922)
8. M. Barón et al., *Pure Appl. Chem.* **73**(5), 845–895 (2001)
9. V. Luzzati in *Biological Membranes*, vol. 1, ed. by D. Chapman (Academic Press, London, 1968)
10. T. Gulik-Krzywicki, E. Rivas, V. Luzzati, *J. Mol. Biol.* **27**, 303–322 (1967)
11. D. Demus, L. Richter, *Textures of Liquid Crystals*, 2nd edn. (VEB Deutscher Verlag für Grundstoffindustrie, Leipzig, 1978)
12. I. Dierking, *Textures of Liquid Crystals* (WILEY-VCH Verlag GmbH & Co KGaA, Weinheim, 2003)
13. H.-D. Dörfler, *Grenzflächen und kolloid-disperse Systeme* (Springer, Berlin, 2002)
14. A. Blume, K. Hiltrop, K. Kratzat, T. Engels, W. von Rybinski, C.C. Möller-Goymann, in *Lyotrope Flüssigkristalle: Grundlagen, Entwicklungen, Anwendungen*, ed. by H. Stegemeyer (Steinkopffverlag, Darmstadt, 1999)
15. S.T. Hyde, in *Identification of Lyotropic Liquid Crystalline Mesophases*, ed. by K. Holmberg, D.O. Shah, M.J. Schwuger. *Handbook of Applied Surface and Colloid Chemistry*, vol 2 (Wiley, West Sussex, 2002)
16. Y. Kosaka, T. Kato, T. Uryu, *Liq. Cryst.* **18**(5), 693–698 (1995)
17. G.S. Attard, R.W. Date, C.T. Imrie, D.R. Luckhurst, S.J. Roskilly, J.M. Seddon, L. Taylor, *Liq. Cryst.* **16**(4), 529–581 (1994)
18. W.L. McMillan, *Phys. Rev. A* **4**(3), 1238–1246 (1971)

19. E.F. Gramsbergen, W.H. De Jeu, *Liq. Cryst.* **4**(4), 449–455 (1989)
20. Y. Takanishi, A. Ikeda, H. Takezoe, A. Fukuda, *Phys. Rev. E* **51**(1), 400–406 (1995)
21. S. Garoff, R.B. Meyer, *Phys. Rev. Lett.* **38**, 848–851 (1977)
22. N.A. Clark, M.A. Handschy, S.T. Lagerwall, *Mol. Cryst. Liq. Cryst.* **94**, 213–234 (1983)
23. N.A. Clark, T.P. Rieker, J.E. MacLennan, *Ferroelectrics* **85**(1), 79–97 (1988)
24. P.M. Chaikin, T.C. Lubensky, *Principles of Condensed Matter Physics*, 2nd edn. (Cambridge University Press, Cambridge, 1997)
25. J.M. Seddon, in *Structural Studies of Liquid Crystals by X-Ray Diffraction Handbook of Liquid Crystals*, vol. 1, ed. by Fundamentals: E. Demus, J. Goodby, G.W. Gray, H.-W. Spiess, V. Vill (WILEY-VCH Verlag GmbH, Weinheim, 1998)
26. G.S. Smith, E.B. Sirota, C.R. Safinya, R.J. Plano, N.A. Clark, *J. Chem. Phys.* **92**(7), 4519–4529 (1990)
27. J.M. Seddon, K. Harlos, D. Marsh, *J. Bio. Chem.* **258**(6), 3850–3854 (1983)
28. A. Tardieu, V. Luzzati, *J. Mol. Biol.* **75**, 711–733 (1973)
29. H.-S. Kitzerow, in *Twist Grain Boundary Phases* ed. by H.-S. Kitzerow, C. Bahr. Chirality in Liquid Crystals (Springer, New York, 2001)
30. R.D. Kamien, T.C. Lubensky, *J. Phys. II* **7**, 157–163 (1997)
31. A.E. Skoulios, V. Luzzati, *Acta Cryst.* **14**, 278–286 (1961)
32. V. Luzzati, A. Tardieu, *Ann. Rev. Phys. Chem.* **25**, 79–94 (1974)
33. F. Hardouin, G. Sigaud, N.H. Tinh, M.F. Achard, *J. Phys. Lett.* **42**, L63–L66 (1981)
34. F. Sigaud, F. Hardouin, M.R. Achard, A.M. Levelut, *J. Phys.* **42**, 107–111 (1981)
35. F. Hardouin, N.H. Tinh, M.F. Achard, A.M. Levelut, *J. Phys. Lett.* **43**, L327–L331 (1982)
36. H. Arnold et al., in *International Tables of Crystallography*, vol. A, 5th edn. ed. by T. Hahn (Wiley, 2005)
37. H. Sackmann, *Liq. Cryst.* **5**(1), 43–55 (1989)
38. D. Demus, in *Sequence Rule and Reentrant Behavior* ed. by H. Stegemeyer. Liquid Crystals (Steinkopf Verlag, Darmstadt, Springer Verlag, New York, 1994)
39. P.E. Cladis, *Phys. Rev. Lett.* **35**(1), 48–51 (1975)
40. Y. Nishihata, H. Sakashita, H. Terauchi, S. Takenaka, S. Kusabayashi, *J. Phys. Soc. Jpn.* **55**(3), 853–859 (1986)
41. E. Fontes, P.A. Heiney, J.L. Haseltine, A.B. Smith, *J. Phys.* **47**, 1533–1539 (1986)
42. P.E. Cladis, *Mol. Cryst. Liq. Cryst.* **165**, 85–121 (1988)
43. S. Singh, *Phase Transitions* **72**, 183–209 (2000)

# Chapter 4

## Materials and Experimental Techniques

In this chapter the materials as well as the preparation of samples for further investigations will be described. Additionally, experimental techniques for all applied methods will be explained in detail.

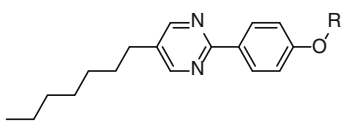
### 4.1 Materials and Preparation of Samples

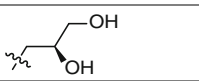
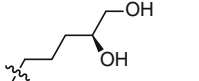
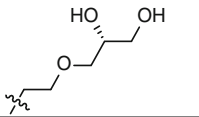
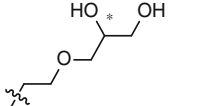
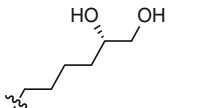
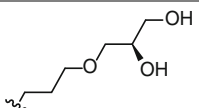
A series of similar surfactant molecules, which differ only in the length and composition of a linking unit, was investigated. The chemical structures and systematic names of the molecules are shown in Table 4.1. For a simplified handling, the surfactant molecules are denoted with the abbreviations given in Table 4.1.

The basic motif of all surfactant molecules used is a 2-phenylpyrimidine core with a heptyl chain attached to the 5-position of the pyrimidine ring. All surfactant molecules possess a terminating 1,2-diol unit as hydrophilic headgroup. This headgroup is connected to the phenyl ring via an ether bond and varying lengths of linking alkyl or alkoxy chains. At room temperature all substances are white, flaky solids. The enantiomeric excess of C3, C5O and C6O is in each case 99 %, due to the synthetic route. The diols C5 and C6 have an enantiomeric excess of 66 or 78 %, respectively. The substances were synthesized and kindly provided by Dr. Jan H. Porada, except for the surfactant C6, which was synthesized by Diana Zauser in collaboration with Dr. Jan H. Porada. Details on the synthesis of C5 and C5O are found in reference [1] or [2], respectively.

Most of the solvents used were commercially available and were bought in the highest available purity. Double distilled water was provided by the chemical-technical service of the Institute of Physical Chemistry at the University of Stuttgart. Details on all solvents are listed in Table 4.2.

To produce solvent/surfactant mixtures with a certain solvent concentration, the substances were weighed into small glass tubes with the analytical balance *Excellence Plus* (Mettler Toledo) with a total mass of approximately 10–20 mg. The mixtures were quickly heated into the liquid state and centrifuged with an Eppendorf *miniSpin* centrifuge, to make sure that all of the substance was at the bottom of the glass tube. To ensure a sufficient mixing of the solvent/surfactant

**Table 4.1** The basic structure of the surfactant molecules used together with the variation of headgroups, systematic names and abbreviations


R =	Systematic name	Abbreviation
	( <i>R</i> )-3-(4-(5-heptylpyrimidin-2-yl)phenoxy)propane-1,2-diol	C3
	( <i>S</i> )-5-(4-(5-heptylpyrimidin-2-yl)phenoxy)pentane-1,2-diol	C5
	( <i>R</i> )-3-(2-(4-(5-heptylpyrimidin-2-yl)phenoxy)ethoxy)propane-1,2-diol	C5O
	( <i>rac</i> )-3-(2-(4-(5-heptylpyrimidin-2-yl)phenoxy)ethoxy)propane-1,2-diol	<i>rac</i> -C5O
	( <i>S</i> )-6-(4-(5-heptylpyrimidin-2-yl)phenoxy)hexane-1,2-diol	C6
	( <i>R</i> )-3-(3-(4-(5-heptylpyrimidin-2-yl)phenoxy)propoxy)propane-1,2-diol	C6O

**Table 4.2** Source and purity of the solvents used

Solvent	Purity	Source
Water (H <sub>2</sub> O)	Double distilled	Chemical-technical service at the Institute of Physical Chemistry, University of Stuttgart
Ethylene glycol (EG)	99.8 %	Sigma-Aldrich
Polyethylene glycol 200 <sup>a</sup> (PEG 200)	Bio Ultra	Sigma-Aldrich
Polyethylene glycol 300 (PEG 300)	Bio Ultra	Sigma-Aldrich
Formamide (HCONH <sub>2</sub> )	99.5 %	Sigma-Aldrich
<i>N</i> -Methylformamide (NMF)	99.0 %	Sigma-Aldrich
Dimethylformamide (DMF)	99.8 %	Sigma-Aldrich

<sup>a</sup>Polyethylene glycol (PEG) is an oligomer or polymer with varying numbers of ethylene glycol units. The given number indicates its average molecular weight and thus is a measure for the degree of polymerization

system, the samples were kept in a thermos-shaker (*PST-60 HL plus*) at 40 °C for at least 24 h. Even though great care was taken in avoiding solvent evaporation, a certain loss of solvent has to be taken into account due to the preparation process. Nonetheless, this loss should be similar in every sample, causing only a slight absolute but not a relative error.

The sample preparation techniques required for individual measurement methods are described in the particular subsection of this method.

## 4.2 Differential Scanning Calorimetry

Differential scanning calorimetry (DSC) is a method to determine phase transition temperatures and enthalpies [3]. In this thesis a power compensation DSC of the Perkin Elmer Corporation (*DSC 8000*) was used.

For measurements 2–5 mg of the sample were weighed into small aluminum pans. In case of lyotropic liquid crystals, pans with a wall thickness of 0.25  $\mu\text{m}$  were used, instead of the conventionally used pans with a wall thickness of 0.1  $\mu\text{m}$ . This ensured that the pans do not blow up in the unfavorable event of an increasing pressure due to solvent evaporation. The sealed pan as well as a second empty pan which served as reference, were then placed into two separate microfurnaces. The furnaces were heated with a constant heat rate while the temperatures of sample and reference were measured with two independent thermo-sensors. If a phase transition occurs in the sample, a temperature difference arises between sample and reference due to the transformation enthalpy. This temperature difference was compensated by an increased heating power in the colder sample chamber. The difference in heating power was recorded as measurement signal versus time. As time and temperature are related to each other via the heat rate, the resulting thermogram was depicted as heat flow versus temperature.

If a first order phase transition takes place in the sample, a peak can be observed in the thermogram. The integrated area of the peak corresponds to the transition enthalpy and its onset to the phase transition temperature. In case of a second order phase transition, only a step-like discontinuity or  $\lambda$ -shaped singularity occurs.

The measurements in this thesis were performed by Gabriele Bräuning. A heating rate of 5 K  $\text{min}^{-1}$  was applied for every sample.

## 4.3 Polarizing Optical Microscopy

Polarizing optical microscopy is one of the most powerful tools for the characterization of liquid crystals. With this method phase transition temperatures as well as phase types can be determined [4, 5].

The property utilized for this method is the birefringence  $\Delta n$  of optical anisotropic materials. In these materials, which include almost all liquid crystals, the



refractive index  $n$  depends on the propagation direction of the light. This process can be visualized descriptively in the following manner: If a beam of light hits a birefringent material, it is split into two rays with different velocity inducing a phase shift. Furthermore, the direction of polarization of those two rays is perpendicular to each other. In general, after leaving the material those two beams interfere with each other to become elliptical polarized light. In uniaxial phases the ray in which the electrical polarization is parallel to the director is denoted by the refractive index  $n_{\parallel}$  and is called the extraordinary beam. The second ray, for which the refractive index  $n_{\perp}$  is important, is called the ordinary beam. The birefringence can then be written as  $\Delta n = n_{\parallel} - n_{\perp}$ . A graphic description of the birefringence can be given by the so called indicatrix, an ellipsoid in which the semiaxes match the refractive indices  $n_{\parallel}$  and  $n_{\perp}$ . Depending on the direction of the highest polarizability, this indicatrix can either be oblate, which is also called optically negative, or prolate, which is then called optically positive. The distance from the center of the indicatrix to its surface corresponds to the refractive index in this direction of the polarization.

A sketch of a typical polarizing optical microscope is given in Fig. 4.1. White light from a lamp is led through a polarizer to give linearly polarized light. The linearly polarized light is focused on the sample which is placed in a hot stage. Then the light is collected by an objective and passes a second polarizer, the so-called analyzer. The analyzer is turned by  $90^{\circ}$  with respect to the polarizer. If the sample is

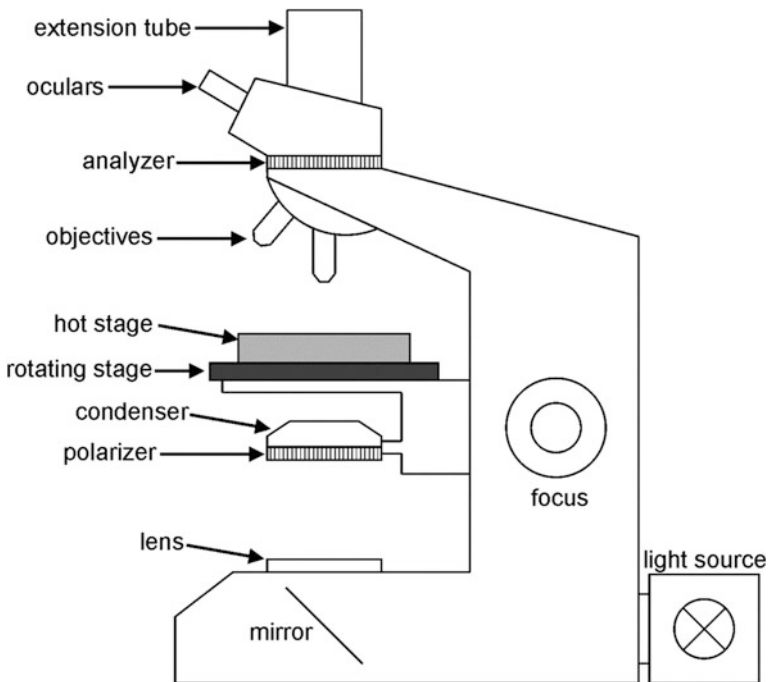


**Fig. 4.1** Polarizing optical microscopy set-up with labeling of the most important components

optically anisotropic in the plane perpendicular to the light path, it converts the linearly polarized light into elliptically polarized light and the observed picture appears bright. If the material between the crossed polarizers is isotropic and thus not birefringent, the picture seen through the oculars appears black. In case of liquid crystals, characteristic textures can be observed, which depend on the local orientation of the director and especially on characteristic defects. Hence, the investigation of liquid crystals with polarized optical microscopy gives important indications for the determination of their mesophases as well as their corresponding phase transition temperatures.

If not denoted otherwise, the measurements presented in this thesis were carried out on an Olympus *BH2* microscope. Pictures of the textures were taken with a Nikon *Coolpix 990* digital camera, which was placed on the extension tube. Series of pictures were made with a software-controlled ScopeTek *DCM500* digital camera. For temperature control a Linkam *LTS350* hot stage with an accuracy of 0.1 K was used, which allows cooling with liquid nitrogen as well as electric heating.

Samples for polarizing optical microscopy were usually prepared between untreated glass plates, which typically leads to a perpendicular or so-called homeotropic alignment of the surfactant molecules' long axes with respect to the glass. For this, a glass slide was cut into two rectangular pieces, one of them being slightly bigger than the other one. The prepared mixture was put between the plates, which were then pressed together by a specially designed compression block which is depicted in Fig. 4.2. The purpose of this block was to achieve samples as thin as possible so that the characteristic textures could be observed. If the sample was not fluid at room temperature the compression block was heated up quickly until the substance became fluid. While being compressed, drops of the UV-curable adhesive *NOA 71* (Norland) were placed at the four corners of the cut glass plates. By capillary forces, the adhesive was sucked in between the two glass plates and thereby encased the substance. For curing of the adhesive, the sample was firstly irradiated with UV light for 5 min and then kept at 50 °C for at least 12 h. Thus, the sample was sealed off from the atmosphere which inhibits solvent evaporation even at elevated temperatures. If a planar alignment of the molecules was needed, a liquid crystal measuring cell either coated with nylon or with polyimide (AWAT,

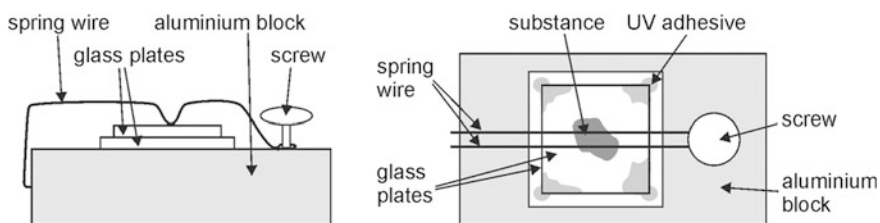


**Fig. 4.2** Side and top view of the compression block designed to prepare thin samples. The glass plates are pressed against each other with a spring wire. The compression strength can be adjusted with a screw

Poland) was broken open and then the sample was prepared in the same manner between these coated glass plates.

So-called contact preparations were made for preliminary investigations and for measurements of schematic phase diagrams. For this the neat substance was brought between two cut glass slides and surrounded with UV adhesive from three sides. Then the solvent was added from the open side and the sample was sealed and cured as described above. With this method a long-lasting solvent gradient can be achieved in the contact region of the sample, which allows the observation of all phases formed by the sample at different concentrations and temperatures.

#### 4.4 Measurement of the Director Tilt Angle

For optical measurements of the director tilt angle in lyotropic SmC and lyotropic SmC\* analog phases, very thin samples being well aligned in a planar geometry were needed. As the method usually applied for thermotropic liquid crystals to obtain such samples requires heating over a longer period of time—thus leading to the evaporation of the solvent—and the method described in Sect. 4.3 results in poorly aligned samples, a new method had to be developed. For this method, liquid crystal measuring cells with a thickness of  $1.6\ \mu\text{m}$  and a single-side rubbed nylon coating (AWAT, Poland) were used, as the best alignment could be achieved with this cell type. To avoid lengthy heating of the sample to the isotropic state, underpressure was used to quickly suck the sample into the cell. Therefore, in a first step, the cell was enclosed with UV adhesive (NOA71, Norland) until there were only two small openings left. Then, in a second step, the cell was attached to a syringe via two heat shrinkable tubings and a rubber hose. A sketch of this is depicted in Fig. 4.3. The purpose of the heat shrinkable tubing was to make an airtight connection between the syringe and the cell, while the intermediate rubber hose made sure that air can be exchanged from the cell to the syringe. The cell was then heated to approximately  $100\ ^\circ\text{C}$  with a Kofler bench of type WME. In this state, the sample was placed at the remaining opening of the hot cell and turned

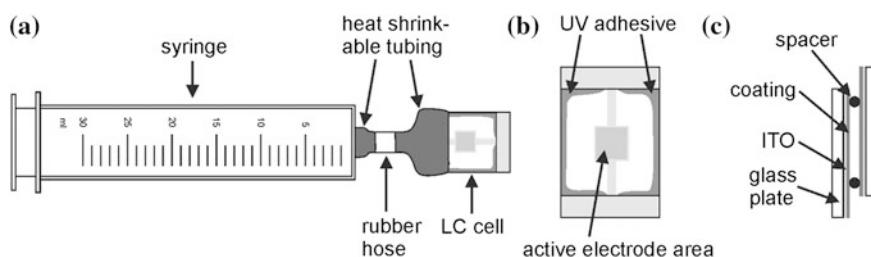


**Fig. 4.3** Suction method applied for the filling of liquid crystal measuring cells. **a** Syringe attached to the cell via heat shrinkable tubings, **b** top view of the cell showing the enclosure with UV adhesive, and **c** side view of the cell

isotropic immediately. As fast as possible the sample was sucked into the cell with the syringe. Afterwards the heat shrinkable tubing was removed and the two openings in the cell were closed with UV adhesive. With this method liquid crystal measuring cells can be filled with lyotropic liquid crystals at a minimum loss of solvent.

The measurement of the director tilt was then carried out following a standard procedure (e.g. [6]). For this, the cell was placed in the Instec hot stage *TS62* of the Leica polarizing optical microscope *DMP*, heated up into the isotropic state and then cooled down rapidly into the lamellar  $L_\alpha$  phase, to obtain a planarly aligned and oriented sample. At the phase transition towards the lyotropic  $SmC^*$  analog phase, two kinds of domains with opposite directions of the director tilt angle appeared. Using the rotating stage of the polarizing optical microscope, one of those domains was brought into extinction and the corresponding angle inscribed on the rotating stage was noted. Then the sample was rotated again until the extinction of domains with opposite tilt direction was reached. The corresponding angle was noted again. Half of the difference between those two angles matches the director tilt angle of the lyotropic  $SmC^*$  analog phase. Statistical measurement errors were reduced by averaging over four repeated measurements.

## 4.5 Measurement of the Helical Pitch

The helical pitch of the  $SmC^*$  phase and its lyotropic analog can be measured by several methods. In this thesis two of them were used to double-check the obtained results. The first applied technique is the so-called ‘direct’ method [7], which requires an orientation of the layer normal  $\mathbf{k}$  normal to the direction of observation (‘planar alignment’). The second one is the Cano method [7, 8] in which the layer normal  $\mathbf{k}$  has to be parallel to this direction (‘homeotropic’).

### 4.5.1 The ‘Direct’ Method

With the so-called ‘direct’ method, pitch lines can be observed directly by using polarizing optical microscopy. A  $SmC^*$  or  $SmC^*$  analog sample of sufficient thickness in which the helix axis is aligned parallel to the glass plates shows a periodic pattern of dark and light stripes due to the helical precession of the local director orientation (*cf.* Fig. 4.5a). But, the primary effect of the modulation of the local birefringence is superimposed by a secondary effect which is due to the appearance of disclination lines [9–11]. These so-called unwinding lines mediate between the helical structure in the center of the sample and the planar alignment close to the upper and lower glass plate. An exemplary sketch of this for antiparallel and parallel anchoring conditions is shown in Fig. 4.4. The distance between two unwinding lines corresponds directly to the length of the pitch  $p$ . However,

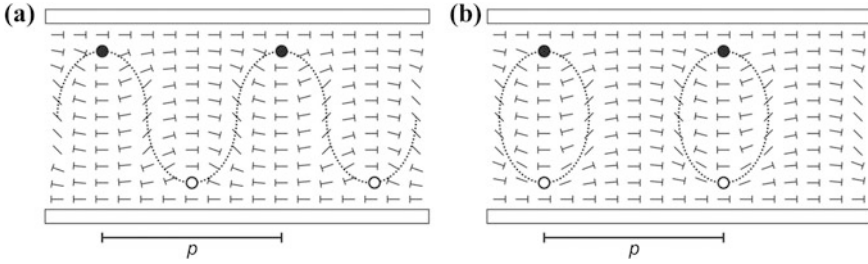


**Fig. 4.4** Unwinding lines in a SmC\* sample with **a** antiparallel and **b** parallel planar anchoring conditions on the upper and lower substrate. The local director of the SmC\* phase is represented by a nail. The symbols ● and ○ correspond to cross sections of  $+2\pi$  and  $-2\pi$  disclinations (redrawn after [11])

unwinding lines at the top and the bottom part of the sample may be shifted by  $p/2$  if the anchoring conditions are antiparallel as depicted in Fig. 4.4a. Thus, the observed periodic pattern of dark and light stripes may correspond to  $p/2$  instead of  $p$ . To check if this is the case, the sample has to be brought slightly out of focus. If every second stripe becomes sharper and every other becomes more diffuse, the distance between two lines is equal to  $p/2$  (Fig. 4.4a), whereas if every stripe behaves similarly, the distance corresponds to  $p$  (Fig. 4.4b). If the sample is too thin, the helical structure is either partially unwound or completely suppressed ('surface-stabilized', cf. [12]). A sufficient thickness to avoid unwinding seems to be about  $200\ \mu\text{m}$  [13] or at least five times the value of the pitch [7].

Samples were prepared as described in Sect. 4.3 with polyimide coated cells (AWAT, Poland). For temperature-dependent measurements cells with a gap of  $30\ \mu\text{m}$  were used, which is already thicker than five times the length of the pitch. Unfortunately, unwinding still appeared in those cells at lower temperatures. Thus, for concentration-dependent measurements samples with a cell gap of  $250\ \mu\text{m}$  were prepared using *Kapton* film (DuPont) as spacer. After the curing process the cells were placed in a magnetic field of about 1 T and cooled with a rate of  $0.05\ \text{K min}^{-1}$  from the isotropic state to the lamellar  $L_\alpha$  phase. This procedure led to an improved alignment in addition to the alignment induced by the rubbed coating of the cells and allowed the observation of the helical pitch lines. Texture images were taken in a cooling run after the sample was equilibrated for 10 min at each selected temperature. These images were analyzed with the program *ImageJ* by plotting the intensity profile perpendicular to the observed stripe texture, as shown in Fig. 4.5. The distance between several maxima of the profile was measured and converted into the value of the pitch with the aid of a calibration lattice. To minimize measurement errors this procedure was repeated four times at different positions in the sample. Finally, the obtained values were averaged.

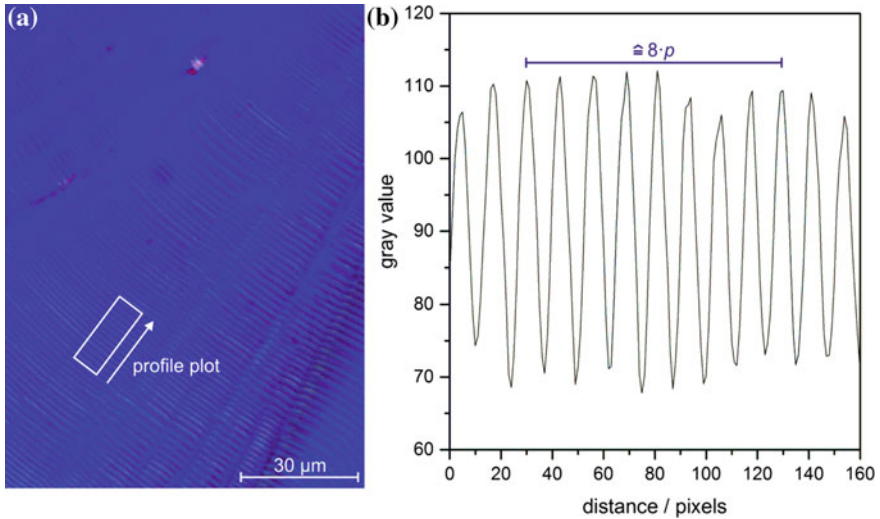


**Fig. 4.5** **a** Stripe texture of the SmC\* phase formed by the thermotropic liquid crystal 4-(2'-methylbutyl)-phenyl-4'-n-octyl-biphenyl-4-carboxylate (CE8). By plotting the intensity profile in the highlighted area with the program *ImageJ* the graph shown in **b** is obtained. From this plot the value of the pitch can be deduced if the relation between the distance in pixels and the distance in micrometers is known

### 4.5.2 The Cano Method

Usually the Cano method [8] is used for chiral nematic liquid crystals. It can also be applied to SmC\* phases, but then the demands on the orientation of the liquid crystal are more extensive as a nearly perfect orientation of the layer normal  $\mathbf{k}$  as well as of the  $\mathbf{c}$ -director are required. The presented method utilizes the different thicknesses which occur in a sample if a lens is placed on top of it. A sketch of this is shown in Fig. 4.6a. Due to the anchoring conditions, only helical structures with integer multiples  $N$  of the pitch  $p$  are allowed and regions with different values of  $N$  are separated by disclination lines [14]. Thus, a picture similar to the one shown in Fig. 4.6b occurs [15]. If the radius of curvature  $R_c$  of the lens is known, the value of the pitch  $p$  can be calculated according to [9]

$$x_N^2 = 2NR_c p. \quad (4.1)$$

To obtain good alignment of the sample, the untreated glass lens was rubbed slightly with a brush from the center to the edge of the lens. The sample was put on an microscope slide in an especially designed housing, which should avoid evaporation of the solvent. A picture of this housing is shown in Fig. 4.7. The lens was placed on top of the sample and several drops of solvent were set around it with some distance. The additional solvent should cause a solvent saturated vapor in the

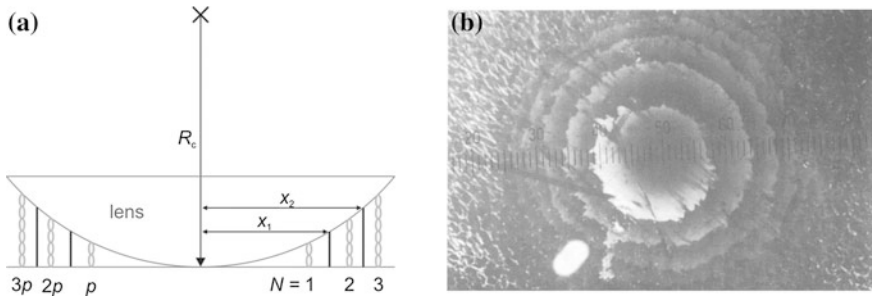


**Fig. 4.6** **a** Sketch of the Cano preparation showing the disclination lines as *black vertical lines* separating integer values  $N$  of the pitch  $p$ , the latter is depicted as *gray double helix*. **b** Exemplary picture of a Cano preparation of the lyotropic cholesteric phase formed by cellulose tricarbaniolate and diethylene glycol butyl ether (adapted from [15] with permission of the author)

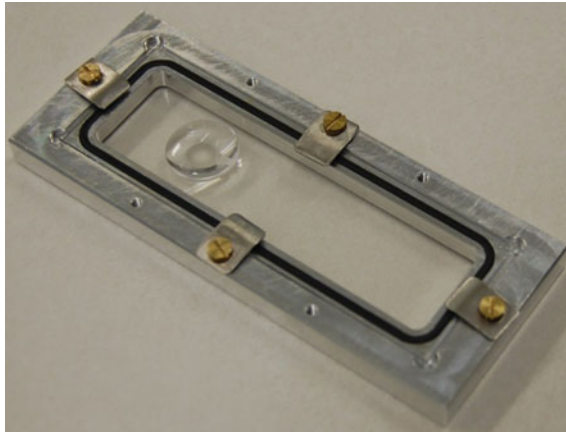


**Fig. 4.7** As the orientation process of the sample takes several days, the Cano preparation was enclosed in the pictured housing which avoided evaporation of the solvent

housing, which should again minimize the amount of solvent evaporating from the sample. Finally, the housing was closed with a second object carrier, which was fixed with four screws. The housing with the sample was placed in the Instec hot stage *TS62* mounted on the Leica polarizing optical microscope *DMLP*. To achieve an alignment of the layer normal  $\mathbf{k}$ , the sample was quickly heated up to the isotropic phase and cooled down slowly. After reaching the lamellar  $L_\alpha$  phase, the sample was cooled down faster to the phase transition into the lyotropic  $SmC^*$  analog phase. At this temperature, the sample was kept for at least 48 h to improve the alignment of the sample. If the sample showed the desired disclination lines, pictures were taken with the Nikon digital camera *D40* at different temperatures while cooling. For every temperature step the sample was equilibrated for 10 min to achieve a homogenous temperature in the sample. The radii  $x_N$  were determined graphically from the pictures with the program *CorelDraw X4*. The helical pitch  $p$  was then calculated by applying Eq. 4.1.



## 4.6 Electric and Electro-Optical Measurements

To investigate the influence of an electric field on the SmC\* phase or its lyotropic analog, the liquid crystal has to be filled into very thin liquid crystal measuring cells (*cf.* Fig. 4.3) with a thickness of 3  $\mu\text{m}$  or less which enables surface stabilization of the samples. These surface-stabilized polar liquid crystals can then be switched between two ferroelectric states by applying an electric voltage [12] (*cf.* Fig. 1.4). Such samples of the lyotropic SmC\* analog phase were either produced with the compression block or with the suction method (*cf.* Sects. 4.3 and 4.4). For a precise temperature setting, the sample was placed in a Linkam *LTS350* hot stage. Via the indium tin oxide (ITO) layer, it was possible to apply an electric field to the liquid crystal in the region of the active electrode area  $A_{\text{El}}$ .

The electric field was generated with the function generator *TG-121B* (NF Circuit Design Block Co. LTD., Japan) and amplified with a Krohn-Hite amplifier *model 7500*. To connect the cell to the electric circuit, copper wires were soldered to the ITO layer on the overlapping ends of the cell. As the electric conductivity of the solvent used in the lyotropic mixtures is quite high, dielectric break downs of the measuring cells occurred easily. Therefore, the measurements were performed as fast as possible with as little applied voltage as absolutely necessary.

### 4.6.1 Measurement of the Spontaneous Electric Polarization

The spontaneous electric polarization  $P_{\text{S}}$  of a thermotropic ferroelectric liquid crystal is usually measured with the so-called triangular wave method [16]. For this method, a triangular voltage  $U$  is applied to the liquid crystal and the so induced current in the liquid crystal is measured. This current can be divided into several contributions. If measuring a thermotropic SmC\* liquid crystal, the main contributors to the total current  $I_{\text{el}}$  are the ohmic current, caused by the resistance  $R_{\text{el}}$  of the liquid crystal, the capacitive current, due to the capacity  $C$  of the cell, and the polarization reversal current, which originates from the spontaneous electric polarization  $P_{\text{S}}$  of the polar liquid crystal.

In Fig. 4.8 an exemplary plot of the current response is given together with the applied electric field  $E$ , as commonly observed for thermotropic SmC\* phases. The areas marked in gray correspond to the contribution of the spontaneous electric polarization  $P_{\text{S}}$ . By integrating these gray areas  $A_1$  and  $A_2$ , the value of  $P_{\text{S}}$  can be calculated according to

$$P_{\text{S}} = \frac{|A_1| + |A_2|}{4A_{\text{El}}}, \quad (4.2)$$

with the active electrode area  $A_{\text{El}}$ .



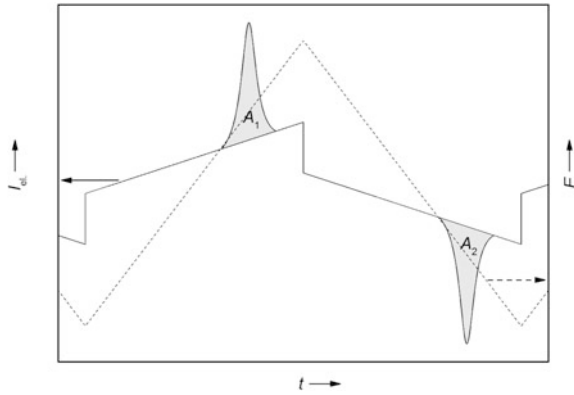


**Fig. 4.8** Applied electric field  $E$  (dashed line) and measured current response  $I_{e1}$  (solid line), as expected for a thermotropic SmC\* phase. The integrated peak areas  $A_1$  and  $A_2$  each represent twice the spontaneous polarization  $P_S$

For measurements a triangular voltage  $U$  was applied to the liquid crystal measuring cell as described above. The so induced current response was recorded with a Clevoscope oscilloscope *CS320A* and its associated software by using a load resistance  $R_L$  of  $50 \Omega$ , which was negligible compared to the resistance of the cell. Furthermore, the measured signal was averaged 16 times and a low pass filter was employed to enhance the signal's quality.

#### 4.6.2 Measurement of the Switching Time

As the brightness of the texture depends on the orientation of the director  $\mathbf{n}$  with respect to the crossed polarizers, a change from dark to bright can be observed if the SmC\* phase or its lyotropic analog are switched from one surface-stabilized state to the other by reversing the direction of the applied electric field (*cf.* Fig. 1.4). This effect can be used to determine the switching time of the ferroelectric liquid crystal. For measurements of the switching time, a rectangular voltage was applied to the liquid crystal measurement cell as described at the beginning of this chapter. Additionally, the hot stage was mounted on an Olympus *BH2* polarizing optical microscope. The change in intensity was recorded with a Burle photomultiplier *IP28* which was mounted on the extension tube of the microscope in dependence of the applied electric field  $E$ .

In Fig. 4.9 a hypothetical measurement of the relative intensity  $I_{rel.}$  is shown in dependence of the time  $t$ . The switching time  $\tau$  is measured in the range between 10 and 90 % of the maximum signal and is thus denoted as  $\tau_{10-90}$ . The switching time  $\tau_{10-90}$  is linked to the spontaneous electric polarization  $P_S$  and the rotational viscosity  $\gamma_\varphi$  via the Equation [17, 18]

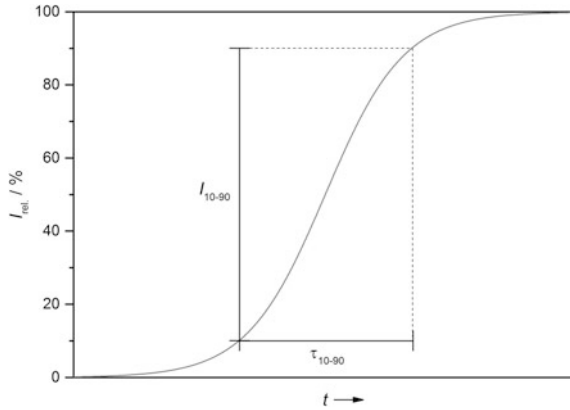


**Fig. 4.9** Theoretical measurement of the switching time  $\tau_{10-90}$ , in which the change in intensity  $I_{rel.}$  is plotted versus the time  $t$

$$\gamma_{\varphi} = \frac{1}{1.8} \tau_{10-90} P_S E. \quad (4.3)$$

Unfortunately, the only method to gain the rotational viscosity is to measure the switching times. However, in literature the values of the diverse types of viscosity often only differ marginally and mainly depend on the temperature. Thus, it is possible to make a rough estimation of the spontaneous electric polarization  $P_S$  by inserting the viscosity of a similar system.

## 4.7 X-Ray Diffraction

### 4.7.1 Basic Concepts of X-Ray Diffraction

X-ray diffraction is one of the most powerful tools for the investigation of correlated structures in the length scale from 0.1 nm up to approximately 100 nm. Already in 1923 de Broglie and Friedel showed that scattering experiments with X-rays can also be applied to liquid crystals to identify their structure [19].

In a scattering experiment [20, 21], a monochromatic X-ray beam with the wave vector  $\mathbf{k}_i$  hits a material and is scattered elastically on the electrodes of the atoms at the angle  $2\theta_{diff}$ . (Fig. 4.10a). As the scattering is elastic, the absolute values of the wave vector  $\mathbf{k}_i$  of the initial beam and the wave vector  $\mathbf{k}_s$  of the scattered beam are equal:

$$|\mathbf{k}_i| = |\mathbf{k}_s| = \frac{2\pi}{\lambda}. \quad (4.4)$$

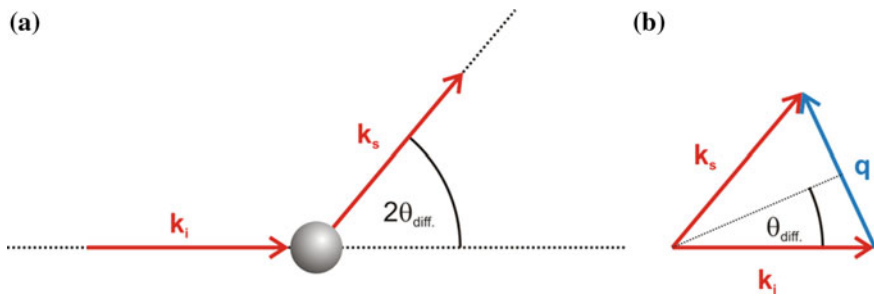


**Fig. 4.10** **a** The initial X-ray beam with the wave vector  $\mathbf{k}_i$  hits the material and is scattered at the angle  $2\theta$ . **b** The difference between the wave vector  $\mathbf{k}_i$  of the initial beam and the wave vector  $\mathbf{k}_s$  of the scattered beam is equal to the scattering vector  $\mathbf{q}$

The difference between these two vectors corresponds to the scattering vector  $\mathbf{q}$  (Fig. 4.10b)

$$\mathbf{q} = \mathbf{k}_s - \mathbf{k}_i. \quad (4.5)$$

Its absolute value is thus equal to

$$|\mathbf{q}| = \frac{4\pi}{\lambda} \sin(\theta_{\text{diff}}). \quad (4.6)$$

The intensity  $I(\mathbf{q})$  of the scattered beam depends on the electron density distribution within the probed material and is proportional to

$$I(\mathbf{q}) \propto Nf^2S(\mathbf{q}). \quad (4.7)$$

$N$  is the number of molecules,  $f$  is the molecular form factor which refers to the interference within single molecules, while the structure factor  $S(\mathbf{q})$  describes the interference on different molecules within the sample. The structure factor  $S(\mathbf{q})$  can be obtained by Fourier transformation of the pair correlation function  $g(\mathbf{r})$  according to

$$S(\mathbf{q}) = 1 + \int_{V_s} g(\mathbf{r}) \exp(-i\mathbf{q}\mathbf{r}) d^3\mathbf{r}. \quad (4.8)$$

The pair correlation function  $g(\mathbf{r})$  specifies how often the intermolecular distance  $\mathbf{r} = \mathbf{r}_j - \mathbf{r}_k$  occurs in the scattering volume  $V_s$  in time average. Thus, the pair correlation function  $g(\mathbf{r})$  strongly depends on the degree of periodicity within the material. In Fig. 4.11 two examples of characteristic pair correlation functions  $g(\mathbf{r})$  and the resulting scattering intensities  $I(\mathbf{q})$  are shown. Due to the periodic structure, the pair correlation function  $g(\mathbf{r})$  of ideal crystalline materials (Fig. 4.11a) exhibits  $\delta$ -functions in multiple distances of a set value  $d$ , which corresponds to the periodicity distance within the material. In consequence, the Fourier transform of this

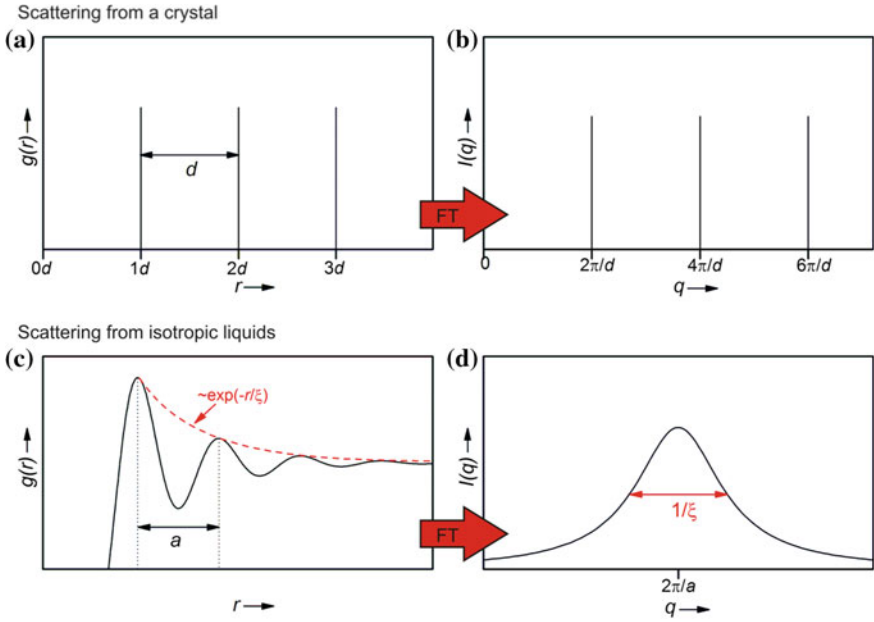


**Fig. 4.11** **a** Pair correlation function  $g(r)$  of an ideal crystal and **b** the corresponding intensity distribution  $I(q)$  obtained by Fourier transform (FT). **c** For isotropic liquids the pair correlation function  $g(r)$  is characterized by an exponentially decaying wave function which result in **d** a Lorentzian intensity distribution  $I(q)$  in the scattering image

pair correlation function  $g(\mathbf{r})$  (Fig. 4.11b), which corresponds to the scattering profile, again shows multiple orders  $n_B$  of sharp scattering peaks at

$$q = \frac{2n_B\pi}{d}. \tag{4.9}$$

The combination of the Eqs. 4.6 and 4.9 lead to the Bragg’s law [22]

$$2d \sin(\theta_{\text{diff.}}) = n_B\lambda \tag{4.10}$$

which states the condition for constructive interference and allows the calculation of the periodicity distance  $d$  out of the scattering experiment.

For isotropic liquids the pair correlation function  $g(\mathbf{r})$  takes the shape of a wave function, which decays proportionally to  $\exp(-r/\xi)$  (Fig. 4.11c). This is due to the lack of long range order within the liquid. If  $a$  is the average distance from one particle to the next, the corresponding scattering profile shows a Lorentzian function with a maximum at  $2\pi/a$  (Fig. 4.11d). The half width of this peak is reciprocally proportional to the correlation length  $\xi$  of the short range order within the liquid.

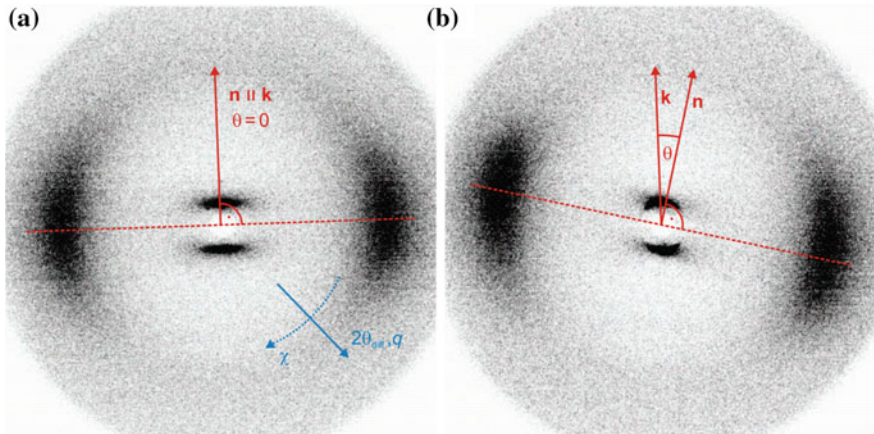


**Fig. 4.12** Two-dimensional diffraction patterns of an aligned sample of the thermotropic liquid crystalline material 5-(octyloxy)-2-(4-(octyloxy)phenyl)pyrimidine **a** at 100 °C in the SmA phase and **b** at 50 °C in the SmC phase [23]

For liquid crystals an intermediate situation between the scattering on crystals and on liquids is found. In Fig. 4.12 typical diffraction patterns of an aligned thermotropic smectic liquid crystal are shown [23]. For small scattering angles two quite sharp Bragg-like diffraction peaks can be found, which originate from scattering on the long range ordered layer structure. In the wide-angle scattering regime two rather diffuse scattering maxima appear caused by the scattering on the liquid-like distributed mesogens within the layers. In the picture shown in Fig. 4.12a the diffraction pattern of a SmA phase is displayed. Here, the small and wide-angle scattering maxima are perpendicular to each other showing that the mean molecular orientation within the smectic layers is parallel to the layer normal. In contrast, in the scattering pattern of a SmC phase (Fig. 4.12b) the scattering maxima are no longer perpendicular due to the director tilt.

For more complex liquid crystalline structures, several X-ray reflections may appear in the small-angle regime in dependence of the azimuthal angle  $\chi$  and the scattering vector  $\mathbf{q}$ . A set of integers  $hkl$  can be assigned to every reflection. This set of numbers is called the Miller indices. Every reflex originates from a bunch of lattice planes, which are described with the same set of integers  $(hkl)$ . Hence, the Miller indices describe the orientation of the individual planes with respect to the lattice. In Fig. 4.13 examples of different lattice planes and the according indexations are given. For a simplified illustration a two-dimensional lattice is used for which only the Miller indices  $h$  and  $k$  are important. A particular lattice plane intercepts the lattice vectors  $\mathbf{a}$  and  $\mathbf{b}$  at the points  $\mathbf{a}/h$  and  $\mathbf{b}/k$ . Thus, the Miller indices  $(hk)$  of a particular lattice plane are the inverse of the intercepts. For example, if a lattice plane does not intercept a lattice vector at all, i.e. the intercept is at infinity, the according Miller index is zero.

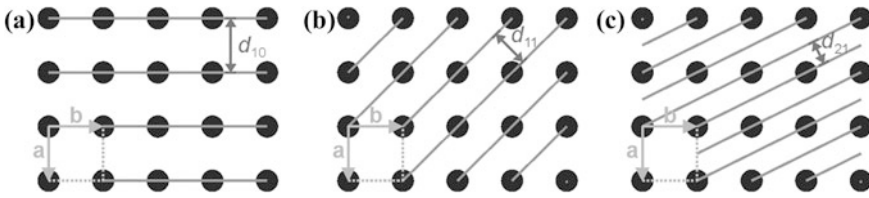


**Fig. 4.13** Examples for different lattice planes in a two-dimensional rectangular lattice spanned by the lattice vectors **a** and **b**. For figure **a** the miller indices are (10), for figure **b** (11) and for figure **c** (21)

In general, liquid crystals only possess a periodic structure in one or two dimensions. Therefore, the Miller index *l* and often also the Miller index *k* can be omitted. In case of a one-dimensional periodic structure, the periodicity distances *d* in Eqs. 4.9 and 4.10 and are directly linked to the layer spacing. Hence, this layer spacing is also denoted with *d*. For two-dimensional structures more complex correlations are needed to make a statement about the lattice constants *a* and *b*. Depending on the plane group of the liquid crystal, which is the two-dimensional analog of the space group, different equations are needed. For a hexagonal lattice the correlation

$$\frac{1}{d_{hk}^2} = \frac{4}{3} \cdot \frac{h^2 + k^2 + hk}{a^2} \tag{4.11}$$

has to be applied. The hexagonal lattice is the most symmetric two-dimensional lattice. It is found quite often in liquid crystalline systems. A further important lattice type is the rectangular lattice. The lattice constants of a phase with this symmetry can be calculated according to

$$\frac{1}{d_{hk}^2} = \frac{h^2}{a^2} + \frac{k^2}{b^2}. \tag{4.12}$$

The plane lattice with the least symmetry is the oblique one. For the calculation of its lattice vectors the variable angle  $\gamma$  of the unit cell has to be considered:

$$\frac{1}{d_{hk}^2} = \frac{h^2}{a^2 \sin^2 \gamma} + \frac{k^2}{b^2 \sin^2 \gamma} - \frac{2hk \cos \gamma}{ab \sin^2 \gamma}. \tag{4.13}$$

As can be seen from Eqs. 4.11 to 4.13, the knowledge of the Miller indices is crucial for the understanding of two-dimensional correlated structures. A simplistic method to determine the Miller indices of a given scattering pattern is to superimpose this pattern with a lattice. The lattice is applicable if reflexes only occur on points of intersection. If this condition is fulfilled, the position of the reflex in the lattice corresponds to its Miller indices. This superimposed lattice is called the reciprocal lattice and has a deeper meaning in crystallography.

### 4.7.2 X-Ray Diffraction Experiments

For X-ray experiments, samples in Hilgenberg Mark capillaries with a diameter of 0.7 mm were used. To avoid solvent evaporation due to heating, a special method was applied to prepare the samples. At first a truncated and deflashed cannula of a syringe was poked repeatedly into the prepared mixture. By doing this, the substance was pressed into the cannula. Afterwards the substance was squeezed out of the cannula directly into the Mark capillary with a thin piece of spring steel. In case of rather fluid samples which stucked to the walls of the Mark capillary, the capillary was additionally centrifuged with the Eppendorf *miniSpin* centrifuge. Thereby all of the substance was brought to the bottom of the capillary. The upper part of the Mark capillary was truncated and sealed by melting it with a lighter. In this process, attention was given to minimize the free volume in the capillary to confine the solvent within the mixture.

Small-angle X-ray scattering (SAXS) experiments were performed with the Anton Paar small-angle scattering system *SAXSess*. The Cu-K $_{\alpha}$  X-ray radiation ( $\lambda = 0.15418$  nm) used was generated by the *ISO-DEBYEFLEX 3003* X-ray generator (GE Inspection Technologies GmbH), which was operated with a voltage of 40 kV and a tube current of 50 mA. The radiation was focused and monochromatized by a bent-multilayer mirror. To achieve a high resolution of the scattering signal, the X-ray beam was line collimated by a collimation block. The X-ray beam then hit the sample, which was placed in the temperature controllable sample holder *TCS 120*. This sample holder can produce temperatures between -30 and 120 °C by using a Peltier element. The housing of the *SAXSess* was evacuated to avoid unwanted scattering. After passing the sample, the scattered as well as the primary beam hit the CCD detector, which has a pixel size of  $24 \times 24 \mu\text{m}^2$ . The primary beam is attenuated by a semipermeable beam stop, which allows an intern calibration. Temperature-dependent measurements were managed with the software *SAXSquant 3.5*. Finally, the one-dimensional scattering profiles obtained were analyzed with the program *OriginPro 9.0G*, which offers a semi-automated peak fitting.

Two-dimensional X-ray patterns in the small (SAXS) as well as in the wide angle regime (WAXS), were measured with a Bruker AXS *NanoStar* system. The X-ray radiation was generated by a Siemens *Kristalloflex 770* X-ray generator. The radiation was monochromatized and focused with two Göbel mirrors. The resulting Cu-K $_{\alpha}$  X-ray radiation with a wavelength of  $\lambda = 0.15418$  nm was then led into the evacuated sample chamber after passing two pinholes. The sample was placed in a specially designed sample holder. The temperature of the sample was controlled with a Eurotherm *2216e* regulator, which was integrated in an mri Physikalische Geräte GmbH *TCPU H* control unit. For cooling, a Huber *Unichiller* was connected, which was operated with a water/glycerol mixture. Thereby, a temperature range of 10–180 °C was accessible. For an improved sample alignment, two permanent magnets were attached to the sample holder, which generated a magnetic field of approximately 1 T. Furthermore, the sample holder was moveable in all

three directions in space. Therefore, it was possible to find a well aligned position in the sample to probe. With the help of extension tubes, the sample to detector distance was variable in a range between 11 and 105 cm. The exact sample to detector distance was determined by a calibration measurement with silver behenate. The scattered X-ray radiation was detected with a Bruker AXS *Hi Star* area detector with a resolution of  $1024 \times 1024$  pixel. The primary data analysis was carried out with the attached software *SAXS 4.1.35* (Bruker AXS) or *datasqueeze 3.0* (Paul A. Heiney). For further data processing *OriginPro 9.0G* was used.

## References

1. J.R. Bruckner, D. Krueerke, J.H. Porada, S. Jagiella, D. Blunk, F. Giesselmann, J. Mater. Chem. **22**, 18198–18203 (2012)
2. J.R. Bruckner, J.H. Porada, C.F. Dietrich, I. Dierking, F. Giesselmann, *Angew. Chem. Int. Ed.* **52**, 8934–8937 (2013)
3. G. Höhne, W. Hemminger, H.-J. Flammersheim, *Differential Scanning Calorimetry—An Introduction for Practitioners* (Springer, Heidelberg, 1996)
4. D. Demus, L. Richter, *Textures of Liquid Crystals*, 2nd edn. (VEB Deutscher Verlag für Grundstoffindustrie, Leipzig, 1978)
5. I. Dierking, *Textures of Liquid Crystals* (WILEY-VCH Verlag GmbH & Co KGaA, Weinheim, 2003)
6. D. Nonnenmacher, *Struktur-Eigenschaftsbeziehungen in smektischen Flüssigkristallen vom de Vries-Typ*, doctoral thesis, University of Stuttgart, 2014
7. M. Brunet, *Ferroelectrics* **84**, 25–52 (1988)
8. R. Cano, *Bull. Soc. Fr. Min. Crist. XC*, 333–351 (1967)
9. M. Brunet, C. Williams, *Ann. Phys.* **3**, 237–248 (1978)
10. M. Glogarová, L. Lejčėk, J. Pavel, V. Janovec, J. Fousek, *Mol. Cryst. Liq. Cryst.* **91**, 309–325 (1983)
11. M. Glogarová, J. Fousek, L. Lejčėk, J. Pavel, *Ferroelectrics* **58**, 161–178 (1984)
12. N.A. Clark, S.T. Lagerwall, *Appl. Phys. Lett.* **36**(11), 899–901 (1980)
13. K. Kondo, H. Takezoe, A. Fukuda, E. Kuze, *Jpn. J. Appl. Phys.* **21**(2), 224–229 (1982)
14. W. Kuczyński, *Phys. Rev. E* **81**(2), 021708(6) (2010)
15. M. Siekmeyer, *Untersuchungen zu Struktur und Phasenverhalten lyotroper Mesophasen von Cellulosetricarbanilat*, doctoral thesis, Clausthal University of Technology, 1989
16. K. Miyasato, S. Abe, H. Takezoe, A. Fukuda, E. Kuze, *Jpn. J. Appl. Phys.* **22**(10), L661–L663 (1983)
17. J.-Z. Xue, M.A. Handschy, N.A. Clark, *Ferroelectrics* **73**(1), 305–314 (1987)
18. K. Sarp, K. Flatschler, S.T. Lagerwall, *Ferroelectrics* **84**(1), 183–195 (1988)
19. M. de Broglie, E. Friedel, *C.R. Acad. Sci.* **176**, 738–740 (1923)
20. G. Strobl, *Physik kondensierter Materie* (Springer, Heidelberg, 2002)
21. F. Giesselmann, in *Structural Studies of Liquid Crystals by X-ray Diffraction*, Bandol Summer School on Liquid Crystals, 2014
22. W.L. Bragg, *Proc. Cambridge Philos. Soc.* **17**, 43–57 (1912)
23. Diffraction patterns courtesy of Sonja Dieterich



# Chapter 5

## Results and Discussion

The experimental results of the present thesis will be presented and discussed in the following chapter. The main focus will be upon the detection and characterization of the novel lyotropic SmC\* analog phase, even though a variety of other phases occurs in the investigated solvent/surfactant mixtures. Furthermore, the obtained results will be discussed in detail in the course of this chapter.

### 5.1 Preliminary Investigations

#### 5.1.1 Design Strategy

For quite some time, the lyotropic analog of the chiral SmC\* phase (lyo-SmC\* phase)<sup>1</sup> was searched for without success. This is not astonishing as even for the achiral version there are only very rare examples in literature. Thus, the first step for the detection of a lyotropic SmC\* analog phase was to devise a reasonable design strategy for the synthesis of suitable surfactant molecules. This design strategy was discussed in our group during the last years.

As a starting point for the design strategy, the most prominent examples of lyotropic SmC analog phases in literature were analyzed (*cf.* Sect. 1.3). The first example is an amphiphilic diol molecule reported by Pietschmann et al. [1]. The chemical structure of this molecule is given in Fig. 5.1a. Even though the molecule has a center of chirality, it was only investigated as racemic mixture by Pietschmann et al. The molecule is composed of three chemically different parts. The first part is a flexible aliphatic chain. The second part is an aromatic core or more precisely a phenylpyrimidine unit. Such a phenylpyrimidine core is known to be a SmC-promoting motif [2, 3] and therefore this molecule should be well suited for the formation of tilted phases. Up to this point, the mentioned structural elements are typical for thermotropic liquid crystals. Hence, to provide the solubility necessary for lyotropic liquid crystals, the last part of the molecule is a diol

---

<sup>1</sup>In order to facilitate the readability of this thesis, the lyotropic analog of the chiral SmC\* phase will be abbreviated with the term 'lyo-SmC\* phase' in the following if expedient.

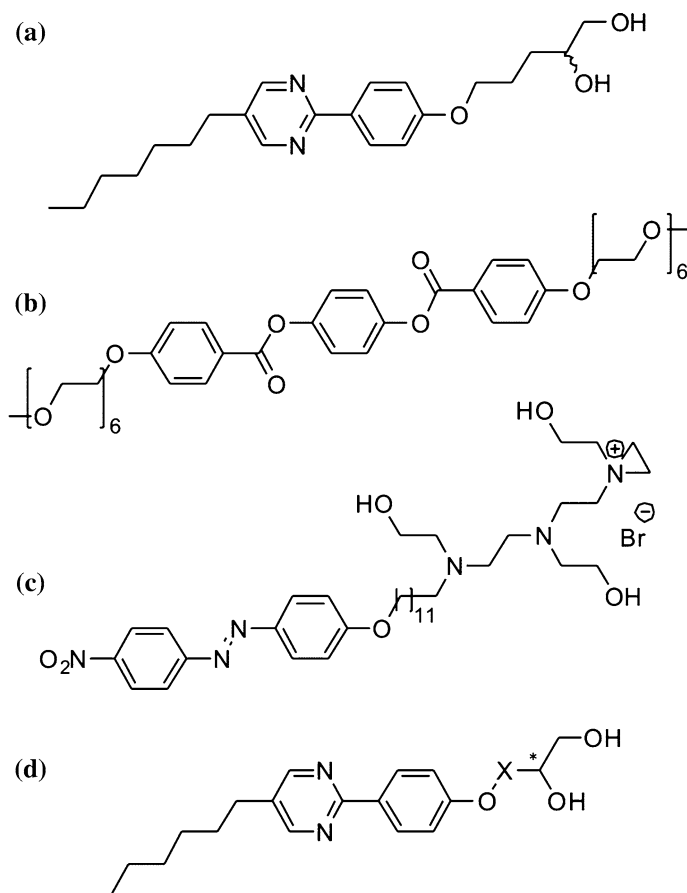


**Fig. 5.1** Molecules regarded for the design strategy: **a** diol molecule synthesized by Pietschmann et al. [1], **b** amphiphile by Schafheutle et al. [8], **c** ionic amphiphile by Ujje et al. [9] and **d** basic module of the devised surfactant molecules. *X* symbolizes varying lengths of alkyl or alkoxy chains, which link the diol head group to the ether bond attached to the aromatic core

headgroup [4, 5]. This diol group is linked to the aromatic core via an alkoxy chain. All of these three parts together make the discussed molecule an ideal candidate for the formation of a lyotropic SmC analog phase. However, in previous work [6, 7], we showed that the lyotropic SmC analog phase supposed by Pietschmann et al. is actually a two-dimensionally correlated columnar phase. Nonetheless, the structural elements of this molecule seem to be very promising for the formation of a lyotropic, fluid and tilted phase and thus were kept in mind in the further process.

The second example in literature is a rod-like amphiphile synthesized by Schafheutle et al. [8]. Its chemical structure is shown in Fig. 5.1b. In this case the authors proved the existence of a lyotropic SmC phase in mixture with water by two-dimensional X-ray diffraction of an aligned sample. Again, this molecule

possesses a quite rigid aromatic system, which seems to be a crucial element for an intra-layer tilt correlation. On both sides of the tripartite core, polyethylene glycol units are attached. These polyethylene glycol units serve as flexible side chains and at the same time as hydrophilic moiety. Furthermore, the repeated oxygen atoms enable the formation of multiple hydrogen bonds with water which was used as solvent.

A third example of a surfactant molecule which forms a lyotropic SmC analog phase in water is the ionic amphiphile reported by Ujiie et al. [9] (Fig. 5.1c). The molecule possesses a polyethylene imine unit, analog to the polyethylene glycol units of the Schafheutle molecule.

Based on these considerations, a new series of surfactant molecules (*cf.* Fig. 5.1d) was devised, which were expected to exhibit the lyotropic analog of the thermotropic SmC\* phase. The basic module of this series of molecules was the same 4-(5-heptylpyrimidin-2-yl)phenoxy moiety as used in the molecule by Pietschmann et al. Moreover, a diol unit served as hydrophilic head group. A difference was made in the linking units used between those two structural elements: several different alkyl and alkoxy chains were used (*cf.* Sect. 4.1, Table 4.1), imitating the ethylene glycol units of the molecule presented by Schafheutle et al. With this design strategy several new surfactant molecules were synthesized and investigated with respect to their lyotropic phase behavior. The synthetic work was done by Dr. Jan H. Porada.

### 5.1.2 Screening of the Diverse Surfactant/Solvent Systems

To gain a first impression of the lyotropic and thermotropic phases exhibited by the synthesized surfactant molecules, contact preparations were made. In a contact preparation a solvent gradient exists over the whole sample. All phases occurring in the phase diagram at a given temperature can thus be detected in a single sample. An exemplary texture image of this is shown in Fig. 5.2. The phase boundaries which follow the concentration gradient can clearly be seen, making it possible to derive a simple qualitative phase diagram. In contrast to a proper phase diagram, the actual concentrations are unknown. Nonetheless, this is a valid method for screening whether the Lyo-SmC\* phase exists in the investigated solvent/surfactant system or not.

In a first attempt, double distilled water was used as solvent for all surfactant molecules. The obtained schematic phase diagrams for the individual surfactant molecules will be presented in the following. Next to the schematic phase diagram measured while heating, the schematic phase diagram obtained while cooling will be shown whenever monotropic phases appear in the investigated system.

#### Variation of the surfactant molecule

Figure 5.3 shows the schematic phase diagram of C3 and water. All liquid crystalline phases occurring in this system are monotropic. The displayed phase

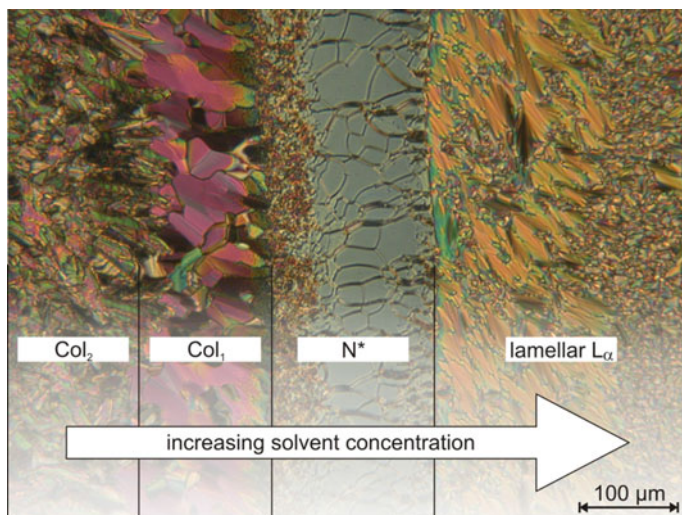


**Fig. 5.2** Texture image as seen through crossed polarizers in the contact region of the diol C50 and ethylene glycol at 59 °C. Sharp boundary lines separate the individual liquid crystalline phases, which appear due to the concentration gradient

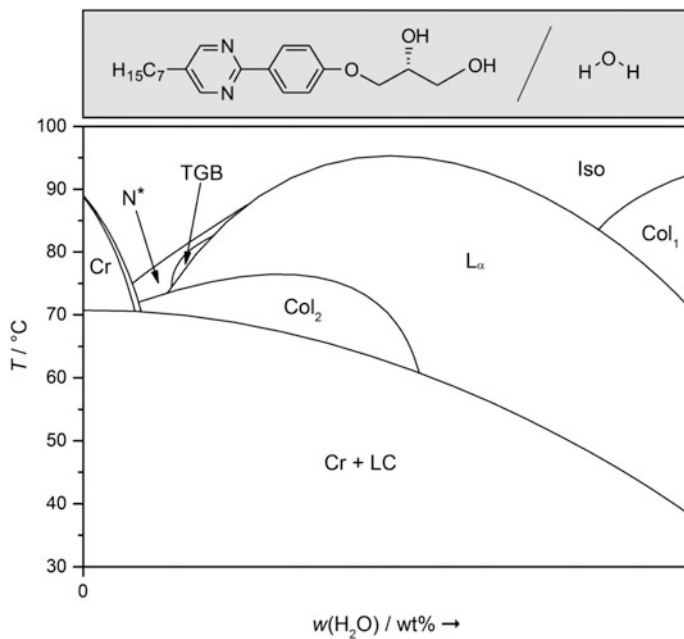


**Fig. 5.3** Schematic phase diagram based on a contact preparation of C3 and double distilled water measured on cooling

diagram was thus measured on cooling. In the neat state, no liquid crystalline phase exists, but already the addition of very small amounts of solvent leads to the appearance of a  $N^*$  phase. The dominating phase in the phase diagram is the chiral lamellar  $L_\alpha$  phase.<sup>2</sup> Between those two phases a further phase occurs which is quite unstable and thus could not be examined in detail. It exhibits a filament texture, which is known from thermotropic twist grain boundary phases. Therefore, this phase might be a lyotropic analog of the thermotropic TGBA\* phase. But as this phase is unknown in lyotropic liquid crystals so far, further experiments are necessary to identify this phase with certainty. Furthermore, two different columnar phases occur. As the symmetry of these phases is unknown, they will simply be denoted with the abbreviation Col, whereas Col<sub>1</sub> stands for the high temperature phase and Col<sub>2</sub> for the low temperature phase. It seems quite odd, that the Col<sub>1</sub> phase should appear at higher temperature than the lamellar  $L_\alpha$  phase, as the columnar phase possesses a more complex structure. However, the phase sequence was checked several times, always leading to the same result.

The schematic phase diagram of the C5/H<sub>2</sub>O system in Fig. 5.4 was already determined in work preceding this thesis [6, 7]. Hence, it is repeated here to complete the series of diol molecules and their qualitative phase diagrams. Similar to the system discussed before, the C5/H<sub>2</sub>O system forms a  $N^*$  phase and a lamellar  $L_\alpha$  phase. Furthermore, three different types of columnar phases can be found in the phase diagram. At intermediate water concentrations an oblique  $M_\alpha$  phase occurs, which is stable over a quite broad concentration and temperature range. At high water concentrations a hexagonal  $H_\alpha$  phase appears at high temperatures. By cooling down the hexagonal  $H_\alpha$  phase a rectangular R phase emerges. Details on the structure of the columnar phases can be found in Ref. [7].

In the upper part of Fig. 5.5 the schematic phase diagram of C5O and water is depicted. Again a  $N^*$  phase appears at low solvent concentrations and the dominating phase in the phase diagram is the lamellar  $L_\alpha$  phase. At high solvent concentrations a high and a low temperature columnar phase occur. At higher water concentrations a fifth phase can be found, which seems to be very promising. This phase shows quite characteristic textures as known from the thermotropic SmC\* phase, i.e. broken fan shaped texture and schlieren texture. An exemplary texture image of the homeotropically aligned contact preparation is shown in the lower part of Fig. 5.5. The left side of the image shows the crinkled texture of the low temperature Col<sub>2</sub> phase. To the right side of the picture, the texture turns into a schlieren texture as typically exhibited by homeotropically aligned thermotropic SmC\* phases. But as the designation of phases based solely on the texture are rather vague, further evidence has to be provided to prove if this phase is really the

---

<sup>2</sup>The International Union of Pure and Applied Chemistry (IUPAC) recommended in 2001 [10], that every liquid crystalline phase composed of chiral molecules should be denoted with a superscript asterisk. However, this is not customary in lyotropic liquid crystal nomenclature, except for the chiral nematic phase ( $N^*$ ). Thus, for all other conventional lyotropic liquid crystalline phases the asterisk will be omitted. Whenever the chirality of the molecules seems to be especially important, the according phase will be denoted as 'chiral'.

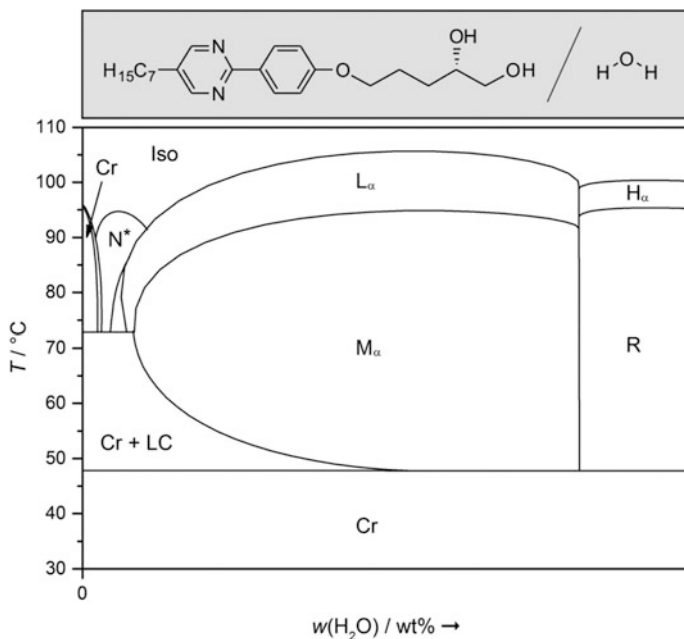


**Fig. 5.4** Qualitative phase diagram of C5 and water (redrawn after [7])

searched for lyotropic analog of the  $\text{SmC}^*$  phase. Hence, the C5O surfactant molecule as well as the C5O/ $\text{H}_2\text{O}$  system were selected for more detailed investigations, which will be discussed in the following chapters.

The surfactant molecule C6 possesses almost the same chemical structure as the molecule C5O. The only difference is that the oxygen atom in the linking unit is replaced by a carbon atom. Therefore, it is not astonishing, that the schematic phase diagram of the C6/water system in Fig. 5.6 possesses similarities to the one of the C5O/water system. In analogy to the already discussed system, the C6/water system exhibits no enantiotropic liquid crystalline phase in the neat state, but the addition of small amounts of solvent leads to the induction of several lyotropic phases. Again these phases are an  $\text{N}^*$  phase, a lamellar  $\text{L}_\alpha$  phase and two columnar phases. In contrast to the formerly presented system, no further phase can be found in the phase diagram, which might be a  $\text{SmC}^*$  analog phase. Thus, the removal of the oxygen atom does not have a very big impact on the formation of conventional lyotropic liquid crystalline phases but on the stabilization of a possible tilted phase.

The last investigated surfactant/solvent system is composed of the surfactant C6O and water. Its schematic phase diagram is shown in Fig. 5.7. As different phases appear while heating and while cooling, schematic phase diagrams for both processes were measured. The only enantiotropic stable liquid crystalline phase is the lamellar  $\text{L}_\alpha$  phase. In contrast to the other investigated systems, this phase also exists as  $\text{SmA}^*$  phase in the neat state. Most likely this is due to the elongated

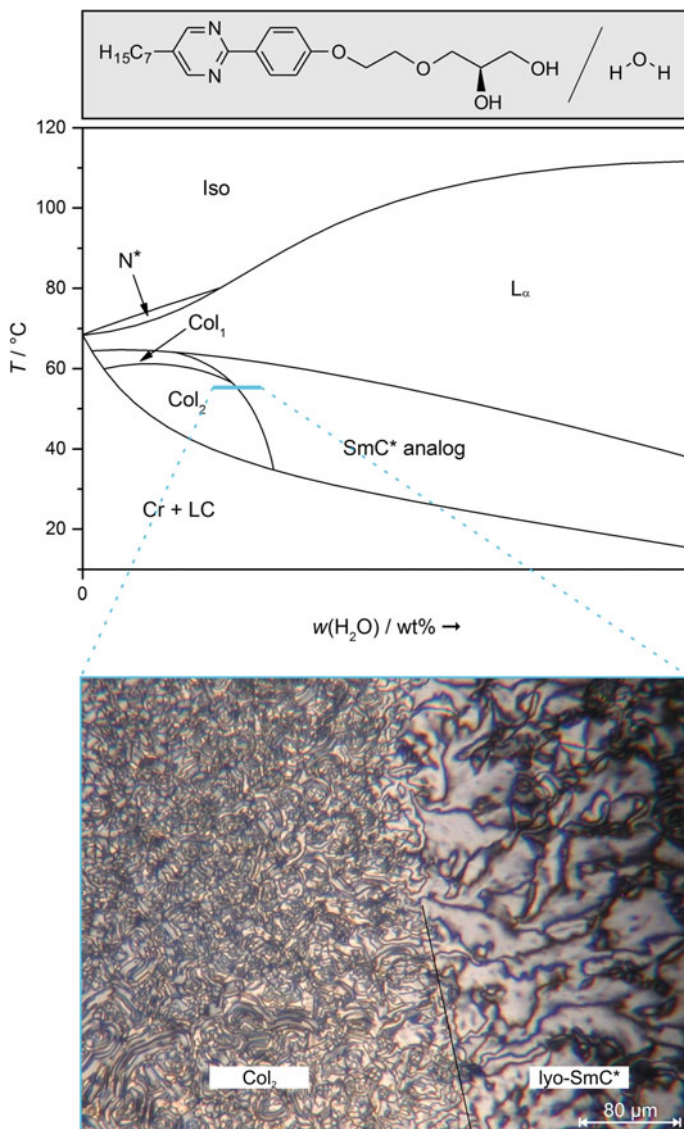


**Fig. 5.5** Schematic phase diagrams of the C50/water system (top). The blue line indicates the temperature and concentration range of the contact preparation in which the texture image (bottom) was taken

linking unit causing a higher flexibility and thus hindering crystallization. On cooling, a second liquid crystalline phase occurs at higher solvent concentrations. Based on its texture, this phase was identified as columnar. Even though the surfactant molecule C60 possesses an alkoxy chain in analogy to C50, no possible lyo-SmC\* phase was found in this system.

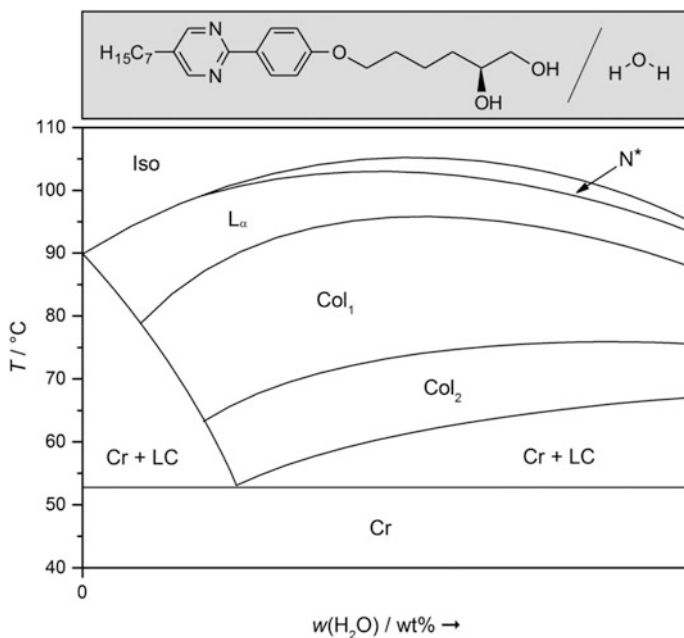


**Fig. 5.6** Qualitative phase diagram derived from the contact preparation of C6 and water

Out of the five surfactant/water systems presented only one possibly exhibits a lyotropic  $\text{SmC}^*$  analog phase. The corresponding surfactant molecule C5O holds an ethoxypropane chain as linking unit. The overall design of the molecule is very delicate. If the oxygen atom is replaced by a carbon atom as it is the case in the C6 molecule, or the ethoxy group is elongated by one carbon atom to a propoxy group as in the molecule C6O, no lyo- $\text{SmC}^*$  phase forms. Nonetheless, the devised design strategy was successful.

Up to now, only the structural demands on the surfactant were considered. But as the solvent is the second important component of the lyotropic liquid crystalline system, the nature of the solvent has to be reflected, too. Thus, to learn more about the role of the solvent, contact preparations of C5O and diverse hydrophilic solvents were screened. The schematic phase diagrams obtained will be discussed in the following section.

### Variation of the solvent

Besides water, typical solvents used in literature for lyotropic liquid crystalline systems are ethylene glycol and formamide [11, 12]. This is not surprising, as all of these solvents are polar protic solvents and thus share a couple of properties, e.g. a low molecular weight, a highly polar structure and the ability to form hydrogen bonds [13]. To gain further insight into the influence of the solvent's chemical structure on the formation of the lyo- $\text{SmC}^*$  phase, additional solvents were used.



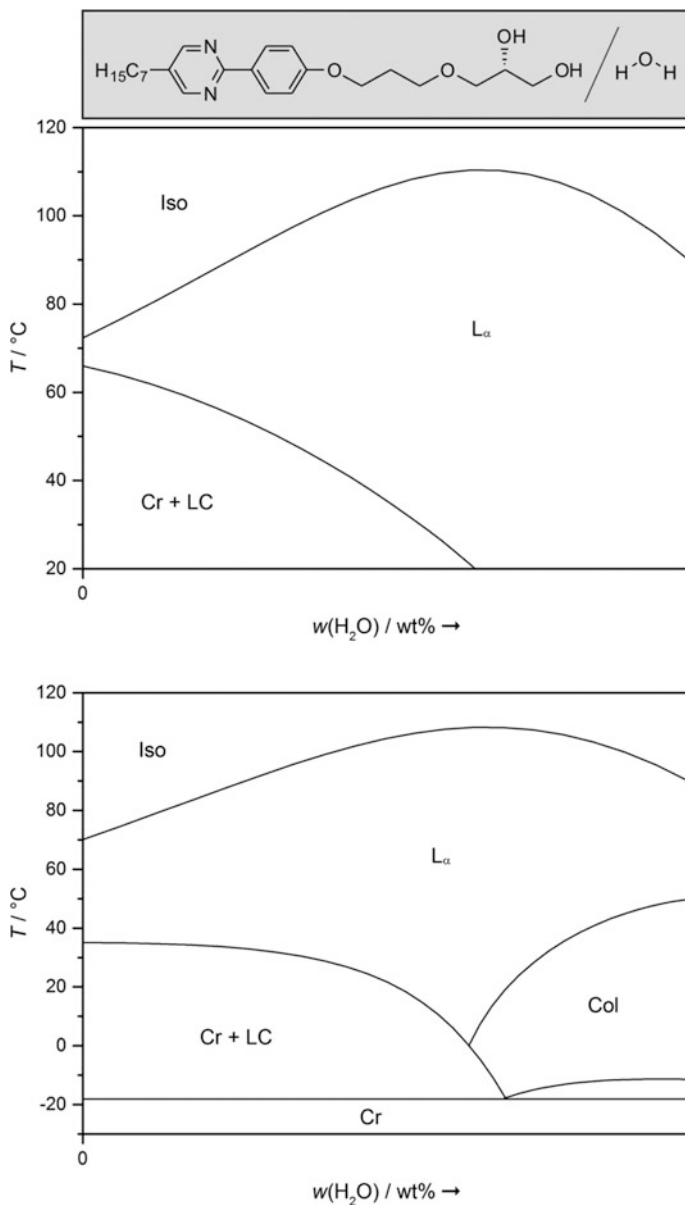


**Fig. 5.7** Schematic phase diagrams of the C6O/H<sub>2</sub>O system, measured on heating (*top*) and on cooling (*bottom*). In addition to the enantiotropic lamellar  $L_\alpha$  phase a Col phase appears on cooling at elevated water concentrations

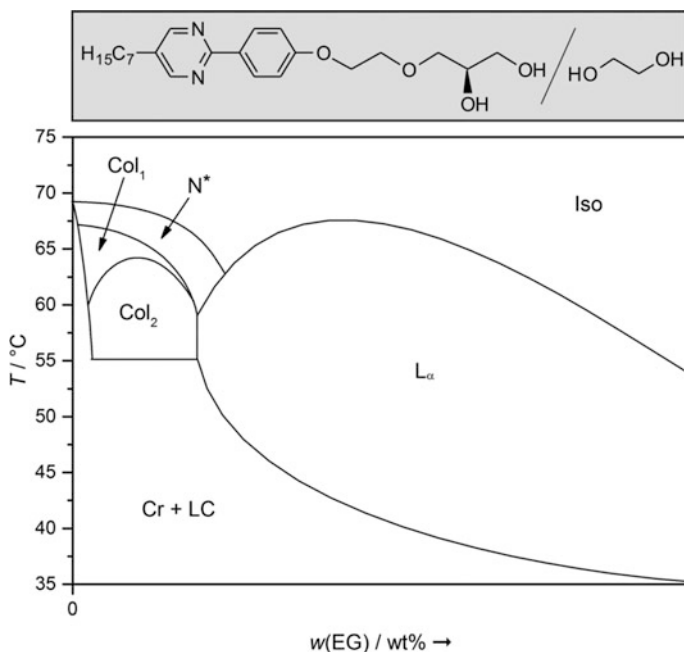
The solvents are polyethylene glycol 200, polyethylene glycol 300, *N*-methylformamide and dimethylformamide. A summary of some fundamental physical data of the solvents used is given in Table 5.1.

**Table 5.1** Fundamental physical data of the solvents used

Solvent	Molecular weight $M$ (g mol <sup>-1</sup> )	Melting point $T_{mp}$ (°C)	Boiling point $T_{bp}$ (°C)	Density (25 °C/*20 °C) $\rho$ (g cm <sup>-3</sup> )
Water	18.02 [15]	0 [15]	100 [15]	0.997 [15]
Ethylene glycol	62.07	-13	195–198	1.113
PEG 200	200.0 [16]	-38 to -36 [16]	>150 [16]	1.124* [16]
PEG 300	300.0 [16]	-15 to -10 [16]	>220 [16]	1.125* [16]
Formamide	45.04	2–3	210	1.134
NMF	59.07	-4	198–199	1.011
DMF	73.10	-61	153	0.944

If not denoted differently all data are taken from [14]

The schematic phase diagram based on the contact preparation of C50 and ethylene glycol is shown in Fig. 5.8. Similar to the schematic phase diagram with water, a N\* phase and two columnar phases appear at low solvent concentrations. The most stable phase in the phase diagram is again the lamellar L<sub>α</sub> phase. No lyo-SmC\* phase was found with ethylene glycol as solvent.

**Fig. 5.8** Schematic phase diagram derived from a contact preparation of C50 and ethylene glycol

In the contact region of C5O and PEG 200, the only enantiotropic liquid crystalline phase appearing is a  $N^*$  phase, as seen in Fig. 5.9. Upon cooling, a monotropic lamellar  $L_\alpha$  phase is formed. In contrast to the sample with monomeric ethylene glycol, the lamellar  $L_\alpha$  phase which forms with PEG 200 is only stable in a range of a few Kelvin but in a quite broad concentration range.

In Fig. 5.10 the schematic phase diagrams of the C5O/PEG 300 system are shown. Again, the only enantiotropic phase is a  $N^*$  phase. On cooling a lamellar  $L_\alpha$  phase appears, which is even less stable than in the contact preparation with PEG 200, regarding the temperature as well as the concentration range.

By replacing the monomeric ethylene glycol with the polymeric ethylene glycols PEG 200 and PEG 300, the overall stabilization of the liquid crystalline phases decreases. Only two instead of four different liquid crystalline phases appear in the phase diagrams, with the  $N^*$  phase being the sole enantiotropic mesophase. Furthermore, the concentration and temperature ranges in which these phases exist become smaller. Thus, a small molecular volume and a highly polar structure of the solvent seem to be favorable for the formation of lyotropic phases (*cf.* Table 5.2). However, no lyotropic  $SmC^*$  analog phase forms with any of these three solvents.

In a second approach, formamide and its derivatives *N*-methylformamide and dimethylformamide were investigated as solvents. The system C5O/formamide seemed to be very promising for the formation of a lyotropic analog of the  $SmC^*$  phase. As can be seen in Fig. 5.11, five different enantiotropic liquid crystalline phases are formed with formamide as solvent. The dominating phase in the phase diagram is the lamellar  $L_\alpha$  phase, as is the case with most solvents. At lower solvent concentrations a  $N^*$  phase appears, as well as two different columnar phases  $Col_1$  and  $Col_2$ . At higher solvent concentrations a further phase forms below the lamellar  $L_\alpha$  phase. At the bottom of Fig. 5.11 a texture image in the contact region between this mesophase and the lamellar  $L_\alpha$  phase is shown. While the lamellar  $L_\alpha$  phase exhibits a broken fan texture and insular homeotropic areas, the other mesophase shows a broken fan texture as well as a schlieren texture. Based on this observation, the regarded phase might be a lyotropic  $SmC^*$  analog phase. For clarification, further investigations were performed on this system and will be presented in the subsequent chapters.

In *N*-methylformamide one hydrogen atom of the amide group is replaced by a methyl group. This still allows hydrogen bonding but with lower density than in formamide. The contact region of this solvent and the surfactant molecule C5O shows two enantiotropic liquid crystalline phases (Fig. 5.12). As in the C5O/formamide system, these two phases are the  $N^*$  phase and the lamellar  $L_\alpha$  phase. On cooling, two monotropic columnar phases appear at low solvent concentrations. Furthermore, between the  $N^*$  phase and the lamellar  $L_\alpha$  phase, a phase occurs which exhibits a texture resembling the texture of the thermotropic twist grain boundary phase. As already mentioned at the description of the C3/water system, there are no reports in literature about lyotropic TGB phases. Due to this, the C5O/*N*-methylformamide system is interesting even though no lyotropic analog of the  $SmC^*$  phase was found. Thus, the system as well as its lyotropic liquid crystalline phases were examined more closely and will be discussed in Sect. 5.2.2.

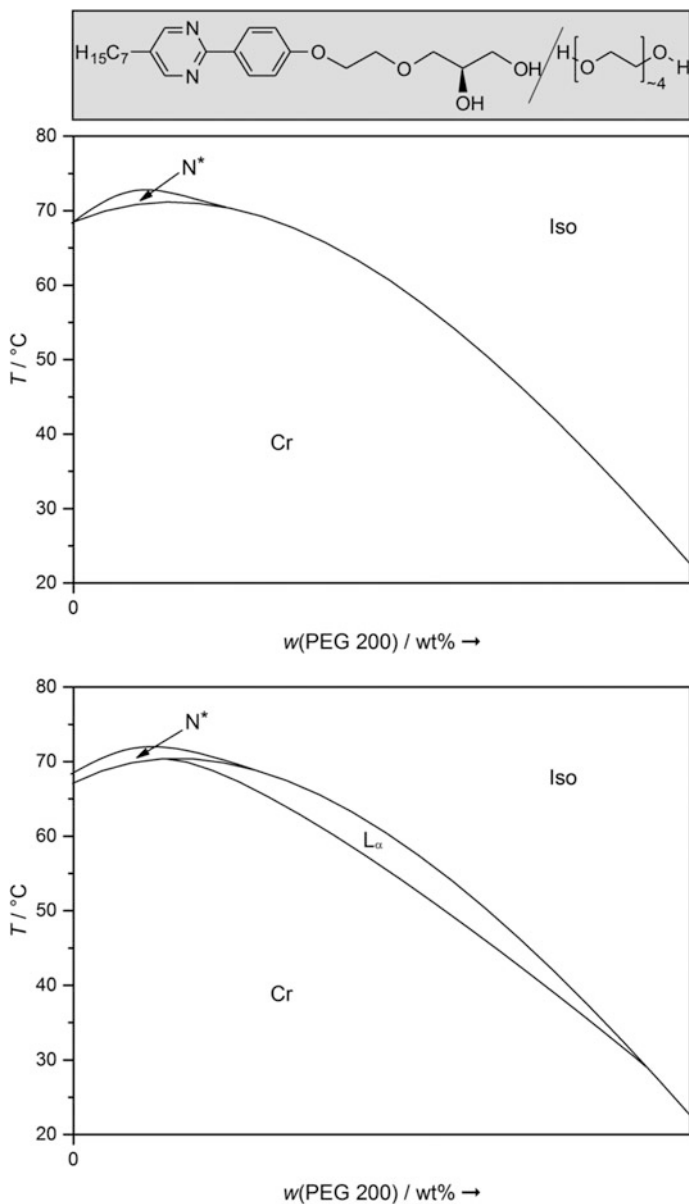


**Fig. 5.9** Schematic phase diagrams of the C5O/PEG 200 system, measured on heating (*top*) and on cooling (*bottom*). The only enantiotropic liquid crystalline phase in this system is a lyotropic  $\text{N}^*$  phase. On cooling, an additional lamellar  $\text{L}_\alpha$  phase appears, which is stable over 40 K but only in a very narrow concentration range

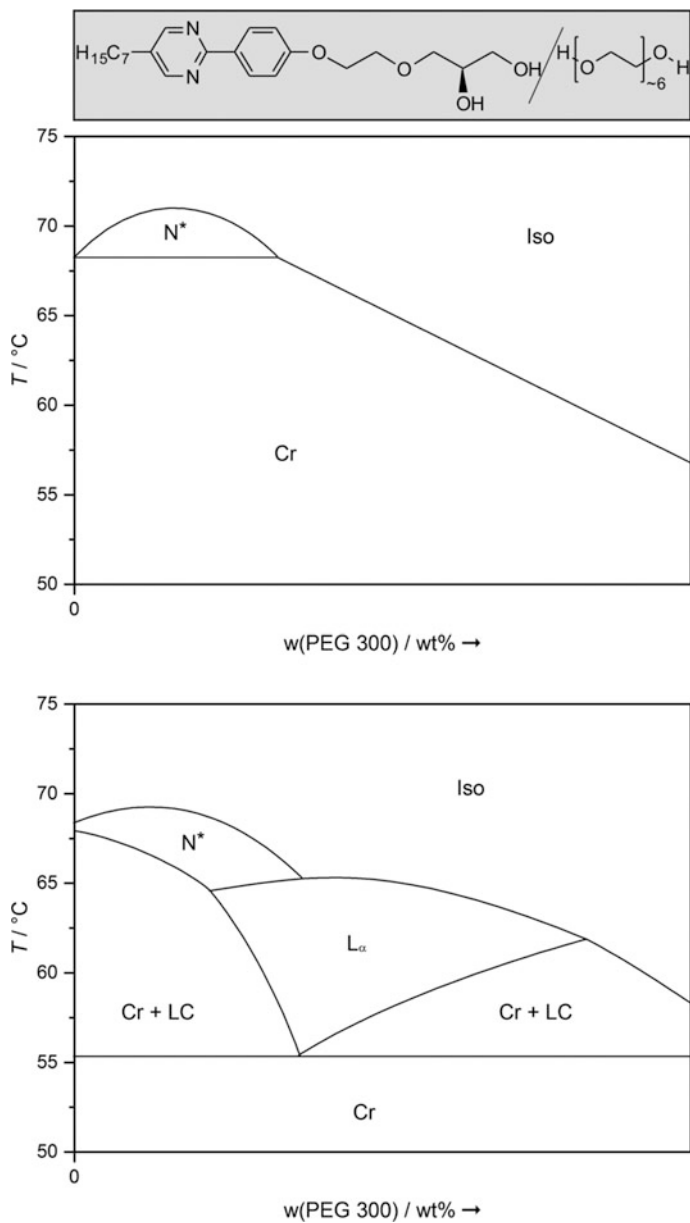


**Fig. 5.10** Schematic phase diagrams measured on heating (*top*) and cooling (*bottom*), which were derived from the contact region of C50 and polyethylene glycol 300

**Table 5.2** Derived physical data of selected solvents

Solvent	Dipole moment [15] $\mu$ (D)	Polarity [18] $E_{T30}$ (kcal mol <sup>-1</sup> )	Number of hydrogen bond donor atoms per molecule	Number density $n_p$ (cm <sup>-3</sup> )
Water	1.85	63.1	2	$3.266 \times 10^{22}$
Ethylene glycol	2.36	56.3	2	$1.080 \times 10^{22}$
PEG 200	–	–	2	$0.338 \times 10^{22}$
PEG 300	–	–	2	$0.226 \times 10^{22}$
Formamide	3.73	56.6	2	$1.516 \times 10^{22}$
NMF	3.83	55.5	1	$1.031 \times 10^{22}$
DMF	3.82	43.8	0	$0.777 \times 10^{22}$

The number density is calculated from the values in Table 5.1 according to  $n_p = \rho \cdot N_A/M$

If the remaining hydrogen atom in the *N*-methylamide group is also replaced by a second methyl group, the solvent dimethylformamide results, which does not possess any hydrogen bond donor atoms. In the contact region of this solvent with C5O, only an enantiotropic N\* phase and a monotropic lamellar L <sub>$\alpha$</sub>  phase appear (Fig. 5.13).

Thus, by going from formamide to *N*-methylformamide and finally dimethylformamide, the stabilization of the lyotropic liquid crystalline phases diminishes. Furthermore, formamide is the only one of these three solvents in which a lyotropic SmC\* analog phase is formed. Of these three solvents, formamide is the one with the smallest molecular volume and the highest polarity. In addition, it is also the only solvent in this row which possesses two hydrogen bond donor atoms.

Summing up, the only two solvents which possibly induce a lyotropic analog of the SmC\* phase in contact with the surfactant C5O are water and formamide. Both solvents possess quite small molecular volume and a highly polar structure. However, this is true for most of the solvents used. Thus, the question is which properties of the solvents enable the formation of a lyotropic SmC\* analog phase. In Table 5.2 some physical data of the selected solvents, which might be useful to answer this question, are listed. All of the solvents possess a quite polar chemical structure and thus have a relatively high dipole moment. But while formamide is almost on the upper end of the scale, water has the smallest dipole moment of the solvents used. Hence, the dipole moment of the solvent should not play an important part in the formation of the phase.

Things are different if the polarity of the solvent, deduced from solvatochromism [17], is considered. Here, both water and formamide possess the two highest polarities of all solvents investigated. Yet, ethylene glycol and *N*-methylformamide exhibit almost the same polarity. A further approach to answer the question is to have a look at the number of hydrogen bonds which the solvent molecules can form. Most of the solvents used possess two atoms per molecule, which can act as hydrogen bond donors. Merely, *N*-methylformamide does only have one hydrogen bond donor atom and dimethylformamide has none at all. By looking at the number

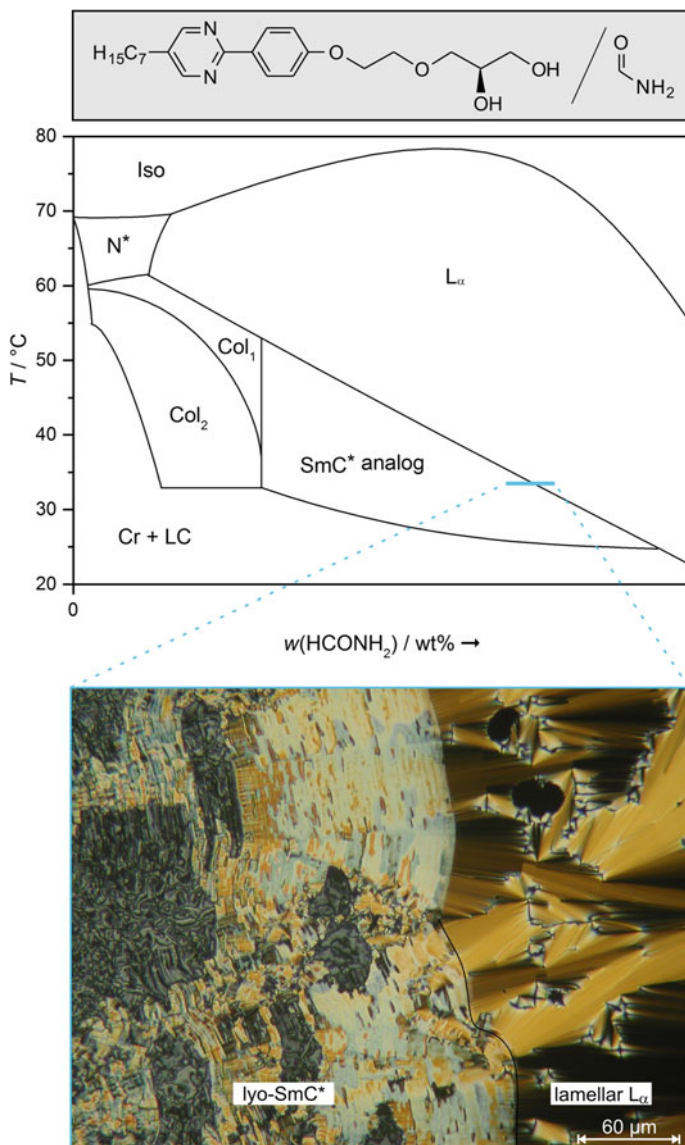


**Fig. 5.11** Schematic phase diagram of the C50/formamide system, which exhibits a lyotropic  $SmC^*$  analog phase (*top*) and texture image (*bottom*), taken at the position in the contact preparation indicated with a blue bar in the phase diagram

density  $n_p$  of the solvents, a clear trend can be seen. Formamide and especially water have by far the highest number density and thus also the highest hydrogen bond density.

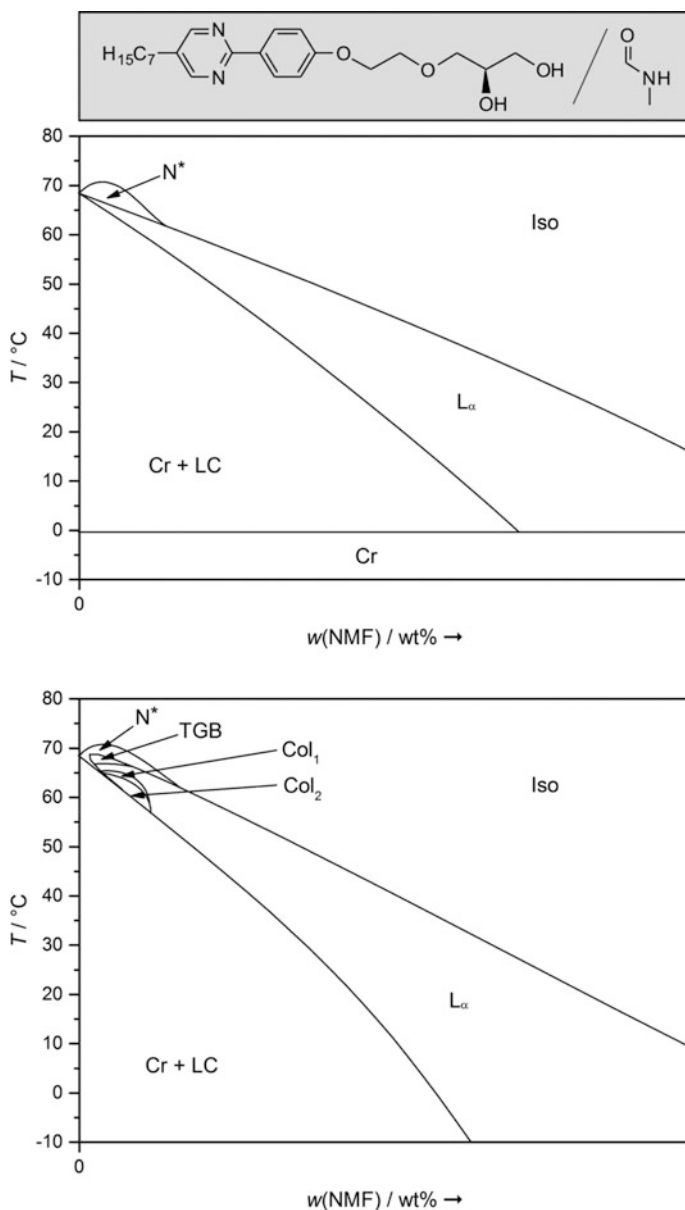


**Fig. 5.12** Schematic phase diagrams of C5O and *N*-methylformamide measured on heating (*top*) and on cooling (*bottom*)

In conclusion, the demands on the solvent do not only require a small molecular volume and a quite polar structure but also an exceptionally dense hydrogen bond network. This also explains, why the stabilization of the lyotropic SmC\* analog



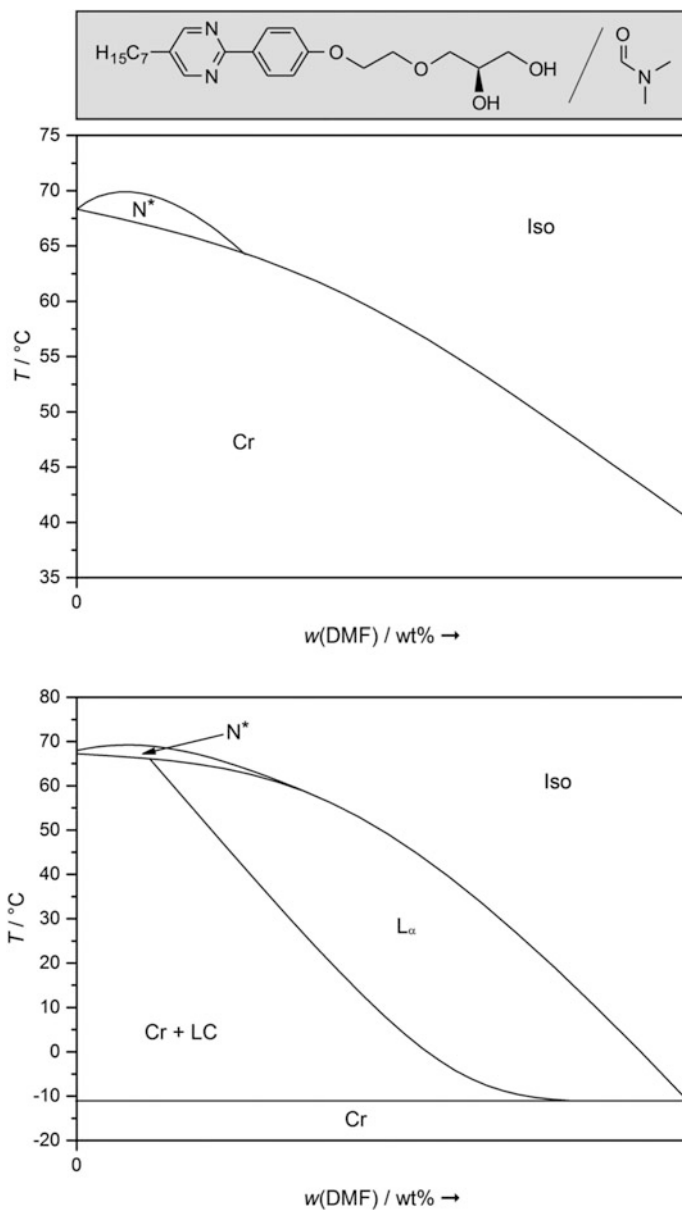


**Fig. 5.13** The *upper part* of the figure shows the schematic phase diagram of the system C5O/dimethylformamide measured on heating (adapted from [17]. Copyright 2015 Wiley-VCH Verlag GmbH & Co. KGaA. Reproduced with permission). The *lower part* displays the one measured on cooling

phase seems to be better with water than with formamide, as the number density of water is about two times higher as the one of formamide. Nonetheless, if considering the vapor pressure, formamide is the more convenient solvent from a practical point of view and facilitates an easier preparation of samples.

## 5.2 Phase Diagrams of Selected Solvent/Surfactant Mixtures

In the following subsection detailed phase diagrams of three solvent/surfactant mixtures will be presented. In two of those phase diagrams, i.e. the C5O/water and the C5O/formamide system, the lyotropic SmC\* analog phase can be found. Furthermore, as a counterexample for a C5O system in which the lyo-SmC\* phase does not occur, the C5O/*N*-methylformamide system was investigated. Characteristic textures of the individual phases will be displayed to document the correct assignment of the phases. Additionally, the other liquid crystalline phases which appear in the phase diagrams will be characterized briefly.

### 5.2.1 Phase Diagrams of C5O/Solvent Systems Exhibiting the Lyotropic SmC\* Analog Phase

As the phase diagrams as well as the properties of the occurring phases are very similar, the C5O/water and the C5O/formamide system will be discussed simultaneously. In Fig. 5.14 the phase diagram of mixtures of the diol C5O and water is shown. As no significant changes could be observed on cooling, only the phase diagram measured on heating is displayed here. The dominating phase in the phase diagram is the lamellar  $L_\alpha$  phase, which is stable over the entire investigated concentration range. At low solvent concentrations a narrow N\* phase appears. In mixtures with up to 40 wt% of water two different columnar or ribbon phases can be found, which will simply be denoted Col<sub>1</sub> and Col<sub>2</sub>. A more detailed characterization of these 2D-correlated phases will be given later in this subchapter. In the mass fraction regime between 25 and 70 wt% of water the lyotropic SmC\* analog phase is found over a temperature range of about 30 K. This clearly shows that the phase is a true lyotropic phase and not just an artifact of a thermotropic phase, as it only exists at elevated solvent concentrations. Thus, the solvent has to play an important role in its formation.

The phase diagram of C5O and formamide is displayed in Fig. 5.15. The sequence of the phases looks quite similar to the one of the phase diagram presented in Fig. 5.14. The most significant difference is that the lamellar  $L_\alpha$  phase is much more stabilized in mixtures with formamide than with water and thus, the other phases appear at lower solvent concentrations. As a result, the lyotropic SmC\* analog phase only occurs between 7 and 30 wt% of formamide. Moreover,

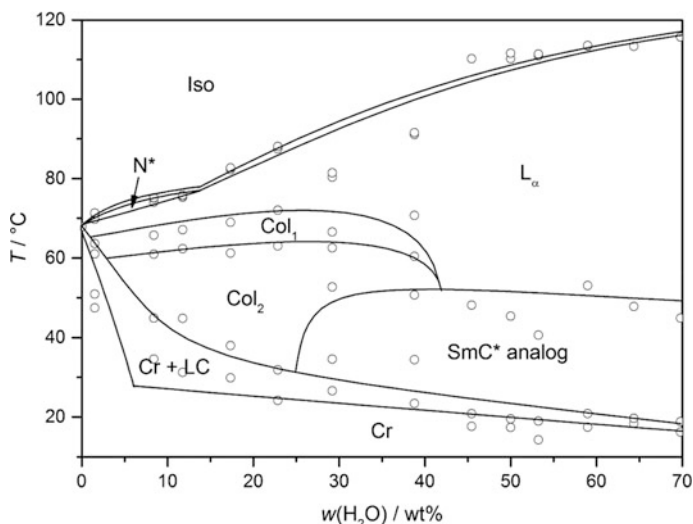


**Fig. 5.14** Phase diagram of the C5O/water system measured on heating. No significant changes could be observed on cooling (adapted from [17]. Copyright 2015 Wiley-VCH Verlag GmbH & Co. KGaA. Reproduced with permission.)

its temperature range is considerably enlarged on cooling. Due to this, the phase diagram of the C5O/formamide system measured on cooling is also shown (*cf.* bottom of Fig. 5.15).

For a tentative proof of the existence and correct phase assignment of the lyotropic analog of the SmC\* phase, the textures between crossed polarizers of this phase were investigated. In Fig. 5.16 a selection of representative textures of the lyo-SmC\* phase is shown. All these textures correspond very well to the characteristic textures known from thermotropic SmC and SmC\* phases [19] and thus emphasize the structural analogy between the lyotropic SmC\* analog and thermotropic SmC\* phase.

By cooling down from the homeotropically aligned lamellar  $L_\alpha$  phase, a schlieren texture appears (Fig. 5.16a). This change from the black homeotropic texture of the lamellar  $L_\alpha$  phase to the birefringent schlieren texture is a first sign of the formation of a tilted structure. Furthermore, all point singularities found in the texture are of the  $s = \pm 1$  type. This indicates that the observed schlieren texture does not belong to a nematic phase, as the schlieren texture of the nematic phase shows singularities with  $s = \pm 1$  as well as with  $s = \pm 1/2$ .

Figure 5.16b shows a broken fan texture, which results from cooling down the sample from the focal conic fan texture of the lamellar  $L_\alpha$  phase. The continuity of the fans suggests that the lamellar structure persists at the phase transition. However, the breaking of the fans again indicates the formation of a tilted structure.

The pictures in Fig. 5.16c, d belong to the same section of a surface-stabilized sample, which is rotated in different directions with respect to the crossed polarizers. The sample is prepared in a 1.6  $\mu\text{m}$  thick liquid crystalline measuring cell,

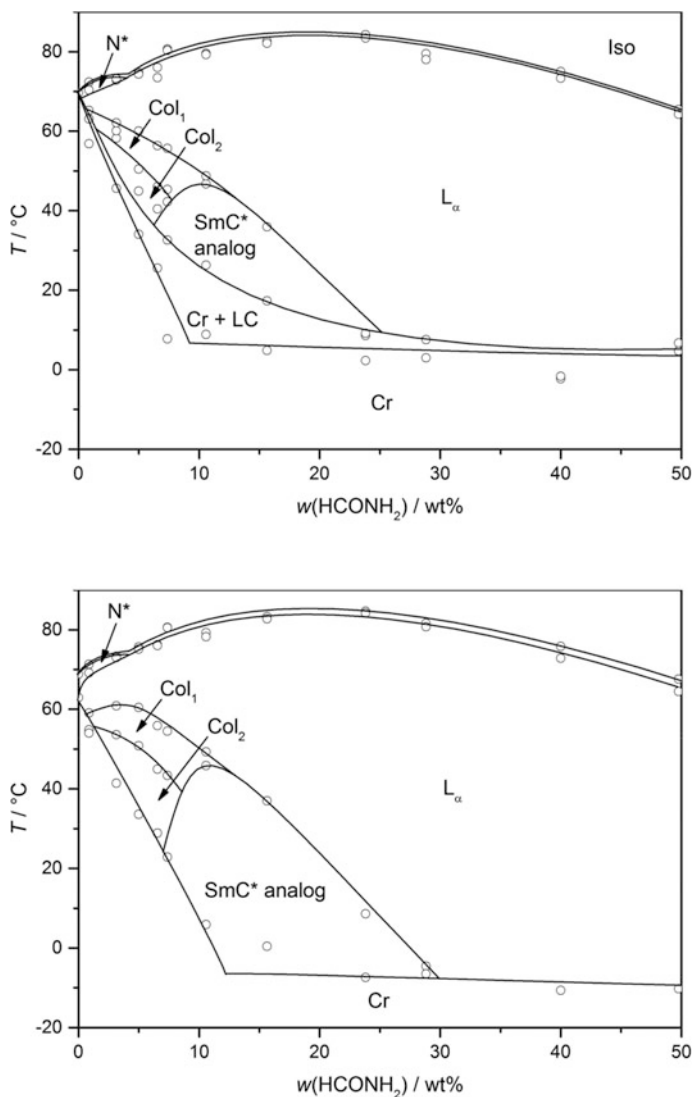


**Fig. 5.15** Phase diagram of C5O and formamide measured on heating (*top*) (adapted from [17]. Copyright 2015 Wiley-VCH Verlag GmbH & Co. KGaA. Reproduced with permission) and on cooling (*bottom*)

which is coated with a nylon layer to give planar alignment. The rubbing of the nylon layer causes a unidirectional orientation of the lamellar  $L_\alpha$  phase. By cooling down into the lyotropic  $SmC^*$  analog phase, clearly separated domains form, which belong to the two surface-stabilized orientations of the now tilted director  $\mathbf{n}$ . By rotating the sample by two times the tilt angle  $\theta$ , bright domains can be converted into dark domains and vice versa. This is once more strong evidence of the

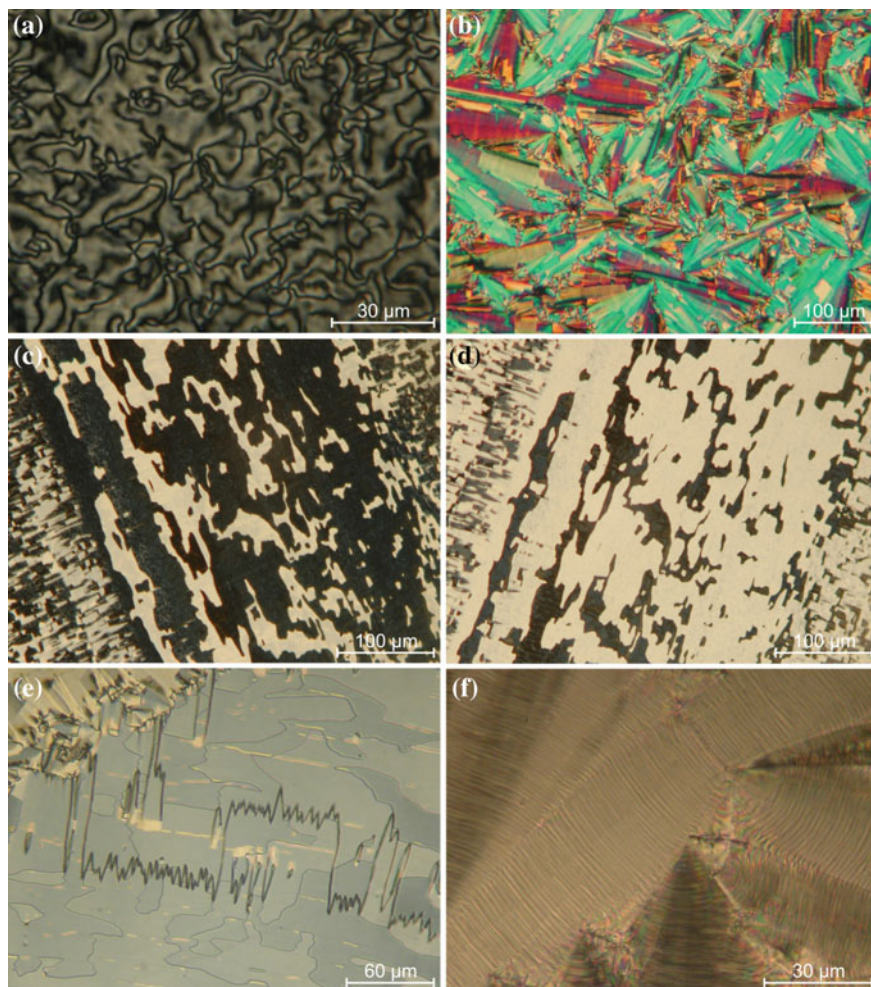


**Fig. 5.16** Characteristic textures of the lyotropic SmC\* analog phase formed by C50 and water or formamide: **a** schlieren texture at 60 °C and 42 wt% of water, **b** a broken fan texture at 47 °C and 65 wt% of water, **c** and **d** domains with opposite tilt directions in a surface-stabilized 1.6 μm thick cell at 28 °C and 17 wt% of formamide, **e** zigzag defect lines in a surface-stabilized sample at 25 °C and 50 wt% of water and **f** helical pitch lines in a thick sample at 30 °C and 32 wt% of formamide (adapted from [20]. Copyright 2013 Wiley-VCH Verlag GmbH & Co. KGaA, Weinheim. Reproduced with permission.)

existence of a tilted and lamellar structure and additionally provides a possibility to measure the magnitude of the tilt angle  $\theta$ .

A further consequence of the director tilt is a shrinking of the lamellar layer thickness at the phase transition from the orthogonal to the tilted phase (*cf.* Eq. 3.3). This leads to a transformation of the bookshelf configuration to a chevron configuration, which causes the formation of zigzag defect lines in thin samples [21].



Coherently, such zigzag defect lines can also be observed in surface-stabilized samples of the lyotropic  $\text{SmC}^*$  analog phase as shown in Fig. 5.16e.

Finally, sufficiently thick samples of planarly aligned thermotropic  $\text{SmC}^*$  phases are known to form a striped texture ('pitch lines') caused by the helical precession of the tilt direction (*cf.* Sect. 3.2.2). Such textures were also found for the lyotropic analog of the  $\text{SmC}^*$  phase in mixtures of C5O with water as well as with formamide, as shown in in Fig. 5.16f. This indicates that not only the tilt direction and magnitude correlate over a long range, but remarkably also the more subtle chirality-induced precession of the director. A more detailed description of the chirality effects in the lyotropic  $\text{SmC}^*$  analog phase will be given in Sect. 5.4.

The textures presented already deliver strong evidence that the lyotropic phase discussed possesses a lamellar, fluid and tilted structure. Further proof that this phase is indeed a lyotropic analog of the thermotropic  $\text{SmC}^*$  phase was obtained by more detailed structural investigations via X-ray diffraction (*cf.* Sect. 5.3).

To complete the characterization of the phases appearing in the measured phase diagrams, typical texture images of the remaining phases are shown in Fig. 5.17. The  $\text{N}^*$  phase exhibits a fingerprint texture with the pitch being in the range of a few  $\mu\text{m}$  or an oily streak texture as displayed in Fig. 5.17a. Most of the time, the lamellar  $\text{L}_\alpha$  phase shows a homeotropic texture with sporadic appearance of oily

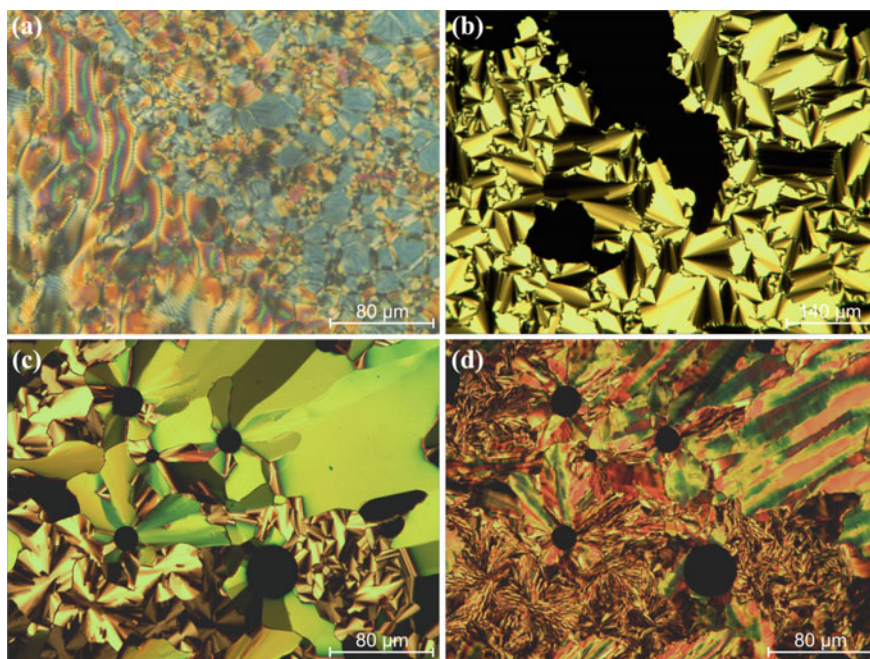


**Fig. 5.17** Textures of **a** the  $\text{N}^*$  phase at 74 °C and 1 wt% of formamide, **b** the lamellar  $\text{L}_\alpha$  phase at 23 °C and 11 wt% of formamide, **c** the  $\text{Col}_1$  phase at 63 °C and 5 wt% of water and **d** of the  $\text{Col}_2$  phase at 59 °C in the same sample as shown in picture (c)

streaks. On glass plates treated with polyimide a focal conic fan texture as well as homeotropic areas can be observed (Fig. 5.17b). A typical texture image of the Col<sub>1</sub> phase is presented in Fig. 5.17c. Depending on the orientation of the sample, the Col<sub>1</sub> phase exhibits either a platelet texture corresponding to the green parts of the image given or a pseudo-focal conic fan texture which usually has a grayish color. By cooling down into the Col<sub>2</sub> phase, the platelets as well as the pseudo-focal conic fans break into a multicolored texture, which is shown in Fig. 5.17d.

For a comprehensive characterization of the two columnar phases, X-ray diffraction measurements were performed. The two-dimensional X-ray diffraction patterns of partially aligned samples of the two columnar phases are displayed in Fig. 5.18a, b. The scattering image of the Col<sub>1</sub> phase (Fig. 5.18a) shows sharp reflections which basically originate from two domains, giving a mirror-imaged diffraction pattern. In the high temperature lamellar L<sub>α</sub> phase, only one layer peak appears which is vertically oriented. Thus, the two domains in the Col<sub>1</sub> phase suggest that the formerly lamellar structure breaks at the phase transition into two domains with opposite tilt. The indexation of the individual reflexes was done by overlaying the scattering image with a grid based on the oblique plane crystallographic group *p2*. Every reflex which occurs at a crosspoint of the grid belongs to the considered domain and its Miller indices can be assigned as shown in Fig. 5.18a. The indexation shown provides a good agreement of theoretical and experimental values. The X-ray diffraction pattern of the Col<sub>2</sub> phase in Fig. 5.18b is less sharp and the reflexes are smeared due to a poorer alignment of the low temperature columnar phase. Nonetheless, an indexation of the Col<sub>2</sub> phase on the basis of the two-dimensional oblique group *p2* is possible, yielding quite good results. The symmetry and indexation of the two columnar phases is almost identical. The only prominent difference between them is a deformation of the Col<sub>2</sub> phase along the two lattice directions, leading to a unit cell with a rhombic shape.<sup>3</sup> This suggests a close structural relationship between the columnar phases. As both columnar phases belong to the plane crystallographic group *p2*, the conventional lyotropic denotation for both phases is monoclinic M<sub>α</sub>.

To gain an impression of the structure of the Col<sub>1</sub> phase, corresponding electron density maps were calculated. The most likely one is shown in Fig. 5.18c. The map can be obtained from the scattering intensities of an unaligned sample by Fourier transform [22]. Further details on this method are found in the appendix. Areas of high electron density which can be assigned to the hydrophilic head groups and the water molecules are depicted in blue. The intermediate electron density of the aromatic cores is illustrated in green and the low electron density of the alkyl chains in red. Several molecules are drawn into the map to reveal a feasible structure of the Col<sub>1</sub> phase. It shows that there is still some structural relationship with the lamellar phase as the alkyl chains reflect the layered structure. However, the hydrophilic

---

<sup>3</sup>Due to the rhombic shape of the unit cell, it should also be possible to index the scattering pattern of the Col<sub>2</sub> phase on the basis of the plane crystallographic group *cm*. However, as the group *cm* possess mirror planes this would not be conform to the chirality of the molecules.

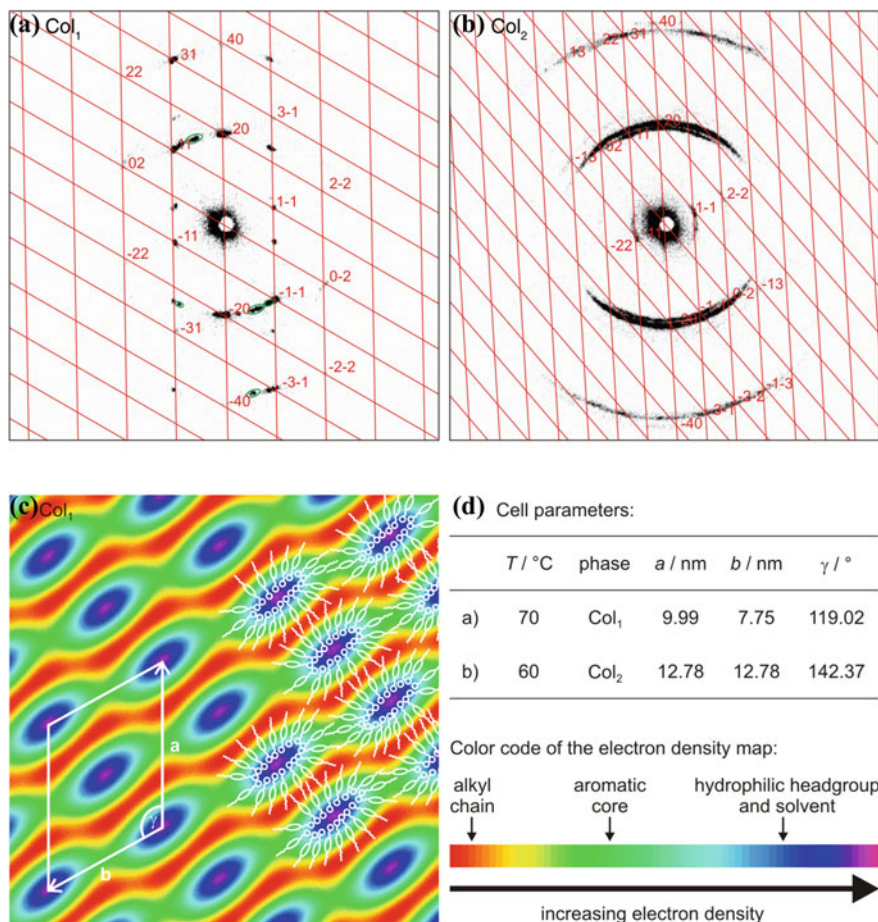


**Fig. 5.18** X-ray diffraction data of the two columnar phases. **a** 2D diffraction pattern of an aligned sample with two domains at 70 °C and 5.5 wt% of water in the Col<sub>1</sub> phase. The Miller indices of the reflexes originating from one of the domains are inserted in red. Reflexes which belong to other than the two main domains are marked with a green circle. **b** 2D diffraction pattern of the same sample at 60 °C in the Col<sub>2</sub> phase together with the Miller indices. **c** Calculated electron density map, which suggests a possible structure for the Col<sub>1</sub> phase. **d** Cell parameters corresponding to the X-ray diffraction data shown in (a) and (b)

head groups buckle into columns, which include the solvent molecules. This inverse-like structure seems to be reasonable because the mole fraction of the water molecules is only 0.55 in the investigated mixture. Furthermore, it is evident that the unit cell can be tilted in one or the other direction with respect to the layers of the lamellar  $L_\alpha$  phase. Due to this, two well aligned domains in the Col<sub>1</sub> phase originate from a single aligned domain in the lamellar  $L_\alpha$  phase.



In case of the  $\text{Col}_2$  phase, it was not possible to calculate an electron density map. This is due to the insufficient resolution of the X-ray diffraction detector which does not allow a sufficient separation of the individual reflexes. Nonetheless, the  $\text{Col}_2$  phase is expected to look similar to the  $\text{Col}_1$  phase except for the shape of the columns which should be circular instead of oval, as its lattice parameters  $a$  and  $b$  have the same values (*cf.* Fig. 5.18d).

### 5.2.2 *The C50/N-Methylformamide System: A Counterexample but not less Interesting*

As an example for a solvent with which the diol C50 does not form a lyotropic  $\text{SmC}^*$  analog phase, *N*-methylformamide (NMF) was chosen. The structural variation with respect to formamide is rather small; however, the impact on the lyotropic mesomorphism is substantial. In Fig. 5.19 the phase diagrams measured on heating and cooling are displayed. With *N*-methylformamide as the solvent, only two enantiotropic phases appear: a narrow  $\text{N}^*$  phase at low solvent concentrations and a very broad lamellar  $\text{L}_\alpha$  phase, which gets destabilized with increasing amount of solvent. Below 0 °C the mixtures become solid but do not properly crystallize suggesting a transition into a glassy state. During cooling several monotropic phases can be observed. Between 3 and 7 wt% the two columnar phases, which already formed with water and formamide, appear. Besides this, at even lower solvent concentrations two so far unobserved phases appear. The first one turns out to be a twist grain boundary (TGB) phase and the second one is a re-entrant cholesteric ( $\text{N}_{\text{RE}}^*$ ) phase. For a better visibility of these quite narrow phases, a magnified section of the phase diagram of the C50/*N*-methylformamide system is given in Fig. 5.20.

Up to now, there are no reports in literature about lyotropic or at least solvent-induced twist grain boundary phases. There is only one theoretical work by Kamien and Lubensky from 1997 [23], which states that lyotropic twist grain boundary phases should exist even though they were not reported up to then. Considering that the first report of a thermotropic twist grain boundary phase [24, 25] was only one year after its theoretical prediction [26], it is astonishing that no lyotropic analog was found for 17 years. Thus, the appearance of such a solvent-induced twist grain boundary phase is quite remarkable and needs further investigations. As no notation for a solvent-induced twist grain boundary phase exists so far, it is suggested to denote this phase as  $\text{TGBL}_\alpha^*$  phase. Besides the  $\text{TGBL}_\alpha^*$  phase, re-entrant cholesteric phases are also scarcely found in lyotropic systems, especially if the re-entrance occurs with respect to the temperature and not the solvent concentration. Therefore, the  $\text{N}_{\text{RE}}^*$  phase is also worth looking at. The main focus of this subchapter is, thus, on providing proof of the existence of the twist grain boundary as well as the  $\text{N}_{\text{RE}}^*$  phase.

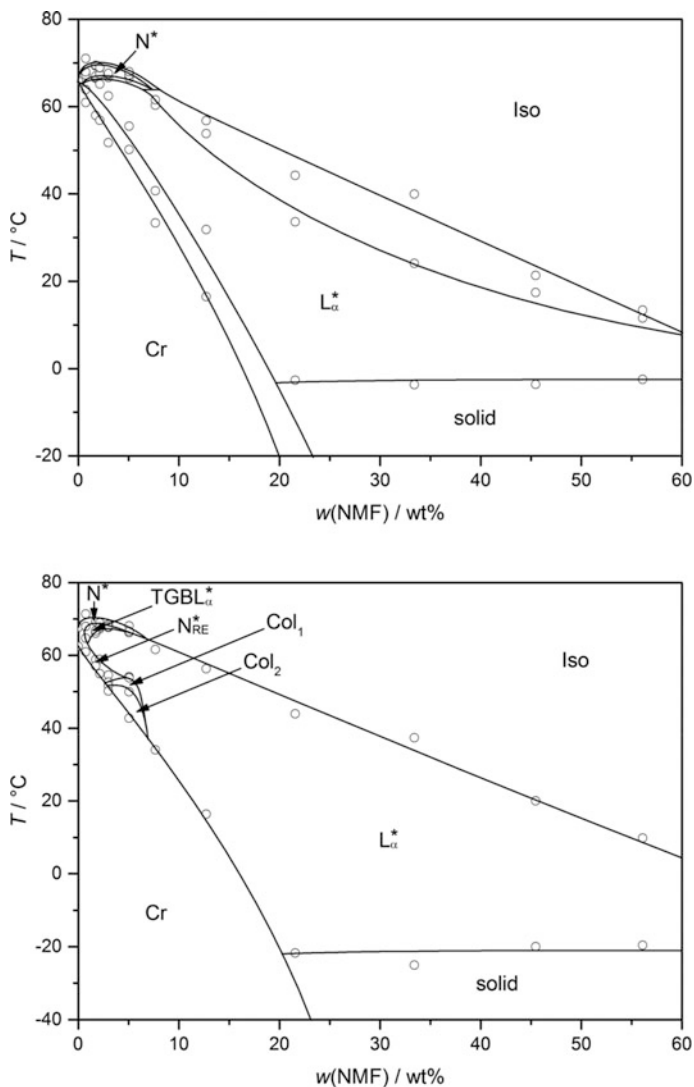


**Fig. 5.19** Phase diagrams of the C5O/*N*-methylformamide system measured on heating (*top*) (adapted from [17]. Copyright 2015 Wiley-VCH Verlag GmbH & Co. KGaA. Reproduced with permission.) and on cooling (*bottom*)

The two phases only exist in a concentration range between approximately 1 and 5 wt% of *N*-methylformamide (*cf.* Fig. 5.20). This corresponds to a maximum mole fraction of  $x(\text{NMF}) = 0.26$ . Therefore, these phases can hardly be seen as lyotropic in the sense that surfactant molecules are dissolved in a solvent. Nonetheless, the solvent has to play a very important role in their formation, as they do not appear in

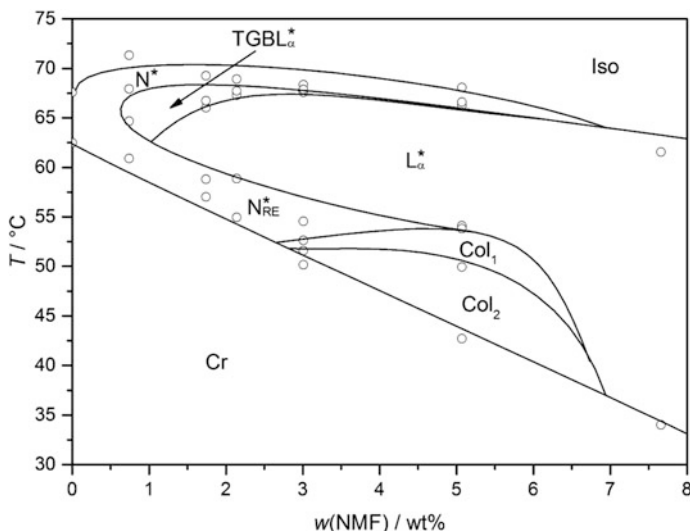


**Fig. 5.20** Magnified section of the phase diagram of the C5O/*N*-methylformamide system measured while cooling

the neat state or with other solvents. The two phases will thus be referred to as ‘solvent-induced’ rather than as ‘lyotropic’.

Characteristic textures are the first evidence for a correct phase assignment. In Fig. 5.21a the fingerprint texture of the  $N^*$  phase which forms on homeotropic anchoring conditions is shown. In the  $TGBL_\alpha^*$  phase a texture quite similar to the cholesteric fingerprint texture can be observed, which is displayed in Fig. 5.21b. However, the texture appears sharper due to the grain boundaries and turns into the so called filament texture at the phase transition to the homeotropically aligned chiral lamellar  $L_\alpha$  phase. This kind of texture is well known for thermotropic twist grain boundary phases [27] and thus already suggests the existence of a solvent-induced twist grain boundary phase. On planar anchoring conditions, the chiral lamellar  $L_\alpha$  phase exhibits a fan shaped texture (Fig. 5.21c). In the  $N_{RE}^*$  phase the oily streak texture occurs on untreated glass plates as can be seen in Fig. 5.21d. The observed textures already strongly indicate that the identification of the  $TGBL_\alpha^*$  phase and the  $N_{RE}^*$  phase is correct. Additional proof was provided by X-ray diffraction and measurements of the helical pitch in all macroscopically chiral phases. For these measurements a sample with 1 wt% of *N*-methylformamide was chosen, which possesses a  $N^*$ - $TGBL_\alpha^*$ - $N_{RE}^*$  phase sequence.

The results of the X-ray diffraction measurements can be seen in Fig. 5.22. In case of the  $N^*$  phase, the measurements clearly show a rather diffuse azimuthal orientation (Fig. 5.22b) and a low scattering intensity (Fig. 5.22a), which reflects the low order of the cholesteric structure. The same can be found for the  $N_{RE}^*$  phase (Fig. 5.22d), which proves the existence of the re-entrant phase. Additional to this scattering maximum, a second incommensurate scattering maximum can be found

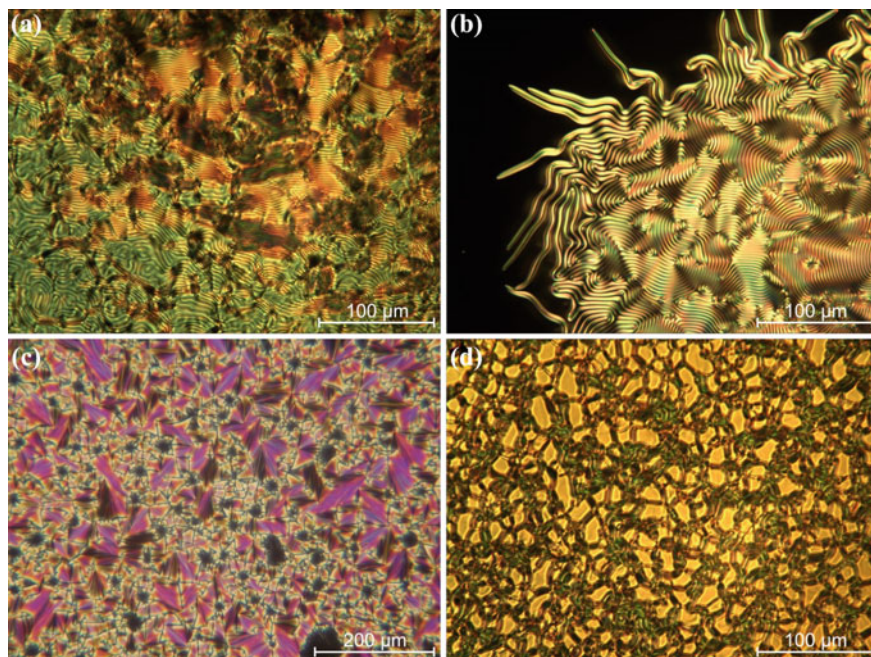


**Fig. 5.21** Texture images C50/NMF mixtures as seen through crossed polarizers of **a** the  $N^*$  phase with 2 wt% of NMF at 66 °C, **b** the phase transition from the homeotropically aligned  $L_\alpha$  phase to the filament texture of the  $TGBL_\alpha^*$  phase in a sample with 2 wt% of NMF at 65.5 °C, **c** the  $L_\alpha$  phase with 13 wt% of NMF at 50 °C and **d** the  $N_{RE}^*$  phase with 2 wt% of NMF at 55 °C

in the  $N_{RE}^*$  phase at  $2\theta = 3.8$  nm corresponding to  $d = 2.3$  nm, which is marked with an arrow in Fig. 5.22a. The occurrence of this second scattering maximum might possibly be explained by the formation of cybotactic clusters, related to a re-entrant lamellar phase, which is composed of monolayers instead of bilayers (*cf.* [28]).

Between the two cholesteric phases, the intensity of the X-ray scattering increases dramatically (Fig. 5.22a) and turns into rather sharp Bragg-peaks (Fig. 5.22c), related to a one-dimensional periodic layer structure. As scattering occurs solely on smectic blocks in which the director is oriented normal to the X-ray beam, only two layer peaks are found in the scattering image, reflecting an orientation of the helix axis perpendicular to the probing direction. Hence, the phase cannot be distinguished from the lamellar  $L_\alpha$  phase by the performed X-ray measurements alone.

To show that the observed  $TGBL_\alpha^*$  phase does not only possess a lamellar structure as proven with X-ray diffraction, but that it also possesses a macroscopically helical structure, it was also investigated with polarized optical microscopy. A sample with the same concentration of *N*-methylformamide as used in the X-ray diffraction measurements was prepared and annealed between untreated glass plates to achieve a characteristic fingerprint texture in the  $N^*$  phase. Texture images of this

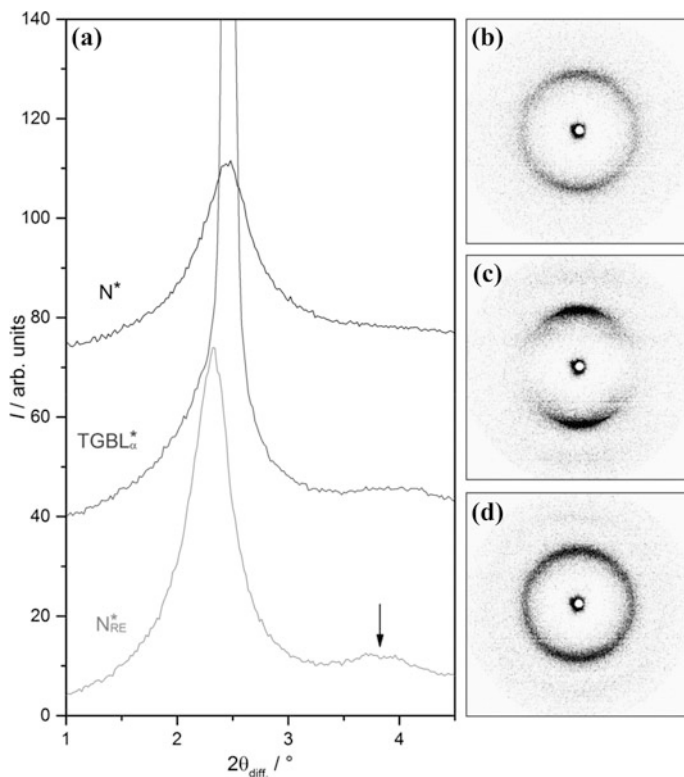


**Fig. 5.22** X-ray diffraction data of a sample of C5O with 1 wt% of NMF. **a** Scattering intensity profiles of the different phases and the corresponding 2D diffraction images of **b** the  $N^*$  phase at 72 °C, **c** the  $TGBL^*_{\alpha}$  phase at 68 °C and **d** the  $N^*_{RE}$  phase at 62 °C

sample can be found in Fig. 5.23. In the  $N^*$  phase the fingerprint texture is rather diffuse and faint (Fig. 5.23d). At the phase transition to the twist grain boundary phase, the texture becomes blurry and then turns into the quite sharp and more birefringent filament texture of the twist grain boundary phase (Fig. 5.23c). By further cooling down, the texture becomes blurry again and transforms back into the faint and diffuse fingerprint texture of the  $N^*_{RE}$  phase (Fig. 5.23b). These observations in the change of the textures strongly suggest the presence of three individually macroscopically chiral phases. The value of the pitch was derived from the texture images (*cf.* Sect. 4.5.1). The result is plotted in Fig. 5.23a. The value of the helical pitch is between 4 and 5  $\mu\text{m}$  for all three phases. Despite this, explicit jumps in the temperature dependence of the pitch mark the two phase transitions. Together with the X-ray diffraction data these results confirm that the phase sequence  $N^*-TGBL^*_{\alpha}-N^*_{RE}$  is correct. Up to now, this is the first report of a solvent-induced twist grain boundary phase.

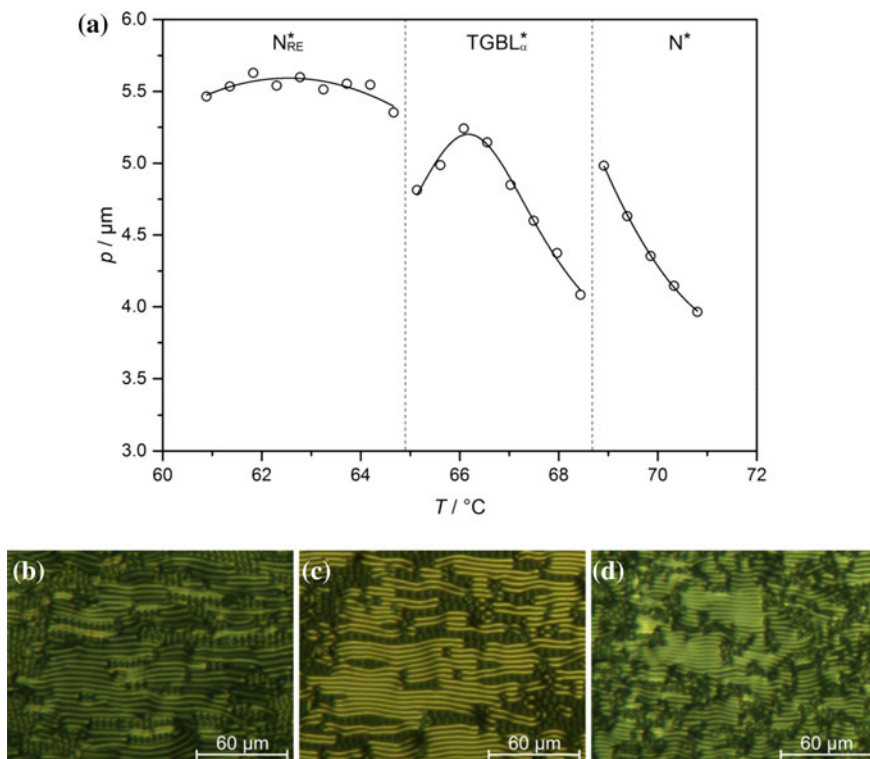


**Fig. 5.23** a Helical pitch versus temperature for the three macroscopically chiral phases and corresponding texture images of **b** the  $N_{RE}^*$  phase at 65  $^{\circ}\text{C}$ , **c** the  $TGBL_{\alpha}^*$  phase at 68  $^{\circ}\text{C}$  and **d** the  $N^*$  phase at 71  $^{\circ}\text{C}$

### 5.3 Structural and Physical Properties of the Lyotropic SmC\* Analog Phase

The following section is devoted to the investigation of the structural properties of the lyotropic SmC\* analog phase. In this context three major issues will be addressed. The first issue is to provide further proof of the existence of the lyotropic analog of the thermotropic SmC\* phase. The second one is to find out if the structure of the lyotropic phase differs from its thermotropic counterpart and the last point is to examine the influence of the solvent concentration on the structural and physical properties of the lyotropic SmC\* analog phase.



### 5.3.1 X-Ray Diffraction Measurements

Fundamental insight into the structure of any liquid crystalline phase can be obtained by two-dimensional X-ray diffraction on an aligned sample. Diffraction patterns of a sample of C5O with 65 wt% of water can be found in Fig. 5.24. In the lamellar  $L_\alpha$  phase (Fig. 5.24a) the maxima of the diffuse wide-angle scattering, which originate from the intralamellar distances between the diol molecules, are perpendicular to the small-angle peaks, which are due to the Bragg-scattering from the one-dimensional periodic lamellar structure. The director  $\mathbf{n}$  and the layer normal  $\mathbf{k}$  are thus parallel to each other and the measured two-dimensional diffraction pattern completely complies with the diffraction pattern expected for a lyotropic lamellar  $L_\alpha$  phase or a thermotropic SmA\* phase.

After cooling down into the lyotropic SmC\* analog phase, the diffraction pattern changes into the one shown in Fig. 5.24b. The scattering image still exhibits diffuse wide-angle peaks, indicating that the probed phase is fluid. Furthermore, the intensity of the layer reflections increases and a 2nd order peak appears in the small angle region. This shows that the lamellar order does not only persist but is strongly enhanced in the lyo-SmC\* phase, resulting in an increased smectic order parameter  $\Sigma$ . But the most noteworthy feature of the scattering image is that azimuthal maxima in the small and wide-angle regime are no longer perpendicular to each other. Thus, the director  $\mathbf{n}$  and the layer normal  $\mathbf{k}$  are no longer parallel to each other, but include the tilt angle  $\theta$ . Furthermore, this shows that the diol molecules in every lamella tilt in the same direction, because otherwise the scattering maxima should

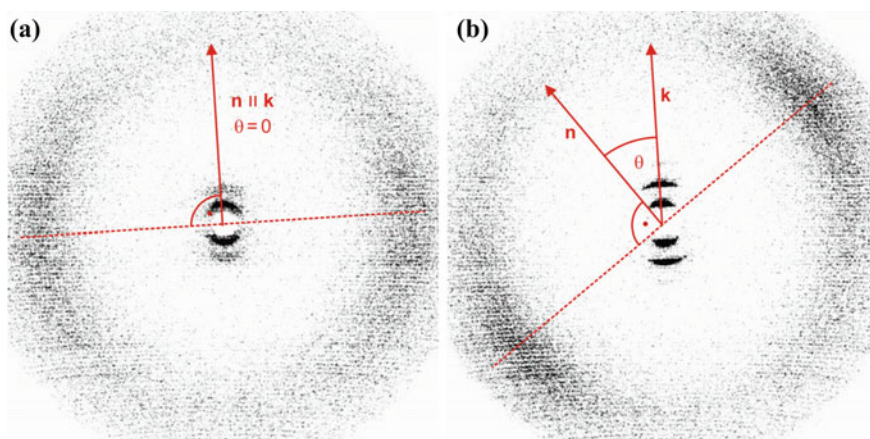


**Fig. 5.24** 2D-diffraction patterns of an aligned sample of the diol C5O with 65 wt% of water in **a** the lamellar  $L_\alpha$  phase at 89 °C and **b** the lyotropic SmC\* analog phase at 38 °C. The director  $\mathbf{n}$ , the layer normal  $\mathbf{k}$  and the tilt angle  $\theta$  are indicated in both scattering images (adapted from [20]. Copyright 2013 Wiley-VCH Verlag GmbH & Co. KGaA, Weinheim. Reproduced with permission.)

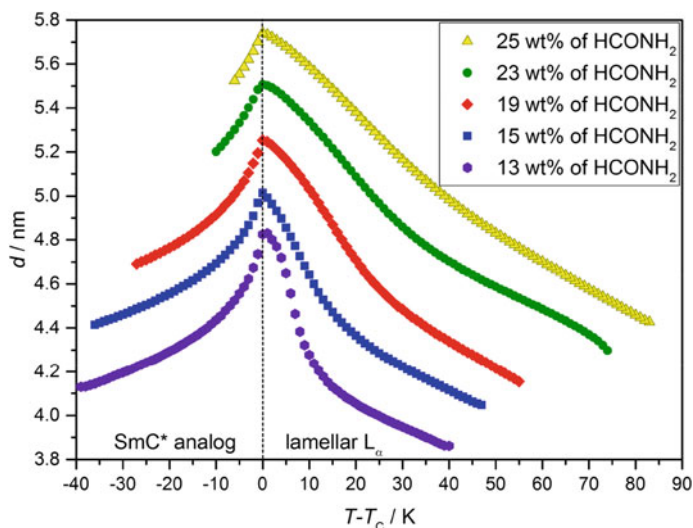


**Fig. 5.25** Temperature-dependent layer spacing of different C5O/formamide mixtures (See Footnote 4)

not shift to one direction but should only get broader. In case of Fig. 5.24 the tilt angle  $\theta$  reaches a rather high value of about  $36^\circ$ .

In conclusion, the two-dimensional scattering image of the lyotropic SmC\* analog phase measured clearly confirms that the phase possesses a lamellar structure which is composed of fluid layers, that the molecules in these layers are tilted with respect to the layer normal  $\mathbf{k}$  and that there is a long range correlation of the tilt directions. Hence, the investigated liquid crystalline phase indeed fulfills all conditions to be the lyotropic counterpart of the thermotropic SmC\* phase. This can be considered as sufficient proof of the existence and correct phase assignment of the lyotropic SmC\* analog phase.

To learn more about the temperature dependence of the layer spacing, one dimensional X-ray diffraction measurements were performed. The resulting layer spacings for samples with different concentrations of formamide are plotted in Fig. 5.25.<sup>4</sup> For all concentrations the layer spacing increases in the lamellar  $L_\alpha$  phase while cooling down. This negative thermal expansion can be explained by a progressive stiffening of the alkyl chains with decreasing temperature as well as an increasing orientational order, which leads to an increase of the smectic layer thickness [29]. At the phase transition towards the lyo-SmC\* phase, the layer spacing is at its maximum value and by further cooling down it starts to decrease again. This decrease in the lyotropic SmC\* analog phase is due to the increasing tilt angle, which causes a shrinkage of the layers (*cf.* Eq. 3.3). This very characteristic

<sup>4</sup>The measurements in Fig. 5.25 were partially performed by Marc Harjung and Friederike Knecht within the scope of a supervised research project.



temperature dependence is well known from thermotropic SmC\* phases and was found likewise for mixtures of C5O and water.

As can be seen in Fig. 5.25 the layer spacing increases with an increasing amount of formamide. This is plausible considering the structure of the lamellar  $L_\alpha$  phase (*cf.* Sect. 3.2.2). In this phase the repeat distance measured by X-ray diffraction is composed of two parts. The first part is a partial or full bilayer of surfactant molecules in which the hydrophilic head groups are surrounded by solvent molecules causing a slight swelling of the surfactant layer. If the solvent concentration exceeds the amount of solvent molecules which can be incorporated into the surfactant layer, the solvent molecules start to build up a separate solvent layer which corresponds to the second part of the overall layer thickness. The easiest way to describe the layer thickness  $d(T, w)$  is thus to separate it into the thickness of the solvent layer  $d_s(w)$ , which in a first approximation solely depends on the mass fraction  $w$  of formamide, and into the thickness of the diol bilayer  $d_{bl}(T)$ , which mainly depends on the temperature  $T$ :

$$d(T, w) = d_s(w) + d_{bl}(T). \quad (5.1)$$

According to this equation the measured layer spacing is plotted versus the weight fraction  $w$  of formamide for different temperatures  $T - T_C$  relative to the lamellar  $L_\alpha$  to lyotropic SmC\* analog phase transition and fitted with a uniform slope. In Fig. 5.26 the data sets for six exemplary relative temperatures and the

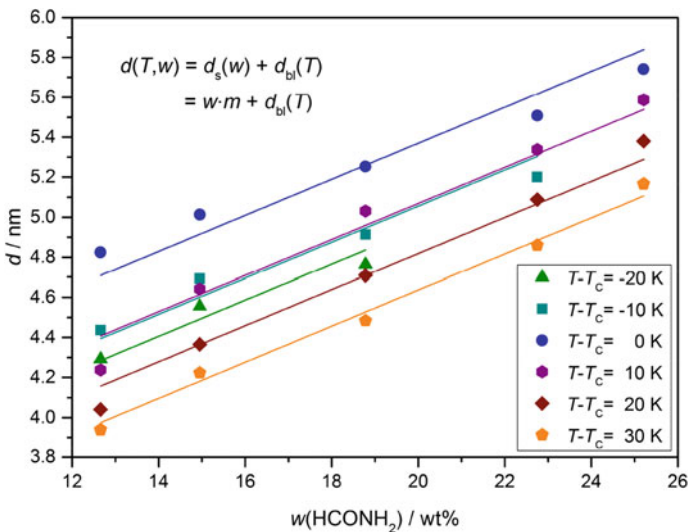


**Fig. 5.26** Plot of the layer spacing  $d$  versus the mass fraction of formamide  $w(\text{HCONH}_2)$  for several selected temperatures  $T - T_C$  relative to the lamellar  $L_\alpha$  to lyotropic SmC\* analog phase transition. The lines show linear fits to the data with a uniform slope  $m$

corresponding linear fits are shown. For this kind of diagram, Eq. 5.1 can be written as

$$d(T, w) = w \cdot m + d_{bl}(T) \quad (5.2)$$

with the slope  $m$  and the intercept  $d_{bl}(T)$  of the linear fit. With the help of these fit parameters, theoretical values for the bilayer and the solvent layer thickness are calculated as shown in Fig. 5.27.

By plotting the intercepts  $d_{bl}(T)$  versus the relative temperature  $T - T_C$ , the temperature dependence of a hypothetical bilayer thickness for 0 wt% of formamide is obtained (Fig. 5.27b). It exhibits the typical temperature dependence expected for a thermotropic SmA to SmC phase transition. The two kinks in the extrapolated data at  $T - T_C = -6$  and  $-10$  are caused by the reduction of analyzable data points due to the crystallization of the samples with high solvent layer concentration. At the lamellar  $L_\alpha$  to lyo-SmC\* phase transition the calculated layer spacing is at its

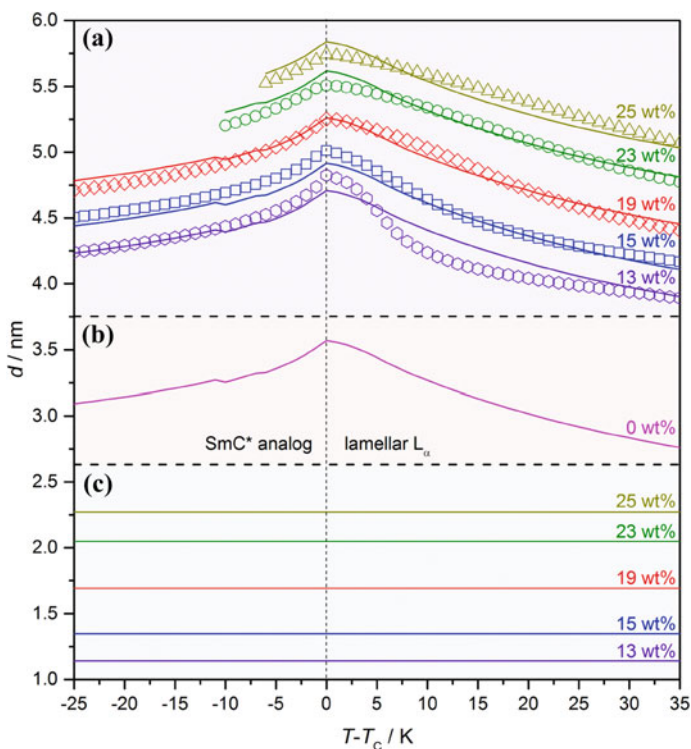


**Fig. 5.27** Extrapolated values obtained by fitting Eq. 5.2 to the measured layer spacing. **a** Measured (*symbols*) and calculated layer spacing (*lines*) for different mass fractions of formamide as indicated in the graph. **b** Layer spacing extrapolated to a hypothetical mass fraction of 0 wt% of formamide. **c** Extrapolated solvent layer thickness for different mass fractions of formamide

maximum reaching a value of 3.6 nm. Considering the calculated energy minimized length of the diol C5O being 2.49 nm,<sup>5</sup> the diol molecules have to form a partial bilayer in which the molecules interdigitate significantly, as the extrapolated value lies well between the one for a single and a full bilayer.

The solvent layer thickness  $d_s(w)$  for different mass fractions of formamide is calculated from the slope  $m$  (Fig. 5.27c). It varies between 1.1 and 2.3 nm in the investigated concentration regime.

By adding up the values for  $d_s(w)$  and  $d_{bl}(T)$ , the calculated repeat distance  $d(T, w)$  is obtained and plotted in Fig. 5.27a (lines) together with the measured data points (symbols). The deviation of the plots shows that the simple assumption of the solvent layer's thickness solely depending on the mass fraction of the solvent, and the diol bilayer's thickness being only influenced by temperature, can give a qualitative description of the measured X-ray data, but not a quantitative one. Further refinement is needed to correctly explain the dependence of the layer spacing on the temperature and solvent concentration. Nonetheless, the simple model can give a rough estimation of the bilayer thickness in the lamellar  $L_\alpha$  as well as in the lyotropic SmC\* analog phase and reveals that the thickness of the solvent layer is in the range of a few nanometers.

### 5.3.2 Measurement of the Director Tilt

In the preceding subchapter it was already demonstrated that the diol molecules in the SmC\* analog phase possess a macroscopic tilt  $\theta$  with respect to the layer normal. To gain information about its magnitude and temperature dependence, the director tilt was measured optically as described in Sect. 4.4. The results of these measurements are presented in Fig. 5.28 for different concentrations of formamide.<sup>6</sup> In general, the tilt angle starts at quite low values right after the lamellar  $L_\alpha$  to lyo-SmC\* phase transition and then increases while cooling. Depending on the formamide concentration, the maximum values as well as the temperature dependence of the measured tilt angles  $\theta_{opt}$  differ. To enhance the lucidity of Fig. 5.28 the measured values are fitted according to  $\theta_{opt} \propto |T - T_C|^\beta$ . For high formamide concentrations, the slope is rather gentle and the tilt angle reaches small values in the order of  $12^\circ$  for a sample of C5O with 25 wt% of formamide. By decreasing the formamide concentration the slope of the curves becomes steeper and steeper and the tilt reaches quite high values, e.g.  $\theta = 27.0^\circ$  for a sample with 15 wt% of formamide. This change in the temperature dependence of the measured tilt angles suggests that the phase transition shifts from 2nd to 1st order with decreasing

---

<sup>5</sup>Derived from molecular modeling with the software *Chem3D Pro 13.0* by CambridgeSoft on the AM1 level.

<sup>6</sup>The measurements in Fig. 5.28 were partially performed by Friederike Knecht within the scope of a supervised research project.

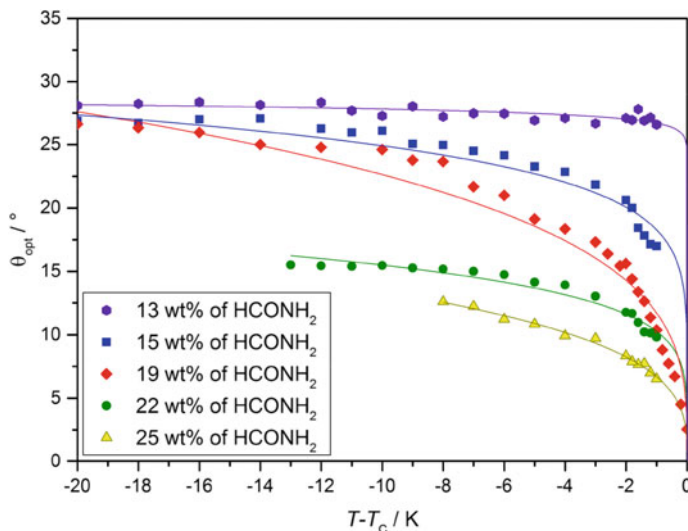


**Fig. 5.28** Optically measured director tilt angle  $\theta_{\text{opt}}$  of different C5O/formamide mixtures in dependence of the temperature  $T - T_C$  relative to the lamellar  $L_a$  to lyotropic SmC\* analog phase transition (adapted from [17]). Copyright 2015 Wiley-VCH Verlag GmbH & Co. KGaA. Reproduced with permission (See Footnote 6)

amount of solvent. Further evidence for this change in the nature of the phase transition will be provided in the following subchapter by means of DSC measurements.

In case of the sample with 13 wt% of formamide, the tilt angle rises abruptly to a quiet high, almost constant value of  $\theta_{\text{opt}} = 27^\circ$ . Here the phase transition towards the SmC\* analog phase does not take place from the lamellar  $L_a$  phase but from the  $\text{Col}_1$  phase.

For a comprehensive understanding of the director tilt in the lyotropic SmC\* analog phase, the tilt angle  $\theta_{\text{steric}}$  was calculated from the layer spacing according to Eq. 3.3. For this only the thickness of the bilayer  $d_{\text{bl}}(T)$  was used, which corresponds to the layer spacing extrapolated to a hypothetical mass fraction of 0 wt% of formamide (*cf.* Sect. 5.3.1). The resulting tilt angles  $\theta_{\text{steric}}$  are plotted in Fig. 5.29 in dependence of the relative temperature. Here, the tilt angle rises from  $0^\circ$  to values slightly higher than observed by the optical measurement of the tilt angle.

According to the simple model proposed in Sect. 5.3.1, the temperature dependence of the bilayer thickness  $d_{\text{bl}}(T)$  should be the same for every mass fraction of formamide and thus the tilt angles  $\theta_{\text{steric}}$  should also be the same for each formamide concentration. In consequence,  $\theta_{\text{steric}}$  does not show any concentration dependence, while  $\theta_{\text{opt}}$  decreases with increasing formamide concentration. Even though the tilt angles obtained by the two methods cannot be compared readily, as the methods probe different segments of the molecules [29], this is an interesting observation.

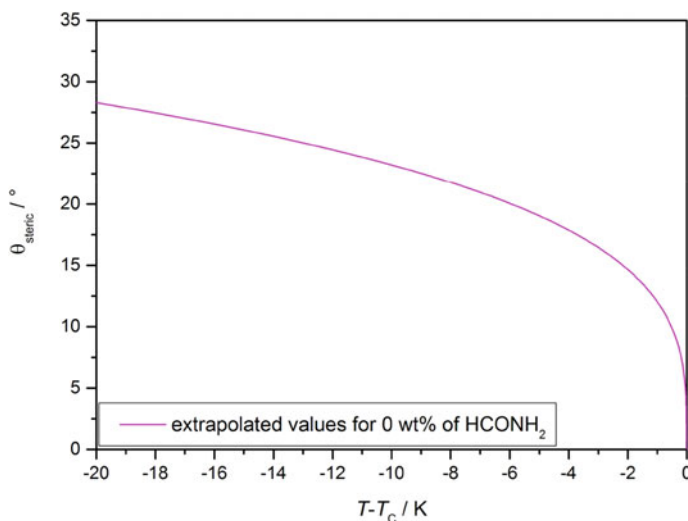


**Fig. 5.29** Tilt angle  $\theta_{\text{steric}}$  calculated from the extrapolated layer spacing of C5O with a hypothetical mass fraction of 0 wt% of formamide (*cf.* Fig. 5.27) in dependence of the temperature  $T - T_c$  relative to the lamellar  $L_\alpha$  to lyotropic SmC\* analog phase transition

While the optical measurements take the long-range correlation of the magnitude as well as the direction of tilt into account, the tilt angles derived from the layer spacing solely include the magnitude of the tilt angle. Hence, the deviance might indicate that the magnitude of the molecular tilt inside the bilayers does not change with the solvent concentration, whereas the long-range correlation of the tilt direction does. As a result, the local directors of the individual lamellas in the lyotropic SmC\* analog phase would shift from highly ordered to rather randomly orientated with increasing solvent concentration. This seems to be quite plausible because in conventional lyotropic liquid crystals, the solvent layer is seen as a rather disordered fluid and thus an increasing solvent layer thickness might disturb the tilt correlation mechanism between adjacent bilayers.

### 5.3.3 Calorimetric Investigations

As already discussed in Sect. 5.3.2, the lamellar  $L_\alpha$  to lyo-SmC\* phase transition seems to shift from 1st to 2nd order with increasing formamide concentration. To further confirm this crossover, the thermodynamic nature of the phase transition was investigated by differential scanning calorimetry (DSC). For this, samples with different concentrations of formamide were measured on heating and cooling (*cf.* Sect. 4.2). The detected heat flow of the individual samples is plotted in Fig. 5.30.

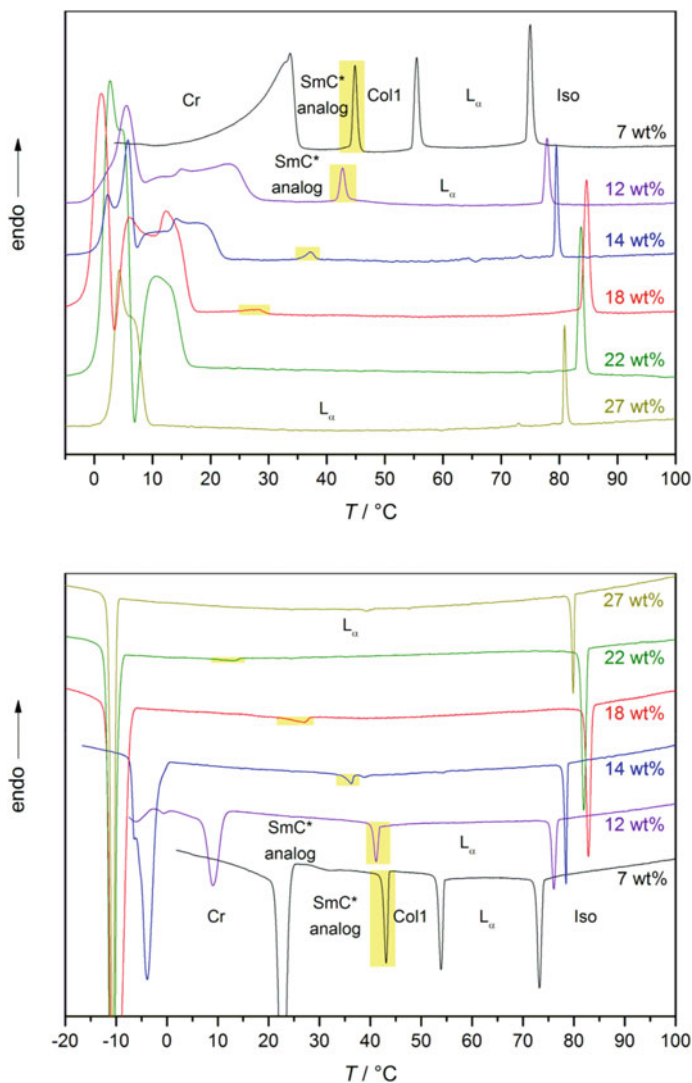


**Fig. 5.30** DSC thermograms measured on heating (*top*) and cooling (*bottom*) for different compositions of C50 and formamide. Peaks corresponding to a phase transition between the lyotropic SmC\* analog and a further liquid crystalline phase are highlighted in *yellow*

In the mixture with 7 wt% of formamide three liquid crystalline phases can be found, namely the lyotropic SmC\* analog phase, the Col<sub>1</sub> phase and the lamellar  $L_\alpha$  phase. The mixtures between 12 and 22 wt% of formamide only exhibit the lyotropic SmC\* analog phase and the lamellar  $L_\alpha$  phase. While the DSC curves of the sample with 12 wt% of formamide still show a very pronounced peak at the lyotropic SmC\* analog to lamellar  $L_\alpha$  phase transition, the peak becomes smaller and

smaller by increasing the formamide concentration. In the samples with 18 and 22 wt% of formamide the phase transition is marked by a step in the heat flow rather than by a real peak (Fig. 5.31). This trend can also be confirmed by looking at the phase transition enthalpies  $\Delta_{tr}H$  in Table 5.3, which diminish significantly with an increasing amount of formamide. Thus, the measurements clearly demonstrate that the phase transition shifts from 1st to 2nd order with increasing formamide concentrations. In case of the sample with 22 wt% of formamide no transition enthalpy  $\Delta_{tr}H$  could be detected at all. The sample with 27 wt% of formamide is a reference specimen which only shows the lamellar  $L_{\alpha}$  phase.

Furthermore, the phase transition temperatures detected by means of differential scanning calorimetry match those determined by polarized optical microscopy. The DSC measurements thus also confirm the phase diagrams shown in Fig. 5.15.

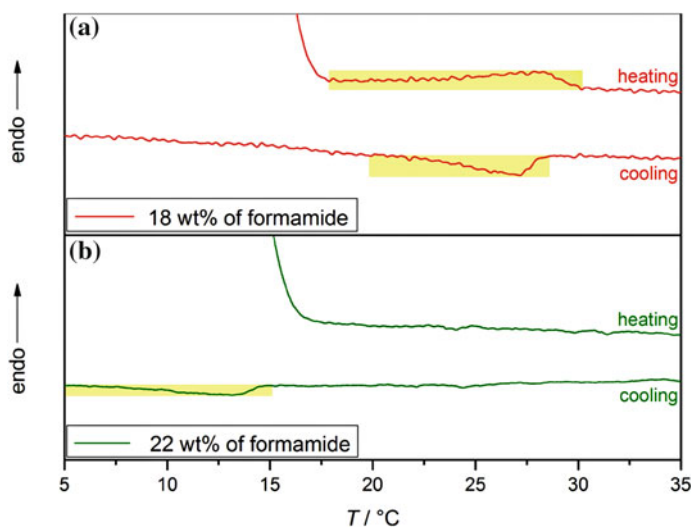


**Fig. 5.31** Enlargement of the DSC thermograms of the C50 samples with **a** 18 wt% of formamide and **b** 22 wt% of formamide. Peaks corresponding to the lamellar  $L_{\alpha}$  to lyo-SmC\* phase transition and vice versa are highlighted in yellow

**Table 5.3** Transition enthalpy  $\Delta_{tr}H$  of the lyotropic SmC\* analog to lamellar  $L_{\alpha}$  or  $Col_1$  phase transition measured on heating and vice versa on cooling of C50 with mass fractions of formamide

w(HCONH <sub>2</sub> ) (wt%)	High temperature phase	$\Delta_{tr}H$ (heating) (J g <sup>-1</sup> )	$\Delta_{tr}H$ (cooling) (J g <sup>-1</sup> )
7	$Col_1$	2.0	-2.1
12	$L_{\alpha}$	1.7	-1.8
14	$L_{\alpha}$	0.7	-1.2
18	$L_{\alpha}$	0.5	-0.5
22	$L_{\alpha}$	Not detectable	Not detectable

## 5.4 Chirality Effects in the Lyotropic SmC\* Analog Phase

The investigated surfactant/solvent mixtures of the diol C5O and water or formamide, respectively, are the first lyotropic systems to form a lamellar, fluid and tilted liquid crystalline phase which contains chiral surfactant molecules. The main issue of the present chapter is thus to demonstrate whether or not the lyotropic SmC\* analog phase exhibits similar chirality effects as known from its thermotropic counterpart. The most outstanding manifestations of chirality in the thermotropic SmC\* phase are helicity, due to a chirality-induced precession of the director, and ferroelectricity, due to its polar  $C_2$ -point group symmetry. Thus, the focus of this chapter is on the detection and analysis of those two macroscopic chirality effects.

### 5.4.1 Investigation of the Helical Pitch

In samples which are substantially thicker than the helical pitch length, a helical director configuration can develop leading to a regularly striped texture (*cf.* Sects. 3.2.2 and 4.5.1). The observation of such a striped texture in planarly aligned samples already accounts for a macroscopic chirality of the phase and efforts were made to achieve this texture in the lyotropic SmC\* phase. Representative examples are shown in Fig. 5.32.

Figure 5.32a shows the striped texture of a sample of the diol C5O and water. The sample is quite thick, causing a multicolored, slightly blurry image. Nonetheless, the underlying periodic stripe pattern can be seen. The texture image thus confirms that the chirality-induced precession of the director along the layer normal  $\mathbf{k}$  is not suppressed by the layers of achiral solvent molecules. From the

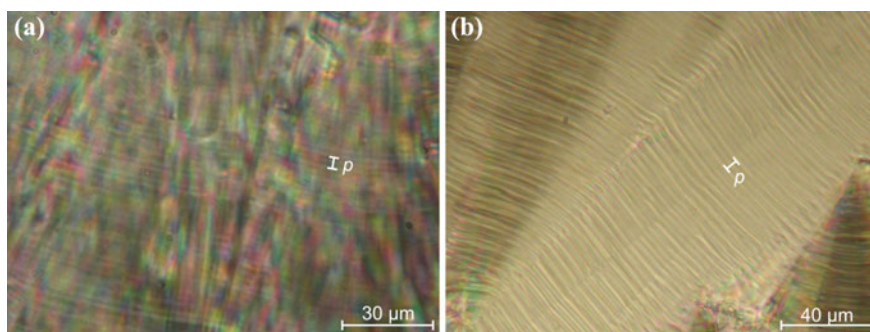


**Fig. 5.32** Striped texture of the lyotropic SmC\* analog phase in a sample of C5O with **a** 59 wt% of water at 36 °C and **b** 32 wt% of formamide at 30 °C. Due to the occurrence of unwinding lines, the pitch  $p$  corresponds to the distance between two stripes instead of only one (adapted from [20]. Copyright 2013 Wiley-VCH Verlag GmbH & Co. KGaA, Weinheim. Reproduced with permission.)



texture image a value of  $p = 4.7 \mu\text{m}$  can be deduced for the helical pitch length (*cf.* Sect. 4.5.1), which is in the same order of magnitude as typically found in thermotropic SmC\* phases [30–32].

In Fig. 5.32b the striped texture of the lyotropic SmC\* phase with formamide as solvent can be seen. The stripes appear much more visible in this sample, clearly indicating the macroscopic helicity of the lyotropic phase. The helical pitch of  $p = 5.2 \mu\text{m}$  is close to the value found in the mixture with water. However, there is one significant difference between the two solvents: While the sample with water had to rest for several weeks before the striped texture could be detected, the sample with formamide only took seconds after the transition into the lyotropic SmC\* analog phase to show the texture displayed in Fig. 5.32b. This difference in the time-based evolution of the helical director configuration is quite remarkable and implies that the solvent plays a very important part in the formation of the helix, even though it has only little impact on the absolute value of the helical pitch. Possible explanations might be the more extended solvent layer in the case of mixtures with water or a different internal structure in the solvent layer. However, these points are only speculations and the reason for the deviating behavior still has to be understood.

In further temperature and concentration-dependent measurements of the helical pitch, only mixtures with formamide were chosen as the lengthy evolution time necessary for mixtures with water together with the ever present threat of solvent evaporation make such investigations of mixtures with water much more complicated. In Fig. 5.33 the helical pitch  $p$  is plotted versus the reduced temperature  $T - T_C$  for a sample with 18 wt% of formamide. The pitch shows the typical temperature dependence known from thermotropic SmC\* phases [30]. Right after the phase transition into the lyotropic SmC\* analog phase, the pitch increases rapidly to a value of about  $5.5 \mu\text{m}$  and decreases more slowly towards a low temperature value of about  $2.5 \mu\text{m}$ . However, by repeating the measurement with other concentrations of formamide, no significant difference in the value of  $p$  could be detected.

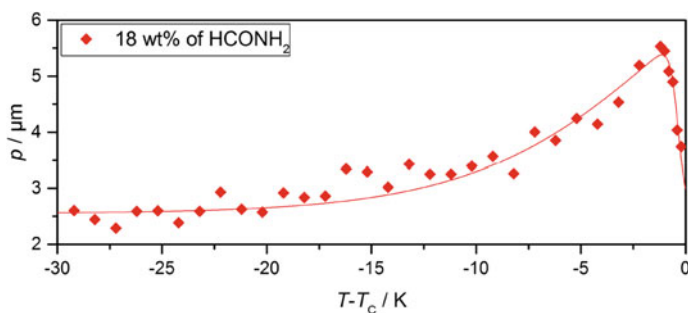


**Fig. 5.33** Temperature dependence of the helical pitch  $p$  measured with the ‘direct’ method in a  $30 \mu\text{m}$  thick sample of C5O with 18 wt% of formamide

The reason for this behavior can be found in the measuring conditions. The temperature-dependent measurement of the helical pitch was performed with the ‘direct’ method (*cf.* Sect. 4.5.1) in a sample of 30  $\mu\text{m}$  thickness. Apparently, in such rather thin samples compared to the value of the helical pitch, the formation of the helical director configuration cannot take place undisturbed, but is influenced significantly by interactions with the surfaces of the liquid crystal cell. Consequently, the observed value of  $p$  depends rather on the cell gap than on the intrinsic pitch of the lyotropic SmC\* analog phase. Nonetheless, the measurement in Fig. 5.33 indicate that the helical pitch of the lyotropic SmC\* analog phase varies with temperature and that the temperature dependence is comparable to the one of thermotropic SmC\* phases.

To avoid the influence of surface interactions on the measurement of the helical pitch length, two alterations of the experiment are possible. The first one is to enlarge the thickness of the sample significantly. The second is to measure the helical pitch length under homeotropic boundary conditions which are known to not affect its value [33]. Both methods, i.e. the ‘direct’ method (*cf.* Sect. 4.5.1) with samples of 250  $\mu\text{m}$  thickness and the Cano method (*cf.* Sect. 4.5.2), were applied to determine the influence of the solvent concentration on the helical pitch length.

In Fig. 5.34 examples of these measurements are shown. Figure 5.34a shows a Cano preparation between crossed polarizers. Circular defect lines can be found in the image, the so called Grandjean steps, which originate from a sudden integer raise in the number of helical windings (*cf.* Fig. 5.23a). According to Eq. 4.1 the helical pitch can be derived from the distances between the Grandjean steps. In Fig. 5.34b an image of the striped texture between crossed polarizers in a 250  $\mu\text{m}$  thick liquid crystal measurement cell is shown.

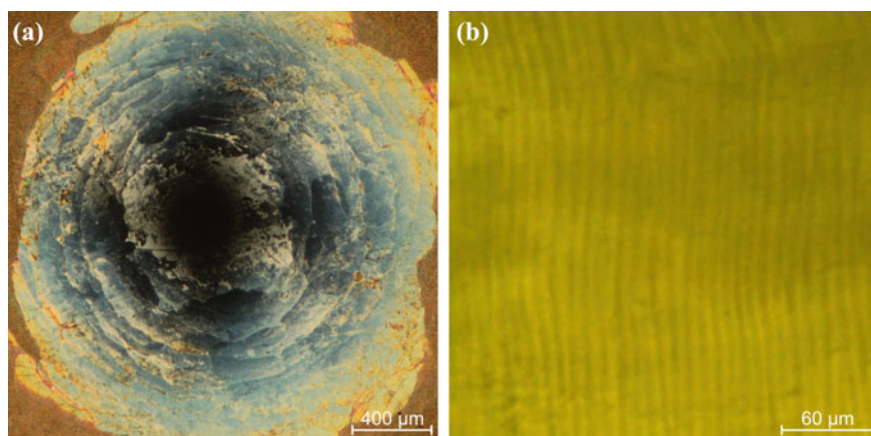


**Fig. 5.34** **a** Cano preparation of a mixture of C5O with 19 wt% of formamide at 29  $^{\circ}\text{C}$  exhibiting circular Grandjean steps. **b** Striped texture in a 250  $\mu\text{m}$  thick sample of C5O with 22 wt% of formamide at 5  $^{\circ}\text{C}$

The inverse of the pitch  $p^{-1}$ , which corresponds to the helical twist of the lamellas against each other, is plotted in Fig. 5.35 for different concentrations of formamide. The values shown in the upper part of Fig. 5.35 were determined with the Cano method, while the bottom part shows the results obtained by the ‘direct’ method. The two plots in Fig. 5.35 basically show the same behavior. In both plots no clear temperature dependence of the helical twist  $p^{-1}$  can be found. Right after the phase transition into the lyotropic SmC\* analog phase, the helical structure is

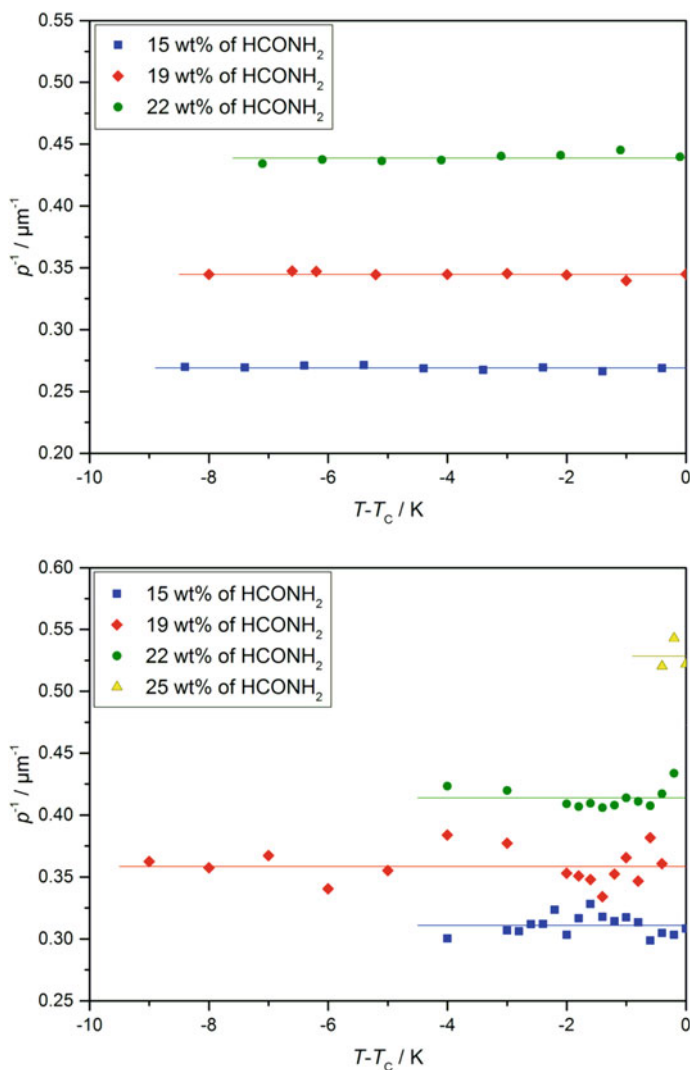


**Fig. 5.35** Helical twist  $p^{-1}$  in the lyotropic SmC\* phase for different ratios of C5O and formamide, determined with the Cano method (*top*) and with the ‘direct’ method (*bottom*)

only poorly developed and is therefore hardly observable. The measurements thus start somewhat below the actual phase transition (*cf.* Fig. 5.33). In the case of the ‘direct’ method, the experimental values scatter (Fig. 5.35, bottom). The reason for this scattering is the large sample thickness of 250  $\mu\text{m}$ , which does not allow any sharp focusing of the sample in the polarizing microscope, thus leading to considerable statistical errors in the pitch measurements. Nonetheless, the obtained values exhibit a similar behavior as the ones determined with the Cano method (*cf.* Fig. 5.35, top).

By looking at the concentration dependence of the helical twist in Fig. 5.35 an astonishing result is revealed. The helical twist  $p^{-1}$  increases with an increasing amount of formamide in the samples. This behavior is counter-intuitive if considering conventional liquid crystals. By increasing the amount of formamide, the number density of chiral diol molecules is reduced. Normally, this should lead to a decrease of the helical twist. This is true for lyotropic  $\text{N}^*$  phases [34–36] as well as for thermotropic  $\text{SmC}^*$  phases [37–39], regarding the solvent concentration or the concentration of a chiral dopant, respectively. Only one publication by Maxein et al. [40] describes a comparable behavior of the cholesteric pitch in styrene solutions of chiral polyisocyanate terpolymers. In this publication the pitch passes through a minimum at about 43 wt% of solvent. By decreasing the solvent concentration, the pitch starts to increase, which is equivalent to a decrease of the helical twist. The authors however do not give an explanation for the unexpected behavior. A possible explanation for the unexpected behavior of an increasing helical twist in the lyo- $\text{SmC}^*$  phase at increasing solvent concentration might be a competition between the chiral twisting power, which decreases with increasing solvent concentration, and the elasticity which might permit easier twisting at increasing thickness of the solvent layer.

Summing up, the decrease of the pitch  $p$  with increasing solvent concentration and thus a decreasing concentration of chiral molecules is a notable difference between the lyotropic  $\text{SmC}^*$  analog phase and conventional thermotropic  $\text{SmC}^*$  phases. Furthermore, the behavior of the lyotropic  $\text{SmC}^*$  analog pitch provides an easy way to adjust it by simply adding or evaporating solvent. This uncomplicated way of tuning the helical pitch might turn out to be a useful feature for future applications.

### 5.4.2 *Electro-optical Investigations*

Ferroelectricity in  $\text{SmC}^*$  liquid crystals is directly observed in the surface-stabilized state in which macroscopic domains of opposite tilt direction are connected to opposite directions of the spontaneous polarization (*cf.* Sect. 1.2). An electric field-induced reversal of the direction of spontaneous polarization also reverses the direction of tilt and thus leads to a polar bistable electro-optic response. In thermotropic  $\text{SmC}^*$  liquid crystals this unique combination of a fluid ferroelectric material was and is extensively studied.

Since a lyotropic lamellar phase with tilted and chiral molecules has the same polar  $C_2$  point group symmetry as the thermotropic SmC\* phase, the important question emerges, whether the lyotropic SmC\* phase might also show ferroelectricity and polar electro-optic switching like its thermotropic counterpart.

In order to prepare a surface-stabilized lyo-SmC\* sample, C5O/formamide mixtures with a mass fraction of 19 wt% of formamide were filled into thin nylon coated cells of 1.6  $\mu\text{m}$  cell gap by the suction method (*cf.* Sect. 4.4). Since the cell gap is considerably smaller than the helical pitch length of several micrometers the formation of the helical structure is suppressed and instead of the striped texture a typical domain texture as shown in Fig. 5.36 with separate domains of opposite tilt directions is observed.

By applying an alternating electric field to this sample, the texture observed between crossed polarizers changes in dependence of the direction of the applied electric field as shown in Fig. 5.36a, b. This observation already suggests a polar response of the lyo-SmC\* phase to the electric field. However, full switching as known from thermotropic SmC\* phases cannot be observed due to the low resistance of the lyotropic SmC\* analog phase which leads to very high induced currents and thus to a dielectric break down of the measurement cell at high voltages or low frequencies of the applied electric field.

To definitely prove, that this effect is indeed polar and not dielectric, the transmission of the sample between crossed polarizers was recorded with a photomultiplier. The signal obtained (dots) is plotted in the upper part of Fig. 5.37 together with the electric field applied (line). The graph plainly validates that the change in transmission observed is polarity-dependent, as the direction of the recorded intensity reverses whenever the direction of the applied electric field

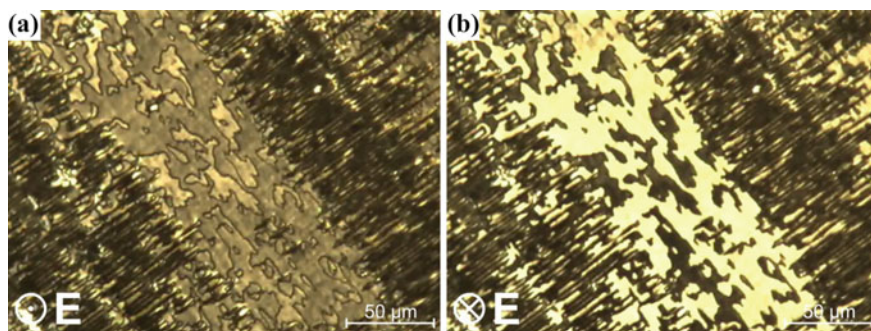


**Fig. 5.36** Electro-optic investigations of the lyotropic SmC\* analog phase. **a** and **b** Show the texture between crossed polarizers of a 1.6  $\mu\text{m}$  thick sample of C5O with 19 wt% of formamide in a nylon coated, single-side rubbed measurement cell. An alternating electric field with a frequency of 0.5 Hz and a voltage of  $5 \text{ V } \mu\text{m}^{-1}$  was applied to the measurement cell. The two images were taken at the same position in the sample but at reversed directions of the applied field. The change in transmission and thus in the orientation of the director can clearly be seen, yet no full switching of the director is achieved (adapted from [19]. Copyright 2013 Wiley-VCH Verlag GmbH & Co. KGaA, Weinheim. Reproduced with permission.)

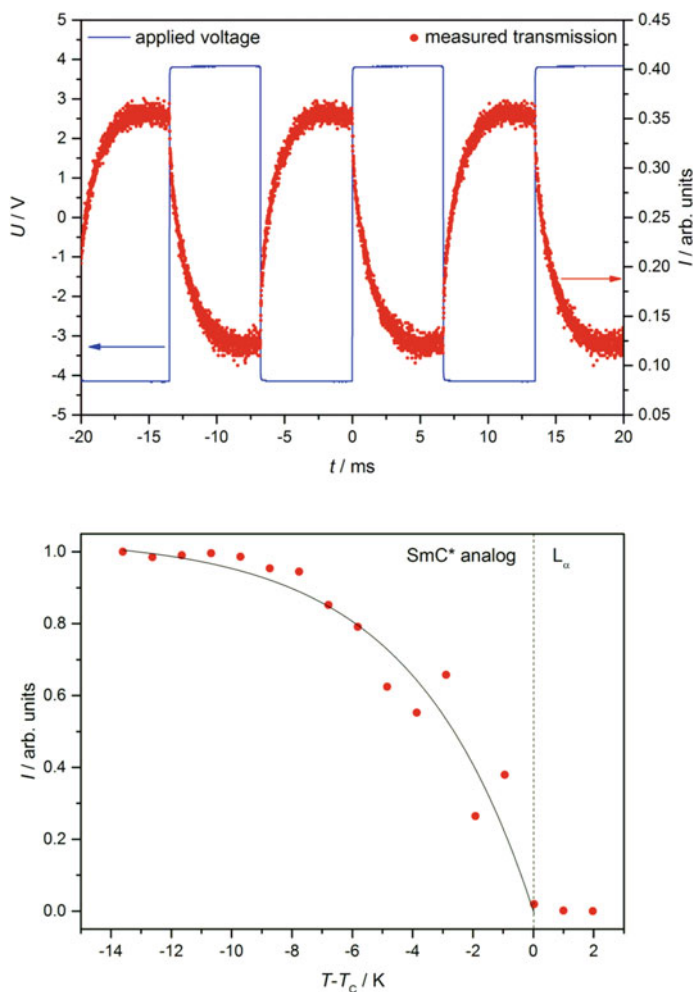


**Fig. 5.37** Change in transmission of the texture of the lyotropic SmC\* analog phase between crossed polarizers induced by an alternating electric field of 73 Hz. In the *upper part* of the figure the intensity  $I$  of the transmission (*dots*) is plotted together with the applied voltage  $U$  (*line*), whereas in the *bottom* the intensity measured is plotted versus the relative temperature  $T - T_C$  (adapted from [20]. Copyright 2013 Wiley-VCH Verlag GmbH & Co. KGaA, Weinheim. Reproduced with permission.)

changes. Thus, the lyotropic SmC\* analog phase shows polar switching in analogy to the thermotropic ferroelectric SmC\* phase.

By integrating the transmission intensity measured and plotting it versus the reduced temperature, the graph at the bottom of Fig. 5.37 is obtained. The measurement starts in the lamellar  $L_\alpha$  phase. Here, no effect of the electric field applied on the sample can be observed and thus the change in the transmission measured is

zero. By cooling down into the lyotropic SmC\* analog phase the signal measured starts to increase. At first the increase of the intensity change is quite rapid, but then the values start to flatten out and at a reduced temperature of  $T - T_C = -10$  K a more or less saturated state seems to be reached.

After proving that the lyotropic SmC\* analog phase is indeed ferroelectric, the next logical step is to determine the value of its spontaneous electric polarization. In thermotropic SmC\* phases the value of  $P_S$  is usually measured by means of the triangular wave method (*cf.* Sect. 4.6.1). However, first experiments on the lyotropic SmC\* analog phase showed that this method is not applicable for lyotropic liquid crystals. Due to the solvent and ionic impurities dissolved therein, the conductivity of lyotropic liquid crystals is rather high compared to thermotropic liquid crystals. Therefore, the resistance becomes very small leading to a quite big ohmic current which is about 100 times larger than in similar experiments with thermotropic SmC\* liquid crystals. It turned out to be nearly impossible to measure the spontaneous electric polarization in the lyotropic SmC\* analog phase with the triangular wave method, since the spontaneous polarization current is almost completely hidden by the large ohmic current.

In a second approach to determine the contribution of the spontaneous electric polarization to the total current, an experimental set-up was devised which simulates all other contributions to the induced current by an equivalent circuit. This set-up is referred to as compensation circuit, as the subtraction of the simulated signal from the measured signal compensates all irrelevant contributions. A sketch of this set-up is shown in Fig. 5.38. The resistance of the lyotropic liquid crystals was simulated with an adjustable resistor which is connected in parallel to an adjustable capacitor mimicking the capacity of the measurement cell. In addition, the resistance  $R_{ITO}$  of the ITO layer has to be taken into account due to the small resistance of the lyotropic liquid crystal. In contrast to the other contributions to the total current, the resistance of the ITO layer has to be seen as connected in series. By subtracting the two signals only the contribution of the spontaneous electric polarization  $P_S$  to the total current should be left. As there are three adjustable

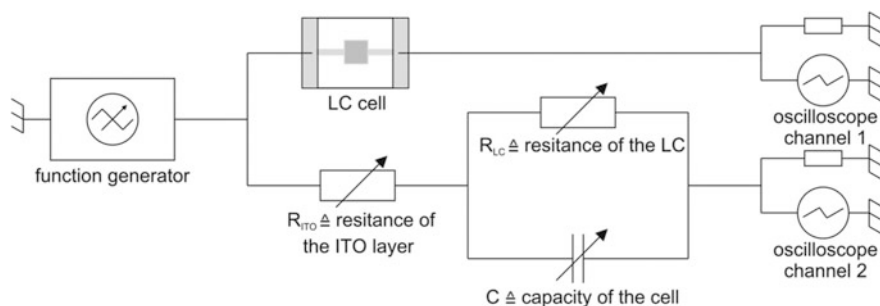


**Fig. 5.38** Measurement set-up for detecting the spontaneous electrical polarization  $P_S$ . The compensation circuit composed of two adjustable resistors and a capacitor mimics the current in the cell filled with the lyotropic SmC\* analog phase



variables ( $R_{LC}$ ,  $R_{ITO}$ ,  $C$ ) in this set-up, the obtained results are not very reliable. However, with this method it is at least possible to detect an additional current which might be related to the spontaneous polarization reversal in the lyotropic SmC\* analog phase.

In Fig. 5.39 the measured as well as the simulated signals are plotted. The upper part of Fig. 5.39 shows the current measured in the lamellar  $L_\alpha$  phase (red curve) and the according simulated signal (black curve). In the examined region the two

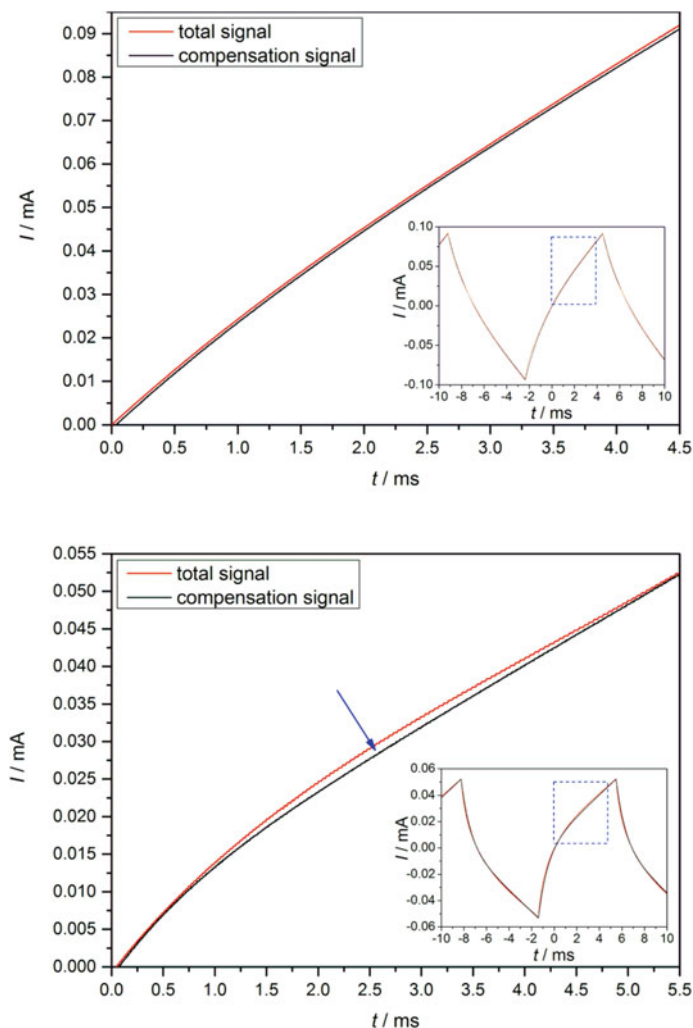


**Fig. 5.39** Current response to a triangular voltage of  $5 \text{ V } \mu\text{m}^{-1}$  at a frequency of 73 Hz applied to the compensation circuit (black curves) and to a C50/formamide sample with 19 wt% of formamide (red curves) in the lamellar  $L_\alpha$  phase at 36 °C (top) and the lyotropic SmC\* analog phase at 16 °C (bottom)



curves exhibit the same progression as there is no contribution in the lamellar  $L_\alpha$  phase to the reversal current which is not covered by the compensation circuit. In the lower part of Fig. 5.39 the measurement in the lyotropic analog of the SmC\* phase is shown. Here, a slight deviation between the measured curve and the simulated curve can be found, which cannot be compensated with the used equivalent circuit.

Hence, the measurement shows that an additional current is observed in the lyotropic SmC\* analog phase, which is not the case in the lamellar  $L_\alpha$  phase. This additional contribution to the total current might originate from the spontaneous electric polarization reversal in the lyo-SmC\* phase. However, the measurement also reveals how small this additional current is compared to the overall current.

For enhanced visibility of the additional polarization reversal current, the simulated curve is subtracted from the measured curve. The resulting compensated signal is plotted in Fig. 5.40 for different temperatures. The contributions which might be attributed to the spontaneous electric polarization are marked arrows. At higher temperatures the curve of the compensated signal runs flat in the examined region. By going to lower temperatures the marked maxima and minima become more and more pronounced. Hence, the additional polarization reversal current increases, according to an increasing spontaneous electric polarization with decreasing temperature, as expected for the lyotropic analog of the SmC\* phase.

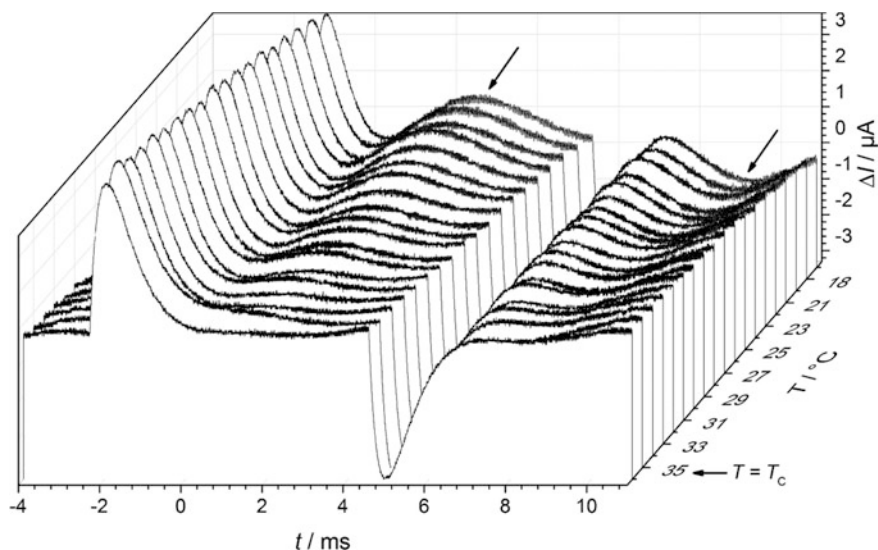


**Fig. 5.40** Compensated measurement signal of a C50 sample with approximately 19 wt% of formamide for different temperatures. The polarization reversal current which can be assigned to the spontaneous electric polarization reversal is marked with an *arrow*. The peak-like maxima or minima do not change with temperature. Thus, they do not correlate with the spontaneous electric polarization but are due to some uncompensated contribution

Next to the additional current just discussed, a further uncompensated current can be found in Fig. 5.40 manifesting in a rather sharp maximum and minimum. However, this uncompensated current also appears in the lamellar  $L_\alpha$  phase and its amplitude does not change with temperature. Therefore, it cannot be attributed to the spontaneous electric polarization of the lyotropic SmC\* analog phase. Most likely, this uncompensated current is due to some disregarded contribution or imprecision in the set-up of the compensation circuit.

In principle, the value of the spontaneous electric polarization  $P_S$  might be derived from Fig. 5.40 and calculated with Eq. 4.2. However, repeated measurements show that the absolute value of  $P_S$  is irreproducible with this method. Thus, no absolute value for the spontaneous electric polarization  $P_S$  will be given in this context. Nonetheless, the measurement proved to be a valuable tool in verifying the appearance of an additional polarization reversal current possibly due to the spontaneous electric polarization  $P_S$  in the lyotropic SmC\* analog phase.

The third approach which was made to determine the value of the spontaneous electric polarization  $P_S$  in the lyotropic analog of the SmC\* phase makes use of its correlation with the time  $\tau$ , which is necessary for switching between the two surface-stabilized states, and with the applied electric field  $E$  (*cf.* Sect. 4.6.2). In Fig. 5.41 the measured switching time  $\tau_{10-90}$  is plotted versus the inverse amplitude  $E^{-1}$  of the applied electric field. Below the threshold voltage the switching of the director between the two surface-stabilized states is incomplete. At field amplitudes higher than the threshold field a linear dependence of the switching time  $\tau_{10-90}$  and the inverse electric field  $E^{-1}$  emerges. According to Eq. 4.3 the slope  $m$  of the

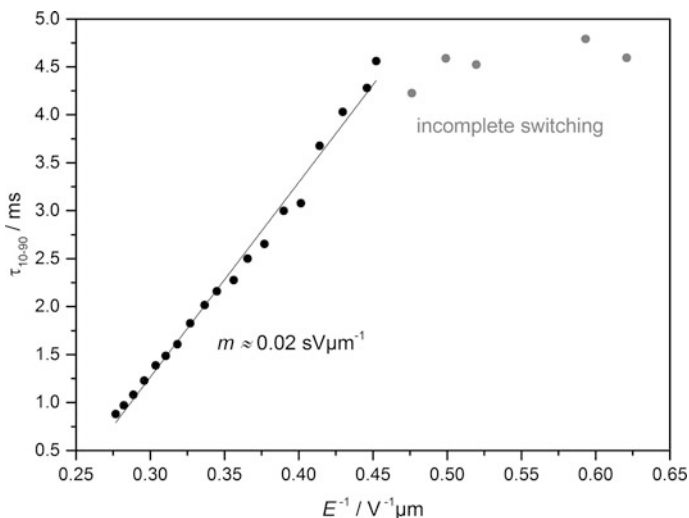


**Fig. 5.41** Switching time  $\tau_{10-90}$  versus the inverse of the applied electric field  $E^{-1}$  measured in a sample of C5O with 20 wt% of formamide at 25 °C. The *gray data points* mark a region in which the applied electric field is too small to induce sufficient switching of the molecules

regression line is proportional to  $\gamma_\phi/P_S$ . Unfortunately, the rotational viscosity  $\gamma_\phi$  is unknown and its measurement would require a large amount of the sample. However, a rough estimation of  $P_S$  can be made by assuming that the order of magnitude of the viscosity in general depends on the state of matter and the temperature mainly. Typical values for the viscosity  $\gamma$  of lyotropic lamellar  $L_\alpha$  phases determined by microrheology at 25 °C were found to be in the order of 10–20 mPa s [41–43]. Inserting this value into Eq. 4.3 results in a spontaneous polarization of 0.1–0.2 nC cm<sup>-2</sup>. Even though this is a very rough estimation, the comparatively small spontaneous electric polarization seems reasonable considering the difficulties which occurred on trying to measure it.

## 5.5 Model of the Lyotropic SmC\* Analog Phase

Based on the measurements presented in the preceding chapters, several conclusions can be drawn concerning the structure of the lyotropic SmC\* analog phase. The observations and corresponding conclusions are as follows:

- Sharp (00*l*)-layer peaks of 1st and 2nd order indicate a one dimensional periodic lamellar structure.
- Diffuse scattering in the wide-angle regime show that the investigated phase is fluid.
- An almost linear increase of the layer spacing measured with X-ray diffraction suggests the presence of separate solvent and surfactant layers.
- A surfactant layer thickness larger than the calculated molecular length hints on the formation of bilayers.
- The macroscopic tilt angles detected optically and by X-ray diffraction indicate that the surfactant molecules are tilted inside the bilayers and that the tilt direction is intra- and interlamellarly correlated over a long distance.

On the basis of these observations it is possible to devise a structural model of the lyotropic SmC\* analog. However, chirality effects are not included in this model and it is thus also applicable to the achiral lyo-SmC phase.

In Fig. 5.42 a true to scale sketch of this structural model is shown, which is consistent with the results obtained for the sample of C5O with 19 wt% of formamide at a temperature relative to the phase transition of  $T - T_C = -10$  K. The repeat unit of the lamellar structure is composed of two parts: a bilayer of the C5O diol molecules and a solvent layer of formamide. By taking into account the extrapolated values of the bilayer thickness in Fig. 5.27 and the calculated length of the diol molecule of 2.49 nm, it turns out that the hydrophobic parts of the diol molecules have to interdigitate considerably. Furthermore, the diol molecules within the partial bilayers are tilted with respect to the layer normal  $\mathbf{k}$  (*cf.* Fig. 5.28). The formamide layer is composed of more or less disordered solvent molecules, which are depicted as gray dots in Fig. 5.42. By extrapolating the layer spacing (*cf.* Fig. 5.25) towards the borders of the concentration range in which the lyotropic SmC\* phase exists, a minimum

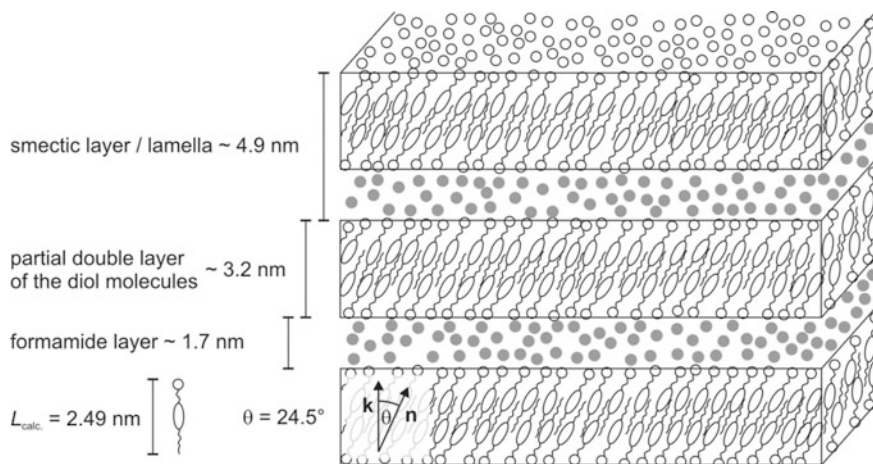


**Fig. 5.42** Structural model of the lyotropic SmC\* analog phase based on the presented measurements of the C50 sample with 19 wt% of formamide at  $T - T_C = -10 \text{ K}$

formamide layer thickness of about 0.7 nm and a maximum formamide layer thickness of about 2.7 nm can be expected. If the thickness of the solvent layer is increased further, only the lamellar  $L_\alpha$  phase remains.

The maximum thickness of the formamide layer of 2.7 nm is only slightly higher than the length of the C50 molecule of 2.49 nm. Thus, one might think that the stability of the lyotropic SmC\* analog phase is based on out of layer fluctuations, which cannot take place if the solvent layer is significantly larger than the length of the molecule. This idea conflicts with measurements performed on mixtures of C50 and water. Here a smectic layer spacing of up to 7 nm at the lamellar  $L_\alpha$  to lyo-SmC\* phase transition was measured in a sample with 64 wt% of water. Assuming that the structure of the bilayers of the diol molecules does not depend on the solvent used, this leads to a solvent layer thickness of 3.4 nm, which is significantly larger than the molecular length.

In conclusion, the model shown in Fig. 5.42 provides an experimentally validated picture of the structure of the lyo-SmC\* phase. However, it does not answer how the correlation of the director tilt takes place from one bilayer to the next across the intermediating layers of solvent molecules. Furthermore, it does not explain how the chirality-induced subtle precession of the director is transmitted, which corresponds to only  $0.2^\circ$  per lamella in the example shown. Thus, to address these two issues further considerations have to be taken into account.

In Sect. 5.1.2 it was shown, that two things are necessary for the formation of the lyotropic analog of the SmC\* phase. Firstly, the surfactant molecule has to exhibit a very balanced structure inbetween the structure of conventional thermotropic and lyotropic liquid crystals. Especially, the lyotropic part has to incorporate a polar chain with oxygen atoms connecting the diol head group to the rest of the molecule. Secondly, the solvent has to possess at least two hydrogen bond donor atoms

allowing the formation of up to four hydrogen bonds per molecule. The solvent molecules are thus able to build up a network of hydrogen bonds. Hence, it seems that the key to understanding the long-range correlation of tilt direction as well as its helical precession in the lyotropic SmC\* analog phase is a pronounced hydrogen bond network between the solvent molecules as well as between the solvent and the surfactant molecules. Based on this observation, the structural model of the lyo-SmC\* phase was refined as discussed in the following.

In Fig. 5.43 the two-dimensional projection of a possible molecular arrangement in the lyotropic analog SmC\* analog phase is shown.<sup>7</sup> The hydrophobic parts of the C5O diol molecules, i.e. the alkyl chains and the aromatic cores, are highlighted in red. The alkyl chains of the diol molecules interdigitate, thus building up the backbone of the bilayer. The hydrophilic parts of the diol molecules, which include the diol head groups as well as the ethylene glycol units, are marked in purple. Since the ethylene glycol units are hydrophilic, solvent molecules can penetrate into this region of the bilayers. The core axes of the diol molecules are tilted with respect to the layer normal. The directions and the magnitude of this tilting are sustained in every bilayer. The region between two bilayers is filled with further formamide molecules. The formamide molecules form a very dense hydrogen bond network with up to four hydrogen bonds per solvent molecule [44, 45]. To gain an impression how this hydrogen bond network could look like, the molecular arrangement in Fig. 5.43 assumes that the structure and connectivity of the hydrogen bond network in liquid formamide is similar but less ordered than its structure in crystalline formamide [46]. The picture suggests that there are not only multiple hydrogen bonds between the solvent molecules but also between the diol head groups of the C5O molecules and the formamide molecules. Moreover, the formamide molecules which interpenetrate into the bilayers form hydrogen bonds with the oxygen atoms of the ethylene glycol units. In consideration of this molecular arrangement, the picture of a complex and tightly interwoven structure emerges. In conclusion, the model suggests, that the long-range inter-layer correlation of tilt directions takes place via this very strong and dense hydrogen bond network.

This assumption is experimentally supported by several results presented earlier in this thesis:

- Firstly, the stability of the lyotropic SmC\* analog phase (in temperature and concentration range) is higher with water than with formamide as solvent (*cf.* Sect. 5.2.1). In comparison no lyo-SmC\* phase is formed with *N*-methylformamide (*cf.* Sect. 5.2.2). These observations are in line with the assumption that the correlation of the tilt direction takes place via the hydrogen bond network if considering that the number density of hydrogen bond donor atoms in water is twice as big as in formamide and that *N*-methylformamide is not capable of forming a hydrogen bond network (*cf.* Table 5.2).

---

<sup>7</sup>The depicted sketch corresponds to a sample of C5O with 20 wt% of formamide in scale and concentration, if the number of surfactant molecules is doubled. Half of the surfactant molecules were omitted for sake of clarity.

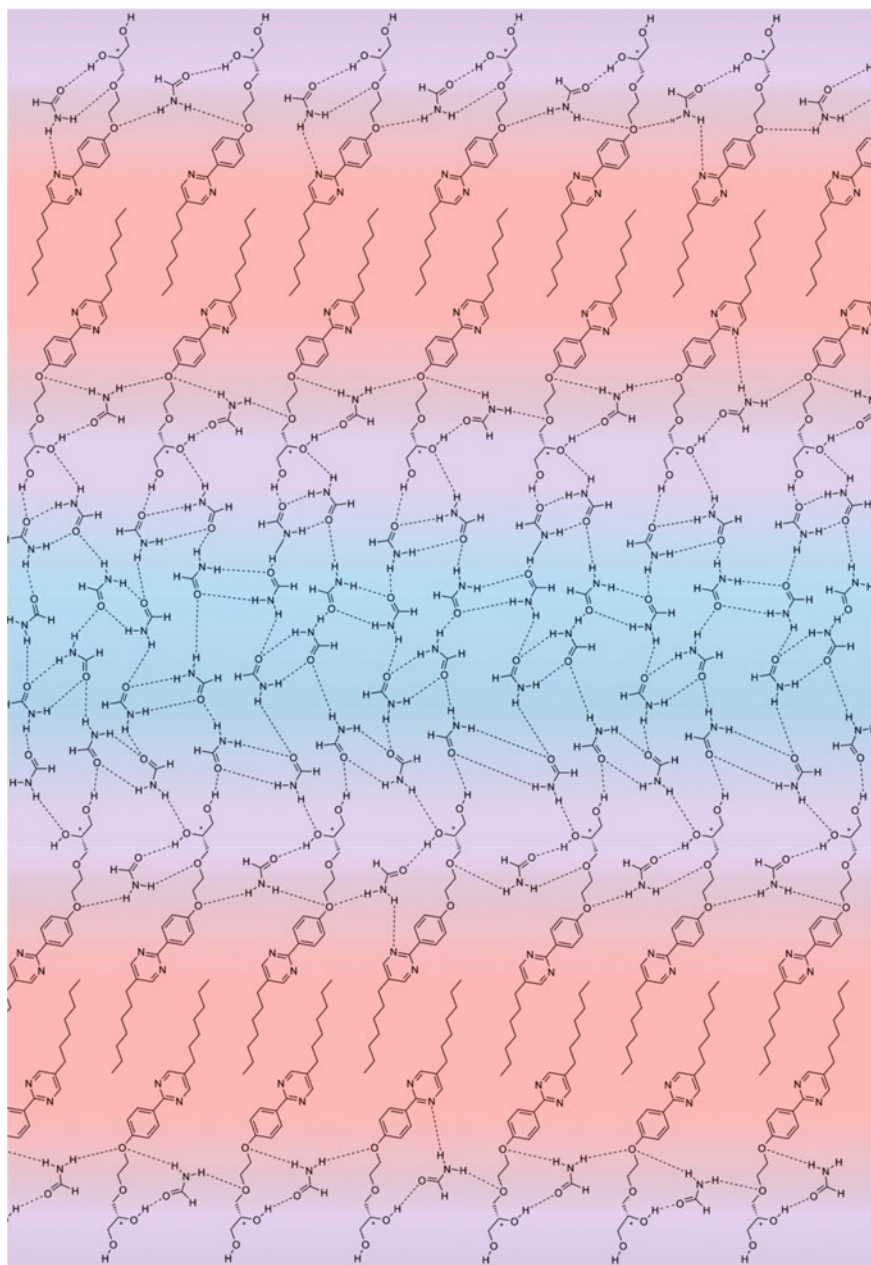


**Fig. 5.43** Refined model of the lyotropic SmC\* analog phase. The hydrophobic part of the bilayers is highlighted in *red*, the hydrophilic part in *purple* and the formamide layer in *blue* (adapted from [17]. Copyright 2015 Wiley-VCH Verlag GmbH & Co. KGaA. Reproduced with permission.)



- Secondly, a rigid hydrogen bond network should improve the correlation of the tilt directions from one layer to the next. This rigidity should be influenced by the number density of the hydrogen bonds as well as the length of the hydrogen bond connection between the bilayers. Thus, if the thickness of the solvent layer is increased, the total rigidity of the hydrogen bond network decreases. This is in line with the experimental observation that the optically determined tilt angle  $\theta_{\text{opt}}$  decreases with increasing solvent concentration while the tilt angle  $\theta_{\text{steric}}$  deduced from X-ray measurements does not. This suggests that the correlation of the tilt direction from one layer to the next is reduced by the increasing thickness of the solvent layers. Furthermore, this is also in agreement with an increasing helical twist  $p^{-1}$  with increasing solvent concentration, as a reduced rigidity of the hydrogen bond network should facilitate the twist of the hydrogen bond network.
- Finally, in the case of formamide as solvent, the phase transition temperature of the lamellar  $L_{\alpha}$  to lyotropic SmC\* analog phase transition shifts to smaller and smaller values with increasing formamide concentration (*cf.* Sect. 5.2.1). This accounts for a loss of correlation between the partial bilayers with increasing thickness of the solvent layer. After reaching a critical formamide layer thickness of 2.7 nm all correlation is lost as the hydrogen bond network becomes less rigid.

In conclusion, the refined model points out the importance of a densely woven three-dimensional hydrogen bond network for the long-range interlamellar correlation of the tilt directions which is necessary for the formation of the lyotropic SmC\* analog phase. Moreover, it is consistent with the experimental results presented in this thesis. Some questions however remain unclear. Especially, the issue of how the transfer of chirality along the hydrogen bond network takes places on a molecular scale. Summing up, this thesis lays the foundation for understanding the novel lyotropic analog of the thermotropic SmC\* phase and opens a fascinating new field in liquid crystal research.

## References

1. N. Pietschmann, A. Lunow, G. Brezesinski, C. Tschierske, F. Kuschel, H. Zschke, *Colloid Polym. Sci.* **269**, 636–639 (1991)
2. L. Li, C.D. Jones, J. Magolana, R.P. Lemieux, *J. Mater. Chem.* **17**, 2313–2318 (2007)
3. J.C. Roberts, N. Kapernaum, F. Giesselmann, R.P. Lemieux, *J. Am. Chem. Soc.* **130**, 13842–13843 (2008)
4. C. Tschierske, A. Lunow, D. Joachimi, F. Hentrich, D. Gridziunaite, H. Zschke, A. Mädicke, G. Brezesinski, F. Kuschel, *Liq. Cryst.* **9**, 821–829 (1991)
5. M. Kçlbel, T. Beyersdorff, C. Tschierske, S. Diele, J. Kain, *Chem. Eur. J.* **12**, 3821–3837 (2006)
6. J.R. Bruckner, *Struktur und Chiralitätseffekte in lyotrop-flüssigkristallinen Phasen eines chiralen 1,2-Diols*. Diploma thesis, University of Stuttgart, 2010
7. J.R. Bruckner, D. Krueerke, J.H. Porada, S. Jagiella, D. Blunk, F. Giesselmann, *J. Mater. Chem.* **22**, 18198–18203 (2012)

8. M.A. Schafheutle, H. Finkelmann, *Liq. Cryst.* **3**(10), 1369–1386 (1988)
9. S. Ujiie, Y. Yano, *Chem. Commun.* 79–80 (2000)
10. M. Barón et al., *Pure Appl. Chem.* **73**(5), 845–895 (2001)
11. B. Neumann, C. Sauer, S. Diele, C. Tschierske, *J. Mater. Chem.* **6**(7), 1087–1098 (1996)
12. N. Lindner, M. Kölbl, C. Sauer, S. Diele, J. Jokiranta, C. Tschierske, *J. Phys. Chem. B* **102**, 5261–5273 (1998)
13. A. Lattes, E. Perez, I. Rico-Lattes, *C. R. Chimie* **12**, 45–53 (2009)
14. Sigma-Aldrich, *Material Safety Data Sheet*, [www.sigmaaldrich.com](http://www.sigmaaldrich.com) (2014)
15. W.M. Haynes, T.J. Bruno, D.R. Lide, *CRC Handbook of Chemistry and Physics*, 95th edn. Internet Version 2015 (CRC Press, Taylor and Francis Group, 2014)
16. Merck Millipore, *Material Safety Data Sheet*, [www.merckmillipore.com](http://www.merckmillipore.com) (2014)
17. J.R. Bruckner, F. Knecht, F. Giesselmann, Origin of the director tilt in the lyotropic smectic C\* analog phase: hydration interactions and solvent variations. *ChemPhysChem*, doi:[10.1002/cphc.201500673](https://doi.org/10.1002/cphc.201500673)
18. K. Dimroth, C. Reichardt, T. Siepmann, F. Bohlmann, *Liebigs Ann. Chem.* **661**, 1–37 (1963)
19. G.W. Gray, J.W.G. Goodby, *Smectic Liquid Crystals—Textures and Structures* (Leonard Hill, Glasgow and London, 1984)
20. J.R. Bruckner, J.H. Porada, C.F. Dietrich, I. Dierking, F. Giesselmann, *Angew. Chem. Int. Ed.* **52**, 8934–8937 (2013)
21. N.A. Clark, T.P. Rieker, J.E. MacLennan, *Ferroelectrics* **85**(1), 79–97 (1988)
22. C. Giacobozzo, H.L. Monaco, G. Artioli, D. Viterbo, M. Milanese, G. Ferraris, G. Gilli, P. Gilli, G. Zanotti, M. Catti, in *Fundamentals of Crystallography*, 3rd ed. by C. Giacobozzo (Oxford University Press, New York, 2011)
23. R.D. Kamien, T.C. Lubensky, *J. Phys. II* **7**, 157–163 (1997)
24. J.W. Goodby, M.A. Waugh, S.M. Stein, E. Chin, R. Pindak, J.S. Patel, *J. Am. Chem. Soc.* **111**, 8119–8125 (1989)
25. J.W. Goodby, M.A. Waugh, S.M. Stein, E. Chin, R. Pindak, J.S. Patel, *Nature* **337**, 449–452 (1989)
26. S.R. Renn, T.C. Lubensky, *Phys. Rev. A* **38**(4), 2132–2147 (1988)
27. I. Dierking, *Liq. Cryst.* **26**(1), 83–95 (2010)
28. E. Fontes, P.A. Heiney, J.L. Haseltine, A.B. Smith, *J. Phys.* **47**, 1533–1539 (1986)
29. D. Nonnenmacher, *Struktur-Eigenschaftsbeziehungen in smektischen Flüssigkristallen vom de Vries-Typ*. Doctoral thesis, University of Stuttgart, 2014
30. P. Martinot-Lagarde, *J. Phys. Colloques* **37**, C3-129–C3-132 (1976)
31. K. Kondo, H. Takezoe, A. Fukuda, E. Kuze, *Jpn. J. Appl. Phys.* **21**(2), 224–229 (1982)
32. M. Krueger, F. Giesselmann, *J. Appl. Phys.* **101**, 094012-1–094012-8 (2007)
33. W. Kuczyński, *Phys. Rev. E* **81**, 021708-1–021708-6 (2010)
34. F. Fried, J.M. Gill, P. Sixou, *Mol. Cryst. Liq. Cryst.* **98**, 209–221 (1983)
35. B.R. Harkness, D.G. Gray, *Macromolecules* **23**(5), 1452–1457 (1990)
36. J. Partyka, K. Hiltrop, *Liq. Cryst.* **20**(5), 611–618 (1996)
37. H. Stegemeyer, H.-J. Kersting, W. Kuczynski, *Ber. Bunsenges. Phys. Chem.* **91**, 3–7 (1987)
38. H.-R. Dübal, C. Escher, D. Ohlendorf, *Ferroelectrics* **84**, 143–165 (1988)
39. S.-Y.T. Tzeng, C.-N. Chen, Y. Tzeng, *Liq. Cryst.* **37**(9), 1221–1224 (2010)
40. G. Maxein, S. Mayer, R. Zentel, *Macromolecules* **32**, 5747–5754 (1999)
41. Q. Liu, T. Asavei, T. Lee, H. Rubinsztein-Dunlop, S. He, I.I. Smalyukh, *Opt. Express* **19**(25), 24143–25135 (2011)
42. Y. Kimura, D. Mizuno, *Mol. Cryst. Liq. Cryst.* **478**, 759–769 (2007)
43. N. Yamamoto, M. Ichikawa, Y. Kimura, *Phys. Rev. E* **82**, 021506-1–021506-8 (2010)
44. E. Kálmán, I. Serke, G. Pálinkás, M.D. Zeidler, F.J. Wiesmann, H. Bertagnolli, P. Chieux, *Z. Naturforsch.* **38a**, 231–236 (1983)
45. I. Bakó, T. Megyes, S. Bálint, V. Chihaia, M.-C. Bellissent-Funel, H. Krienke, A. Kopf, S.-H. Suh, *J. Chem. Phys.* **132**, 014506-1–014506-7 (2010)
46. S. Suhai, *J. Chem. Phys.* **103**(16), 7030–7039 (1995)



## Chapter 6

### Summary

The subject of this thesis is the discovery and characterization of the lyotropic analog of the well-known thermotropic ferroelectric SmC\* liquid crystal phase. In addition to providing evidence for the existence of this previously unknown phase, the main focus of the work presented is on the investigation of its structural properties and chirality effects. In particular, the following results were obtained:

- The systematic study of the schematic phase diagrams of various surfactant/solvent systems indicates that certain structural elements are required for the formation of the lyotropic SmC\* analog phase. In addition to a SmC\*-promoting aromatic core and a hydrogen-bonding head group, the presence of an ethylene glycol unit linking those two elements seems to be crucial for the surfactant molecule. The overall design of the surfactant molecule is very delicate, as small variations of the structure lead to the disappearance of the lyotropic SmC\* analog phase. Out of the investigated surfactant molecules only one exhibits the lyotropic SmC\* analog phase and was thus selected for further investigations. The solvent molecules should be highly polar, possess a small molecular volume and be able to form multiple hydrogen bonds leading to a dense three-dimensional hydrogen bond network. Only water and formamide have proved to be suitable solvents so far.
- The detailed phase diagrams of the selected surfactant with water or formamide exhibit a variety of lyotropic liquid crystalline phases. While there is only a monotropic cholesteric phase in the neat surfactant, the addition of either one of the solvents leads to the induction of the following enantiotropic phases: cholesteric, lamellar  $L_{\alpha}$ , high and low temperature two-dimensional monoclinic  $M_{\alpha}$ , and SmC\* analog. Remarkably, the lyotropic SmC\* analog phase occurs only at elevated solvent concentrations, which shows that this is a true lyotropic phase.
- The SmC\* analog nature of the lyotropic phase was demonstrated by the observation of characteristic textures associated with the thermotropic SmC\* phase, such as broken fan-shaped texture, schlieren texture, zigzag defects, spontaneous tilt domains in the surface-stabilized state and pitch lines. Further evidence was provided by X-ray experiments. The two-dimensional diffraction pattern of an aligned sample confirms that the phase is lamellar, tilted and fluid,

and the layer spacing shows a temperature dependence typical of thermotropic SmA\* to SmC\* phase transitions.

- Temperature-dependent X-ray diffraction measurements of the layer spacing of the lyotropic SmC\* analog phase in mixtures with different concentrations of formamide revealed that the layer spacing increases approximately linearly with the amount of solvent. The maximum solvent layer thickness which still allows the correlation of the director tilt direction between succeeding surfactant layers, was estimated to be about 2.7 nm.
- The optically measured tilt angle of mixtures with formamide can be as large as 28°. The magnitude of the tilt angle decreases with increasing solvent concentration. This can be explained by the increased solvent layer thickness which leads to a reduced inter-lamellar tilt correlation. Measurements of the temperature dependence of the tilt angle showed that an increasing solvent concentration drives the lamellar  $L_\alpha$  to SmC\* analog phase transition from first to second order, a trend that was also confirmed by differential scanning calorimetry.
- A significant result of this thesis is that the subtle chirality-induced helical precession of the tilt direction is correlated over long distance, even though the surfactant bilayers are separated by substantial layers of achiral solvent molecules. To gain further insight into this phenomenon, two chirality effects of the lyotropic SmC\* analog phase were studied.
- The first chirality effect is the helical twist of the  $\mathbf{c}$ -director. For both solvents, i.e. water and formamide, the pitch length is in the order of several micrometers. Remarkably, the two solvents lead to quite different behavior regarding the dynamics of formation of the helical structure. While in samples where the solvent is water the pitch lines take weeks to build up, in mixtures with formamide they form within seconds. The temperature dependence of the pitch is comparable to the thermotropic case. The concentration dependence in contrast is counterintuitive, the helical twist increasing with increasing formamide concentration even though the number density of chiral molecules in the mixtures decreases. A possible explanation for this unexpected behavior is that the rigidity of the solvent layers is reduced by increasing the solvent concentration which in turn facilitates the chirality-induced distortion of the director field.
- The second chirality effect which was observed and investigated is the polar electro-optical switching between two surface-stabilized states. The polar nature of the observed effect indicates that the lyotropic SmC\* analog phase possesses a spontaneous electrical polarization similar to its thermotropic analog. Due to the high conductivity of the solvent it was not possible to measure this polarization directly. Nonetheless, the spontaneous electrical polarization  $P_s$  was estimated by field-dependent measurements of the optical response time to be in the order of  $0.1 \text{ nC cm}^{-2}$ .
- Based on the results obtained in this thesis, a first model of the lyotropic analog of the SmC\* phase was developed. The model suggests that the correlation of the director tilt as well as its helical precession takes place via a strong, three-dimensional hydrogen bond network formed by the solvent molecules. When the solvent concentration is increased, the solvent layers become thicker

and their rigidity is reduced. After reaching a critical distance, the tilt correlation between adjacent bilayers gets lost. This then causes the appearance of the lamellar  $L_\alpha$  phase in which there is no macroscopic tilt correlation.

- In addition to the stated aims of this thesis, the phase diagram of the selected surfactant mixed with *N*-methylformamide as solvent was investigated to show that no lyotropic SmC\* analog phase occurs with a solvent that does not form a three-dimensional hydrogen bond network. However, two other interesting phases appear by the addition of this solvent. The first phase is a rare example of a re-entrant cholesteric phase and the second is a solvent-induced twist grain boundary phase, the first observation of this phase in a lyotropic liquid crystal.

In conclusion, this work shows that a lamellar, tilted, fluid phase exists in lyotropic liquid crystals and that it exhibits characteristic chirality effects, namely helicity and spontaneous electrical polarization, known from the thermotropic ferroelectric SmC\* phase. These results contribute significantly to a better understanding of lyotropic liquid crystals and bridge a substantial gap between the two fields of liquid crystal research. In accordance with the established nomenclature of lyotropic and thermotropic liquid crystals, the novel phase is suggested to be denoted as the lamellar  $L_{\alpha'}^*$  phase, where the index  $\alpha'$  denotes a tilted fluid phase and the superscript \* indicates that molecules are chiral.

## Appendix

### A. Calculation of Electron Density Maps

In Sect. 5.2.1 the structural properties of the two columnar phases Col<sub>1</sub> and Col<sub>2</sub> formed by mixtures of C5O and water or formamide are discussed. In this appendix details on the indexation of their X-ray diffraction patterns as well as on the calculation of the electron density map of the Col<sub>1</sub> phase are given.

In Tables A.1 and A.2 the X-ray diffraction data of the Col<sub>1</sub> phase at 70 °C and the Col<sub>2</sub> phase at 60 °C measured in a C5O sample with 5.5 wt% of water are shown. To every observed periodicity distance  $d_{\text{obs}}$ , the Miller indices ( $hk$ ) were assigned as listed in Tables A.1 and A.2. Both mesophases belong to the plane group  $p2$ . The lattice parameters of the high temperature Col<sub>1</sub> phase and the low temperature Col<sub>2</sub> phase were calculated to be  $a = 9.99$  nm,  $b = 7.75$  nm,  $\gamma = 119.0^\circ$  and  $a = 12.78$  nm,  $b = 12.78$  nm,  $\gamma = 142.4^\circ$ , respectively. To verify these results, the hypothetical periodicity distances  $d_{\text{calc}}$  were calculated using the determined Miller indices and lattice parameters (cf. Eq. 4.13). In case of the Col<sub>1</sub> phase (cf. Table A.1) the values of  $d_{\text{obs}}$  and  $d_{\text{calc}}$  are in agreement. For the Col<sub>2</sub> phase (cf. Table A.2) the deviations of the measured and calculated values are slightly higher than for the Col<sub>1</sub> phase, which can be explained by the declining alignment in the Col<sub>2</sub> phase (cf. Fig. 5.18b). Furthermore, the multiplicity corrected intensities  $I(hk)$  of every diffraction peak are listed. The phase angles  $\phi(hk)$  of the structure factor are only stated for the diffraction peaks, which were used for the calculation of the electron density map.

The electron density map of the Col<sub>1</sub> phase (cf. Fig. 5.18c) was calculated from the data given in Table A.1. For this the equation

$$\rho(x, y) = \frac{1}{V} \sum_{hk} F(hk) \exp[-2\pi i(hx + ky)] \quad (\text{A.1})$$

**Table A.1** X-ray diffraction data of the Col<sub>1</sub> phase of a C5O sample with 5.5 wt% of water at 70 °C

(hk)	d <sub>obs.</sub> (nm)	d <sub>calc.</sub> (nm)	I (hk)	ϕ (hk)
(01)	7.35	7.36	0.1072	0
(1 $\bar{1}$ )	4.37	4.37	0.2914	π/4
(10)	4.37	4.38	0.4246	0
(20)	3.69	3.68	0.0364	–
(1 $\bar{2}$ )	3.36	3.34	0.0311	–
(11)	3.36	3.35	0.0296	–
(2 $\bar{1}$ )	2.30	2.29	0.0723	–
(2 $\bar{2}$ )	2.22	2.19	0.0025	–
(20)	2.19	2.19	0.0049	–

**Table A.2** X-ray diffraction data of the Col<sub>2</sub> phase of a C5O sample with 5.5 wt% of water at 60 °C

(hk)	d <sub>obs.</sub> (nm)	d <sub>calc.</sub> (nm)	I (hk)	ϕ (hk)
(01)	12.07	12.42	0.0502	–
(02)	6.07	6.21	0.0096	–
(1 $\bar{1}$ )	4.12	4.19	0.3002	–
(10)	3.90	3.89	0.4152	–
(1 $\bar{2}$ )	3.90	4.05	0.0775	–
(1 $\bar{3}$ )	3.44	3.59	0.0373	–
(12)	2.90	2.85	0.0089	–
(2 $\bar{2}$ )	2.05	2.10	0.0556	–
(2 $\bar{1}$ )	2.05	2.04	0.0139	–
(2 $\bar{3}$ )	2.03	2.09	0.0099	–
(20)	1.96	1.95	0.0217	–

was used, which connects the electron density  $\rho(x, y)$  to the scattering amplitude  $F(hk)$  by Fourier transform [1]. The complex scattering amplitude  $F(hk)$  can be split up into its modulus  $|F(hk)|$  and a term including its phase angle  $\phi(hk)$  according to

$$F(hk) = |F(hk)| \exp[i\phi(hk)]. \quad (\text{A.2})$$

The modulus  $|F(hk)|$  of the scattering amplitude is related to the intensity  $I(hk)$  of the diffraction peaks via

$$|F(hk)| \propto \sqrt{I(hk)}. \quad (\text{A.3})$$

The electron density can thus be written as

$$\rho(x, y) \propto \sum_{hk} \sqrt{I(hk)} \exp[-2\pi i(hx + ky) + i\phi(hk)] \quad (\text{A.4})$$

or as

$$\rho(x, y) \propto \sum_{hk} \sqrt{I(hk)} (\cos[-2\pi(hx + ky) + \phi(hk)] + i \sin[-2\pi(hx + ky) + \phi(hk)]) \quad (\text{A.5})$$

if including Euler's formula. As in the plane group  $p2$  for every reflection  $(hk)$  a symmetry equivalent reflection  $(\bar{h}\bar{k})$  exists, the term containing the central symmetric sine function is canceled out. Hence, Eq. A.5 is reduced to

$$\rho(x, y) \propto \sum_{hk} \sqrt{I(hk)} \cos[-2\pi(hx + ky) + \phi(hk)] \quad (\text{A.6})$$

for the given plane group.

Equation A.6 makes it possible to calculate the electron density of the probed sample if the phase angle  $\phi(hk)$  of the scattering amplitude is known. However, no experimental method exists which enables the determination of this value. For non-centrosymmetric plane groups  $\phi(hk)$  may take every value between 0 and  $2\pi$ . Hence, the number of possible electron density maps is infinite. To enable the calculation of electron density maps in a finite time, the value of  $\phi(hk)$  was varied in steps of  $\pi/4$ . This results in reasonable approximations of the electron density. To decide which of the electron density maps obtained is the one best reflecting the reality, the maps are compared by means of physical and chemical plausibility. A possible way of doing this is by comparing the volume fractions of the different parts of the molecules with the histogram of the calculated electron density maps. In reasonable electron density maps these volume fractions should match with well separated regions of high and low electron density.

Practical calculations of the electron density maps were performed with the program *MATLAB R2013a* by *The MathWorks* (USA). For this a program code was written which is listed below. Comments in the code are marked with the symbol '%'.

**MATLAB** code for the calculation of electron density maps (plane group  $p2$ ):

```

a = 999;
% value of the lattice parameter a
breal = 775;
% value of the lattice parameter b
gamma = 2.0773;
% value of the lattice parameter gamma
b = round(breal*cos(gamma-1.570976));
% value of the lattice parameter after projection on the x-axis

s = 2;
% step size

n = 1:(4*a/s)*(4*b/s);
% row vector of calculation points

M = (-2*a:s:2*a-1);
ex = repmat(M,4*b/s,1);
% array for calculation of data points with respect to the direction of b

num = [1:s:4*b];
ta = 1/tan(gamma);
tnum = (num*ta).';
tex = repmat(tnum,1,4*a/s);
X = ex+tex;
% array for calculation of data points with respect to the x-axis, includes
projection of b on the x-axis

O = (-2*b:s:2*b-1);
Or = repmat(O,4*a/s,1);
Y = Or. ';
% array for calculation of data points with respect to the direction of a
and the y-axis

I1 = 0.1072;
I2 = 0.2914;
I3 = 0.4246;
% relative scattering intensities of the three strongest diffraction peaks

for u1=[0 1 2 3 4 5 6 7];
% permutation of the phase of the structure factor in steps of Pi/4
for u2=[0 1 2 3 4 5 6 7];
% permutation of the phase of the structure factor in steps of Pi/4
for u3=[0];
% the phase of one of the diffraction peaks can be set to a constant value
as it only leads to a shift of the electron density relative to the lattice

h1 = 1;
k1 = -1;
h2 = 1;
k2 = 1;
h3 = 2;
k3 = 0;
% Miller indices of the diffraction peaks

h1a = -h1;
k1a = -k1;
h2a = -h2;
k2a = -k2;

```

```

h3a = -h3;
k3a = -k3;
% symmetry-equivalent reflections in the plane group p2

r(n) = I1^0.5*(cos(-2*pi*(h1*ex(n)/a +k1*Y(n)/b) +u1*pi/4))
      + I2^0.5*(cos(-2*pi*(h2*ex(n)/a +k2*Y(n)/b) +u2*pi/4))
      + I3^0.5*(cos(-2*pi*(h3*ex(n)/a +k3*Y(n)/b) +u3*pi/4))
      + I1^0.5*(cos(-2*pi*(h1a*ex(n)/a +k1a*Y(n)/b) +u1*pi/4))
      + I2^0.5*(cos(-2*pi*(h2a*ex(n)/a +k2a*Y(n)/b) +u2*pi/4 ))
      + I3^0.5*(cos(-2*pi*(h3a*ex(n)/a +k3a*Y(n)/b) +u3*pi/4));
% Fourier transform gives electron density as row vector

roh =reshape(r(n),4*b/s,4*a/s);
% electron density as array

figure(1)
mesh(X,Y,roh)
% plots the electron density

d = (-3:0.05:3);
figure(2)
hist(r(n),d);
% plots the histogram of the electron density

ne = histc(r(n),d);
ce = cumsum(ne);
% sums up the histogram
figure(3)
bar(d,ce)

ind1 = find(ce>(0.344*ce(121)));
% finds the value in the histogram which corresponds to the volume fraction
of the alkyl chains
ind2 = find(ce>(0.682*ce(121)));
% finds the value in the histogram which corresponds to the volume fraction
of the alkyl chains and the aromatic core

l = zeros(1,121);
l(ind1(1)) = 90000;
l(ind2(1)) = 90000;
l(2,:) = hist(r(n),d);
figure(4)
plot(d,l)
% plots the histogram of the electron density with indication of the volume
fractions

saveas(figure(1),['map' num2str(u1) num2str(u2) num2str(u3) '.jpg'])
saveas(figure(4),['hist' num2str(u1) num2str(u2) num2str(u3) '.jpg'])
% saves the figures

end
end
end

```

Application of the code results in 64 possible electron density maps. Further diffraction peaks, however, can be included into the calculation leading to further, more refined electron density maps. To decide which of the 64 maps obtained is the



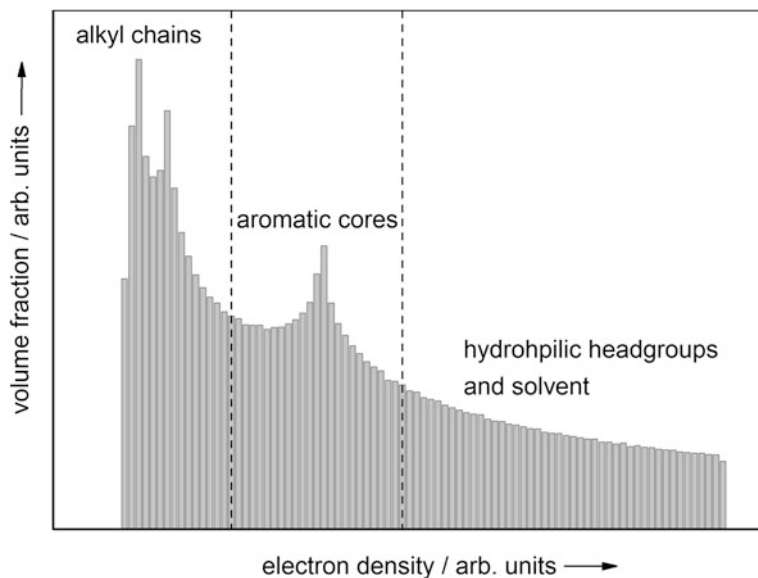


**Fig. A.1** Histogram of the most likely electron density map (cf. Fig. 5.18c). The summed-up volume fractions corresponding to the alkyl chains, the aromatic cores and the hydrophilic parts of the surfactant as well as the solvent are separated from each other with *dashed lines*

most realistic, the histograms of the electron density were calculated. The histogram of the chosen electron density map (cf. Fig. 5.18c) is shown in Fig. A.1. The volume fractions of the alkyl chains, the aromatic cores and the hydrophilic headgroup of the surfactant as well as the volume fraction of the solvent in the mixture were estimated by modeling the *Connolly solvent excluded volume* of the energy minimized molecules with the program *Chem3D Pro 13.0*. Areas corresponding to these volume fractions are separated with dashed lines in Fig. A.1. They exhibit a good correlation with the histogram. In the region of lowest electron density which corresponds to the alkyl chains two maxima can be found. These two maxima can be explained by different degrees of interdigitation of the alkyl chains. At intermediate electron densities only one maximum is present which arises from the aromatic cores. At high electron densities, which can be attributed to the oxygen-containing hydrophilic headgroups and solvent molecules, a rather broad distribution is found, which reflects the smooth transition between the solvent layers and the hydrophilic headgroups.

## ***B. Conference Contributions Originating from this Work***

J.R. Bruckner, D. Krueerke, F. Giesselmann, *New 2D-correlated structure of a lyotropic liquid crystalline diol*, 39th German Conference on Liquid Crystals (O12), Hamburg, Germany, (2011)

J.R. Bruckner, J.H. Porada, D. Krueerke, S. Jagiella, D. Blunk, F. Giesselmann, *In search of the lyotropic liquid crystalline smectic C phase*, 24th International Liquid Crystal Conference, Mainz, Germany, (2012)

J.R. Bruckner, J.H. Porada, M. Harjung, C.F. Dietrich, I. Dierking, F. Giesselmann, *Chirality effects in a first example of a lyotropic smectic C\* phase*, 40th German Conference on Liquid Crystals (O24), Paderborn, Germany, (2013)

J.R. Bruckner, J.H. Porada, M. Harjung, C.F. Dietrich, I. Dierking, F. Giesselmann, *Chirality effects in a first example of a lyotropic smectic C\* phase*, 31st International Conference on Ferroelectric Liquid Crystals (36 O), Magdeburg, Germany, (2013)

J.R. Bruckner, J.H. Porada, F. Giesselmann, *Solvent induced twist grain boundary phase in a lyotropic liquid crystal*, 41st German Conference on Liquid Crystals (O10), Magdeburg, Germany, (2014)

J.R. Bruckner, J.H. Porada, F. Knecht, C.F. Dietrich, M. Harjung, F. Giesselmann, *Lyotropic chiral smectic C liquid crystal with polar electro-optic switching*, 25th International Liquid Crystal Conference (CL-O2.001), Dublin, Ireland, (2014)

F. Knecht, J.R. Bruckner, F. Giesselmann, *New insights into the lyotropic analog of the chiral smectic C\* phase*, 42nd German Conference on Liquid Crystals (O9), Stuttgart, Germany, (2015)

J.R. Bruckner, F. Knecht, M. Harjung, I. Dierking, J.H. Porada, F. Giesselmann, *The lyotropic analogue of the chiral smectic C\* phase*, 15th International Conference on Ferroelectric Liquid Crystals (Keynote Lecture), Prague, Czech Republic, (2015)

## **Reference**

1. C. Giacovazzo, H.L. Monaco, G. Artioli, D. Viterbo, M. Milanesio, G. Ferraris, G. Gilli, P. Gilli, G. Zanotti, M. Catti, in *Fundamentals of Crystallography*, 3rd ed. by C. Giacovazzo (Oxford University Press, New York, 2011)